

The Effect Of Spin-Orbit Coupling On Electronic Structure And Magnetism In Low Dimensional Compounds

Thesis submitted for the degree of
Doctor of Philosophy (Science)
in
Physics (Theoretical)

by
POONAM KUMARI

Department of Physics
University of Calcutta

2019

Dedicated to

My Parents

Acknowledgement

I wish to express my sincere thanks to my supervisor, Prof. Priya Mahadevan for her supervision and guidance during my Ph.D. I have learnt a lot from her and I am really thankful for her valuable inputs and insights without which this thesis would not have been possible. I also want to thank my thesis committee, Prof. P. K Mukhopadhyay, Prof. Anjan Barman and Prof. K. S. R. Menon (from SINP Kolkata) for their valuable inputs and suggestions during the course of my Ph.D. An honest thanks goes to the computer section here at S. N. Bose.

I would like to take this opportunity to thank all my past and present group members for their help, support and discussions, Hirak da, Saikat da, Ruma di, Shishir da, Basudeb da, Sagar da, Soumya da, Bipul da, Ravikishor da, Deepika di, Joydeep, Sumanti, Debayan, Prasun, Shivam and all the project students who visited our group, Gokul, Aathira, Surender and Komal.

I would also like to remember and thank my college Professors, Prof. R. Nagrajan, Prof. D. Mathur, Prof. S. Krishnagopal and Dr. A. Das for motivating me to take this journey.

A heartfelt thanks goes to Shoumi, Rashi, Pooja, Ninad and Navneeta.

I also want to thank Ashutosh bhैया, Arup da, Ravi, Ransell, Shaili, Dhani, Poulami, Chandrayee, Ankan, Ritam, Monalisa, Shauri, Jayita, Edwin and Rahul for contributing towards making these six years at S. N. Bose memorable.

Finally, I would like to express my love and gratitude to my family. I am grateful to my parents, brother and sister-in-law for their unconditional love, support and respect for my decisions and choices.

Poonam Kumari
Kolkata, India
2019

List Of Publications

1. Structural distortions in monolayers of binary semiconductors.
Poonam Kumari*, Saikat Debnath* and Priya Mahadevan.
Phys. Rev. B. **97**, 041404(R) (2018).
2. Quantum confinement: A route to enhance the Curie temperature of Mn doped GaAs.
Basudeb Mandal*, Hirak Kumar Chandra*, **Poonam Kumari*** and Priya Mahadevan.
Phys. Rev. B **96**, 014430 (2017).
* equal contribution
3. Engineering spin-valley physics in bilayers of MoSe₂.
Poonam Kumari, Joydeep Chatterjee and Priya Mahadevan.
(Under Review)
4. In search of planar bismuthene.
Poonam Kumari and Priya Mahadevan.
(Manuscript under preparation)
5. Role of spin-orbit coupling on magnetism in Sr₂IrO₄.
Poonam Kumari and Priya Mahadevan.
(Manuscript under preparation)

Contents

Table of Contents	x
List of Figures	xvi
List of Tables	xx
1 Introduction	1
1.1 Motivation	1
1.2 Spin-Orbit Coupling	2
1.3 Two dimensional materials	5
1.4 Quantum Spin Hall Effect	15
1.5 Transition Metal Oxides	17
1.6 Overview of the thesis	20
2 Theoretical Concepts	31
2.1 Many body Hamiltonian	31
2.2 Born-Oppenheimer Approximation	32
2.3 Density Functional Theory (DFT)	32
2.3.1 The Hohenberg-Kohn Theorems	34
2.3.2 Kohn-Sham Formulation	35
2.3.3 Approximations For Exchange Correlation Functional	39
2.4 Numerical Approximations for DFT Calculations	41
2.4.1 Plane Wave Basis and Cut-off Energy	41
2.4.2 K -Space Integrations	42
2.4.3 Pseudopotential and Frozen core approximation	42
2.4.4 Projector Augmented-Wave(PAW) Method	44
2.5 Van der Waals Correction: DFT-D2 Method	45

2.6	Tight Binding Method	46
3	Effect Of Spin Orbit Coupling On Electronic Structure Of Transition Metal Dichalcogenides	53
3.1	Introduction	53
3.2	Methodology	54
3.3	Results and discussion	57
3.4	Conclusion	73
4	In Search Of Planar Graphitic Semiconductors	79
4.1	Motivation	79
4.2	Structural Distortions in Monolayers Of Binary Semiconductors	80
4.2.1	Introduction	80
4.2.2	Methodology	81
4.2.3	Results and Discussion	82
4.3	Route to planar Bismuthene	91
4.3.1	Introduction	91
4.3.2	Methodology	93
4.3.3	Results and Discussion	93
4.4	Conclusion	101
5	The Role Of Spin-Orbit Coupling On Magnetism In Sr_2IrO_4	109
5.1	Introduction	109
5.2	Methodology	111
5.3	Result and Discussion	113
5.4	Conclusion	118
	Appendix A	124
A		125
A.1	Monte Carlo Simulation For Heisenberg Model	125
A.2	Heisenberg Model	125
A.3	Metropolis Hastings Algorithm	126
A.4	Results	127

List of Figures

1.1	Family of two dimensional materials. Reproduced from [52]	7
1.2	Two dimensional materials covering different range of electromagnetic spectra. Reproduced from [53]	8
1.3	Different polymorphs of TMDs. Reproduced from [62].	9
1.4	Hexagonal Brillouin zone of TMDs with high symmetry points indicated. Reproduced from [63]	10
1.5	Opposite splitting of K and -K valley in monolayer of TMDs. Reproduced from [64]	11
1.6	Angle Resolved Photo Emission Spectroscopy (ARPES) band dispersion of monolayer of MoS ₂ in the Γ to K direction reproduced from [70] as well as bandstructure calculated from Density Functional Theory (DFT) along Γ to K direction superimposed on it reproduced from [66]	12
1.7	Selective valley polarization in monolayer of WSe ₂ . Reproduced from [64]	13
1.8	High symmetry stackings possible in bilayer TMDs. Reproduced from [75]	13
1.9	Circular luminescence for monolayer (blue) and bilayer (green) of MoS ₂ . Left panel of the inset shows 2H stacking of bilayer MoS ₂ . Right panel of the inset shows Photoluminescence spectra for monolayer (blue) and bilayer (green) MoS ₂ . Reproduced from [76]	14
1.10	Spin polarized channels in QSH insulators. Reproduced from [78]	15
1.11	Normal insulators, quantum hall insulators and quantum spin hall insulators. Reproduced from [79].	16
1.12	conducting edge states in graphitic monolayer of bismuth. Reproduced from [67]	17
1.13	Octrahedral environment. Reproduced from [95]	19
1.14	Octrahedral splitting of d-orbitals. Reproduced from [95]	19
2.1	Flowchart of DFT	39
2.2	Core electrons in pseudo potential approach. Reproduced from [27]	43

3.1	a) Ab-initio bandstructure along the Γ to X direction for GaAs conventional cell. b) The supercell bandstructure along Γ to X direction c) The unfolded bandstructure of the 2x1x1 supercell of GaAs along Γ to X direction with the spectral weights proportional to band thickness	56
3.2	Ab-initio bandstructure of monolayer MoSe ₂ calculated along various symmetry directions with (dashed red line) and without (solid black line) spin-orbit interactions. The inset shows an expanded view with the magnitude of the spin splitting indicated.	58
3.3	Comparison of ab-initio band dispersions (solid black line) for monolayer MoS ₂ and the fitted tight binding bands (red dashed line), using a basis consisting of Mo <i>s</i> , <i>p</i> , <i>d</i> and S <i>s</i> , <i>p</i> , <i>d</i> states, calculated along various symmetry directions.	59
3.4	Comparison of ab-initio band dispersions (solid black line) for monolayer MoSe ₂ and the fitted tight binding bands (red dashed line), using a basis consisting of Mo <i>s</i> , <i>p</i> , <i>d</i> and Se <i>s</i> , <i>p</i> , <i>d</i> states, calculated along various symmetry directions.	59
3.5	Comparison of ab-initio band dispersions (solid black line) for monolayer MoTe ₂ and the fitted tight binding bands (red dashed line), using a basis consisting of Mo <i>s</i> , <i>p</i> , <i>d</i> and Te <i>s</i> , <i>p</i> , <i>d</i> states, calculated along various symmetry directions.	60
3.6	The bandstructure of MoS ₂ monolayer using tight-binding model with spin-orbit coupling included, calculated along various symmetry directions. . . .	61
3.7	The bandstructure of MoSe ₂ monolayer using tight-binding model with spin-orbit coupling included, calculated along various symmetry directions. . . .	62
3.8	The bandstructure of MoTe ₂ monolayer using tight-binding model with spin-orbit coupling included, calculated along various symmetry directions. . . .	63
3.9	The ab-initio bandstructure with (dashed red line) and without (solid black line) spin-orbit interactions along Γ to K direction for 2H stacking MoSe ₂ (structure shown schematically). The contributions from Mo atoms of each layer for the two highest occupied bands at K point after inclusion of spin-orbit interactions is also given.	65
3.10	Structure of one of the twisted bilayers with angle of rotation 38.2°. Mo1 is the from the bottom layer whereas Mo2 represents Mo from the top layer. . . .	66
3.11	Ab-initio bandstructure with spin-orbit interactions included for MoSe ₂ bilayer at a twist angle of 38.2° along the Γ to \bar{K} direction.	67
3.12	The supercell bandstructure without spin-orbit coupling included along Γ to K direction of the primitive cell.	67
3.13	The unfolded bandstructure without spin-orbit coupling included along Γ to K direction of the primitive cell with spectral weights proportional to band thickness.	68

3.14	The ab-initio bandstructure with (dashed line) and without (solid line) spin-orbit interactions along Γ to K direction for MoSe ₂ bilayer with 2H stacking at the interlayer separation equal to that of the twisted bilayers.	69
3.15	The unfolded bandstructure without spin-orbit coupling included along Γ to K direction of the primitive cell for MoSe ₂ bilayer at a twist angle of 15.8° with spectral weights proportional to band thickness.	69
3.16	Schematic showing the contributions to \bar{K} from the Brillouin zone of the rotated and unrotated primitive cells	72
4.1	a) Bulk Wurtzite structure of CdS b) Planar graphitic structure at the bulk lattice constant.	82
4.2	The phonon dispersion of graphitic phase of a monolayer of CdS along different symmetry directions using optimized in-plane lattice constants. The displacement of the atoms corresponding to the eigenfunction for the unstable phonon mode in one unit cell are shown in the inset. Reproduced from [35]	83
4.3	Top view of relaxed buckled non-polar structure for CdS where Up(Dn) denotes the anions that have moved in positive(negative) z-direction.	84
4.4	Phonon dispersion of monolayer of planar CdS under 2% biaxial tensile strain. This Figure has been taken from Ref([35])	87
4.5	Shift in Energy (in eV) of the highest occupied bands at Γ and K on application of strain in planar CdS.	89
4.6	Charge density of the highest occupied band at Γ and the charge density of the highest occupied band at K-point in planar CdS.	90
4.7	Structure of bulk Bismuth	94
4.8	Variation of Energy with lattice constant for freestanding planar and buckled Bismuthene	95
4.9	Bandstructure of planar freestanding bismuthene calculated along various symmetry directions	95
4.10	Layer of bismuth atoms on Ag(111) slab	96
4.11	Bandstructure of bismuthene on Ag(111) substrate calculated along various symmetry directions	97
4.12	Hydrogenated SiC and its bandstructure calculated along various symmetry directions.	98
4.13	Formation energies involved in obtaining Bismuthene	99
4.14	Hydrogenated SiC with a layer of Bi on top of H and its bandstructure calculated along various symmetry directions.	100
4.15	Quasi freestanding bismuthene its bandstructure calculated along various symmetry directions.	100

4.16	Electrostatic potential of the substrate and the quasi freestanding bismuthene	101
5.1	Structure of $\text{Sr}_{n+1}\text{Ir}_n\text{O}_{3n+1}$ for $n = 1$, $n = 2$ and $n = \infty$. Reproduced from [3]	110
5.2	Schematic of the electronic structure of $\text{Sr}_{n+1}\text{Ir}_n\text{O}_{3n+1}$ for $n = 1$, $n = 2$ and $n = \infty$. Reproduced from [12]	110
5.3	Non-magnetic bandstructure of Sr_2IrO_4 using ab-initio (solid black line) method and tight binding (dashed red line) along various symmetry directions. Γ , M and X are taken to be (0.0, 0.0, 0.0), (0.5, 0.5, 0.0) and (0.5, 0.0, 0.0) respectively.	113
5.4	Orbital projected density of states for Ir atom	115
5.5	Schematic of the electronic structure of Sr_2IrO_4	115
5.6	Various magnetic configurations considered for Sr_2IrO_4	116
5.7	Bandstructure of Sr_2IrO_4 using multiband hubbard hamiltonian with spin orbit coupling included for $U=1.0$ eV, $SO=0.4$ eV along various symmetry directions.	117
5.8	Bandstructure of Sr_2IrO_4 using multiband hubbard hamiltonian with spin orbit coupling included for $U=1.5$ eV, $SO=0.4$ eV along various symmetry directions.	117
5.9	Schematic explaining magnetic stability for $U=1.0$ eV compared to $U=2.0$ eV	118

List of Tables

3.1	The magnitude of the spin-splitting of VBM at K for MoS ₂ , MoSe ₂ and MoTe ₂ monolayer.	57
3.2	Parameters obtained from least-squared-error minimization fitting of the ab-initio band structure onto a tight binding model using <i>s</i> , <i>p</i> , <i>d</i> orbitals of Mo and S for monolayer MoS ₂	60
3.3	Parameters obtained from least-squared-error minimization fitting of the ab-initio band structure onto a tight binding model using <i>s</i> , <i>p</i> , <i>d</i> orbitals of Mo and Se for monolayer MoSe ₂	61
3.4	Parameters obtained from least-squared-error minimization fitting of the ab-initio band structure onto a tight binding model using <i>s</i> , <i>p</i> , <i>d</i> orbitals of Mo and Te for monolayer MoTe ₂	62
3.5	Comparison of the spin-splitting of VBM for MoS ₂ , MoSe ₂ and MoTe ₂ using ab-initio and tight-binding model.	63
3.6	The angle of rotation and the corresponding number of atoms in the supercell for different twisted MoSe ₂ bilayers.	65
3.7	The angle of rotation and the corresponding spin-splitting of the VBM. The labels for specific choice of angles has also been given.	70
3.8	A table showing the angles made by primitive cell unrotated lattice vectors and primitive cell rotated lattice vectors to the supercell lattice vectors. . .	71
4.1	Table comparing the energies of the Planar(P), Buckled Polar (BP) and Buckled Non-Polar(BNP) structures for a monolayer of the listed semiconductor.	85
4.2	Table showing the net dipole moment and the energy due to the dipole (E(dp)) for the buckled polar structure.	86
4.3	Table showing the cation-anion and anion-anion bondlengths (in Å) for both polar buckled and non-polar buckled structures	86

- 4.4 Table showing the breakup of the total energies in the ab-initio calculations performed using VASP are given. The energy associated with the sum of the occupied eigenvalues is called Eband. It also includes the Hartree energy (electron-ion interaction). This is the reason why 1/2 of the Hartree energy must be subtracted out while evaluating the total energy. Ewald energy is the ion-ion interaction term. $E(xc)$ and $V(xc)$ are energies associated with the exchange and correlation functional. The PAW double counting accounts for the double counting in the Hartree energy. All components in the above Table must be added except the Hartree energy. 1/2 times the Hartree energy must be subtracted out in order to get the total energy. . . . 88
- 5.1 Parameters obtained from least-squared-error fitting of the ab-initio band structure onto a tight binding model for Sr_2IrO_4 114

Chapter 1

Introduction

1.1 Motivation

The electronic industry has seen rapid miniaturization since 70's following Moore's law, proposed in 1965 by Gordon Moore [1]. It is an empirical law which predicted that in a dense integrated circuit, the number of transistors doubles every two years. For several decades, semiconductor industry has been guided by this law. Modern day integrated circuits now contain millions of transistors with their sizes smaller than 100 nm. More and more materials with desirable properties to be used in these devices are being studied. The field of spintronics has emerged rapidly in this regard. Spintronics, as the name suggests, utilizes the spin of an electron and its interactions which lead to various interesting and exotic phenomena like spin-valley physics, quantum spin hall effect etc and the aim is that they will provide an alternate technology as well as a route to a new generation of more efficient devices. As a result, there is an upsurge in understanding these spin induced phenomena in materials.

Spin is a quantum mechanical property of an elementary particle, which has a quantized value and can be measured. As described by Landau and Lifshitz [2], the spin of an electron is stated to be *“This property of elementary particles is peculiar to quantum theory and therefore has in principle no classical interpretation. In particular, it would be wholly meaningless to imagine the ‘intrinsic’ angular momentum of an elementary particle as being the result of its rotation about its own axis.”* In 1925 Ralph de Laer Kronig, after the discovery of anomalous Zeeman effect, in order to explain it for the first time, proposed that electrons poses another kind of momentum apart from the angular momentum which comes because of its rotation about its own axis [3]. He however never published this idea. A few months later George Uhlenbeck and Samuel Goudsmit

published similar idea about electrons spinning around its own axis giving rise to an angular momentum [4]. However it was Wolfgang Pauli in 1927 [5], who worked out the mathematical theory of spin and it was established that it is a quantum mechanical entity and has no classical analogue. Ever since its discovery, it has been widely studied and its existence can be experimentally inferred by experiments like the Stern-Gerlach experiment [6–8]. Because of the relativistic nature of an electron, when it moves in an electric field of the nucleus of an atom, it experiences a magnetic field in its rest frame through Lorentz transformation of the electric field. The spin of the electron interacts with this magnetic field and gives rise to what is called the spin-orbit effect. In solids, this effect give rise to many interesting and exotic phenomena like spin-splitting of bands in systems which lack inversion symmetry [9–12], quantum spin hall effect [13–16] etc. Two dimensional materials provide a very rich playground to investigate these effects. The main aim of this thesis is to understand and investigate some of these exciting phenomena due to spin-orbit coupling in low dimensional compounds. We first present a discussion of the form of the spin-orbit coupling term in the next section.

1.2 Spin-Orbit Coupling

In this section we discuss a semi classical approach to deriving the form of the spin-orbit coupling term in an atom. In order to do that, let us consider a hydrogen like system where an electron is orbiting around a positively charged nucleus with a velocity v_{orbit} in an orbit with a radius \vec{r} . Let the charge on the nucleus be Ze , where, Z is the atomic number of the atom and e is the charge of an electron. Let us further assume that the magnetic moment of the electron is $\vec{\mu}_e$. While the electron is orbiting around the nucleus, it feels the electric field due to the presence of the positively charged nucleus of the atom. Now, since we know that electron is a relativistic particle, it experiences a magnetic field \vec{B} in its own rest frame, due to Lorentz transformation of the electric field. The interaction energy (H_{SO}) of the electron due to the appearance of this magnetic field is given as

$$H_{SO} = -\vec{\mu}_e \cdot \vec{B} \quad (1.1)$$

We know that magnetic moment of an electron can be written in units of Bohr magneton (μ_B), its spin and the gyromagnetic ratio as

$$\mu_e = -g_0\mu_B\vec{s} \quad (1.2)$$

Using this definition in Equation 1.1, we get

$$H_{SO} = g_0\mu_B\vec{B} \cdot \vec{s} \quad (1.3)$$

Now if we look at this from the frame of the electron, we have electron at rest and the nucleus moving around in an orbit whose radius is now given as \vec{r} and the velocity with which the nucleus is revolving around the electron is v_{orbit} . Now we apply Biot Savart law and calculate the magnetic flux density \vec{B}_0 at the point where the electron is. This can be written as follows

$$\vec{B}_0 = Ze\frac{\vec{r} \times v_{orbit}}{4\pi\epsilon_0c^2r^3} \quad (1.4)$$

here ϵ_0 is the permittivity of free space and c is the speed of light. Since we know that momentum can be written as $\vec{K} = m\vec{r} \times v_{orbital}$ and \vec{K} can be quantized in units of \hbar as $\vec{K} = \hbar\vec{L}$ the magnetic field expressed in Equation 1.4 can therefore be written as

$$\vec{B}_0 = \frac{Ze\hbar\vec{L}}{4\pi\epsilon_0mc^2r^3} \quad (1.5)$$

Now putting this value of B_0 from Equation 1.5 back in Equation 1.3, we get the following

$$H_{SO} = g_0\mu_B\hbar\frac{Ze}{4\pi\epsilon_0mc^2r^3}\vec{L} \cdot \vec{s} \quad (1.6)$$

After Thomas correction of the factor of 1/2 which arises due to the relativistic nature of electron [17] and needs to be put in externally here.

$$H_{SO} = g_0\mu_B\hbar\frac{Ze}{8\pi\epsilon_0mc^2r^3}\vec{L} \cdot \vec{s} \quad (1.7)$$

We also know that for a $|n, l\rangle$ electronic state, $\langle r^{-3} \rangle$ can be written as

$$\langle r^{-3} \rangle_{n,l} = \frac{2Z^3}{a_0^3n^3l(l+1)(2l+1)} \quad (1.8)$$

where a_0 is the Bohr's radius, n is the principle quantum number and l is the angular quantum number. Putting Equation 1.8 in Equation 1.7 we get

$$H_{SO} = \frac{g_0\mu_B\hbar Z^4e}{4\pi\epsilon_0mc^2a_0^3n^3l(l+1)(2l+1)}\vec{L} \cdot \vec{s} = \lambda\vec{L} \cdot \vec{s} \quad (1.9)$$

where

$$\lambda = \frac{g_0 \mu_B \hbar Z^4 e}{4\pi \epsilon_0 m c^2 a_0^3 n^3 l(l+1)(2l+1)} \quad (1.10)$$

and it is called the spin-orbit coupling constant. Looking at the Equation 1.10 carefully, we see that, the spin-orbit constant λ varies with the atomic number as Z^4 . As a result, the value of this constant increases as we go to heavier elements and the effects of spin-orbit coupling becomes more and more prominent in materials containing heavy elements. λ also has a dependence on the principle quantum number n as n^{-3} . It is therefore the ratio of $\frac{Z^4}{n^3}$ which dictates the value of λ in an isolated atom where hydrogenic picture holds. Moving away from the hydrogenic picture, however, this dependence gets weaker. It varies from 20-40 meV in $3d$ ions [18] to 200-500 meV in $5d$ ions [19].

In a solid if we look at the spin-orbit interaction, we find that the electric field which gives rise to this effect has several different origins. The electrons in the conduction band in a solid are free to move within the solid and can be seen as quasi free particles. These quasi free electrons do not experience a very strong electric field by the nucleus of the atoms. They can however experience electric field whose origin can be different.

In two dimensional materials with surfaces or interfaces such as in heterostructures, the electric field generated due to an internal potential gradient can lead to Rashba spin-orbit effects, which was named after E. I. Rashba [20]. An external electric field enhances this interaction [21–24]. Sometimes in an asymmetric crystal, like GaAs, the electrons moving in the crystal's asymmetric potential experience an electric field which results in an intrinsic spin-orbit interaction. This was first studied by Dresselhaus for zinc-blende structures [25]. It is called Dresselhaus interaction. This effect [26–29] in systems with no inversion symmetry leads to phenomena like splitting of the bands into spin up and spin down bands, which can provide separate spin channels for transport in these materials and can be of use in spintronic devices. In systems where inversion symmetry is preserved, i.e if $\vec{r} \rightarrow -\vec{r}$, the crystal lattice remains the same upon this operation. Hence we have

$$E(k, \uparrow) = E(-k, \uparrow) \quad (1.11)$$

and

$$E(k, \downarrow) = E(-k, \downarrow) \quad (1.12)$$

Also, we know that according to Kramer's degeneracy theorem, which says that in a system where time reversal symmetry is preserved, states which have opposite momenta

and spin must have the same energy. We therefore have

$$E(k, \uparrow) = E(-k, \downarrow) \quad (1.13)$$

Taking into account all three equations we get

$$E(k, \uparrow) = E(k, \downarrow) \quad \text{and} \quad E(-k, \uparrow) = E(-k, \downarrow) \quad (1.14)$$

This means that since spin-orbit coupling cannot induce magnetism and break time reversal symmetry, it can not result in a net spin splitting in a system which has inversion symmetry in absence of an external magnetic field. In this thesis we have focused mainly on the electronic structure of two dimensional materials where inversion symmetry is broken and the effect of spin-orbit interactions on the electronic structure of these materials is investigated. To examine this effect it is important to understand some properties of two dimensional materials.

1.3 Two dimensional materials

The past few decades have seen an upsurge in the research of nanoscience and nano materials. These are materials whose sizes ranges from one to ten nanometers in atleast one direction. If the size of the materials are restricted only in one direction, then one gets two dimensional(2D) materials with bulk like periodicity in two directions but confinement in one. If the size of the materials are restricted in two directions, then we get one dimensional(1D) materials. The interest in going from bulk to 2D and 1D materials lies in the unusual change in properties shown by these low dimensional materials. CdS nanocrystals for example, show a bandgap change from 4.5 eV to 2.5 eV as their diameter changes from 13 Å to 39 Å [30]. This tunability of bandgap with size make them suitable candidates to be used in various opto electronic devices [31, 32]. In other instances, magnetism can be induced with the change in dimensionality. For instance thiol-capped gold nanoparticles at 1.4 nm size [33] become magnetic. Other properties like ionization potential, melting point etc. have also been reported to vary with size, as can be seen in case of platinum, where its ionization potential varies from 9.0 eV for a single atom to the work function of its bulk form which is 5.3 eV [34]. Also in case of gold, it has been reported that its melting point in the bulk form is 1336 K but for 2.5 nm, it is reported to be 930 K [35].

As we go from bulk to 2D materials, these change in properties can be attributed to mainly two effects, surface effects and quantum confinement effects.

In the nano regime, materials have large surface to volume ratio. The atoms on the surface have less number of neighbors than the ones present in the bulk. As a result, the atoms on the surface has high affinity to form bonds compared to their bulk counterpart. This makes the surface atoms very suitable to be used as catalysts. For example, gold nanoparticles have been used as catalysts in many organic reactions [36]. Iron nanoparticles have been used as a catalysts for production of lower olefins, which are key ingredients of drugs, cosmetics and plastics [37].

In a semiconductor, upon excitation, an exciton is formed, which is a pair of electron and a hole bound together by Coulomb interaction between them. This exciton has a radius called Bohr exciton radius, which is the separation between the electron and the hole upto which they form a bound state. In a bulk semiconductor, this exciton moves freely in the material [38]. This is however not the case as we go to lower dimension where the size of the material becomes comparable to the Bohr exciton radius. Also, in this limit the wavefunction of the electron and the hole start getting effected due to the confinement effect. This modifies the electronic structure of the material. This effect is called quantum confinement effect. It has been studied extensively in silicon and germanium quantum dots [39], quantum wells [40], nanowires [41] and other nanomaterials [42]

Much before stable two dimensional materials were discovered, people have been studying these two dimensional systems. For example high temperature superconductivity in cuprate [43], where CuO_2 plane has confinement of superconductivity and some of the examples mentioned earlier. But it was after the successful exfoliation of graphene in 2004 by Novoselov and Geim by Scotch tape method [1,2], the research in the field of layered two dimensional material saw an upsurge. Layered materials are one where atoms are arranged in layers, with the inplane bonding being covalent in nature whereas the atoms in one layer are bonded to the ones in the next layer by weak Van der Waals forces. As a result, it is easy to remove them layer by layer. Ever since various methods like chemical vapor deposition [46,47], epitaxial growth and other advances in mechanical exfoliation techniques [50,51] have been used to obtain a wide variety of layered two dimensional materials. An overview of the family of two dimensional materials have been shown in the Figure 1.1.

These two dimensional materials have varied properties ranging from insulators like hexagonal boron nitride (h-BN) which has a band gap of more than 5eV to semiconductors like transition metal dichalcogenides whose band gap varies from 0.5-3.0 eV to metals like TiS_2 , VOs_2 etc [52]. The bandgap of these two dimensional materials cover a wide range of the electromagnetic spectrum, giving rise to opportunities to be used in various sectors.

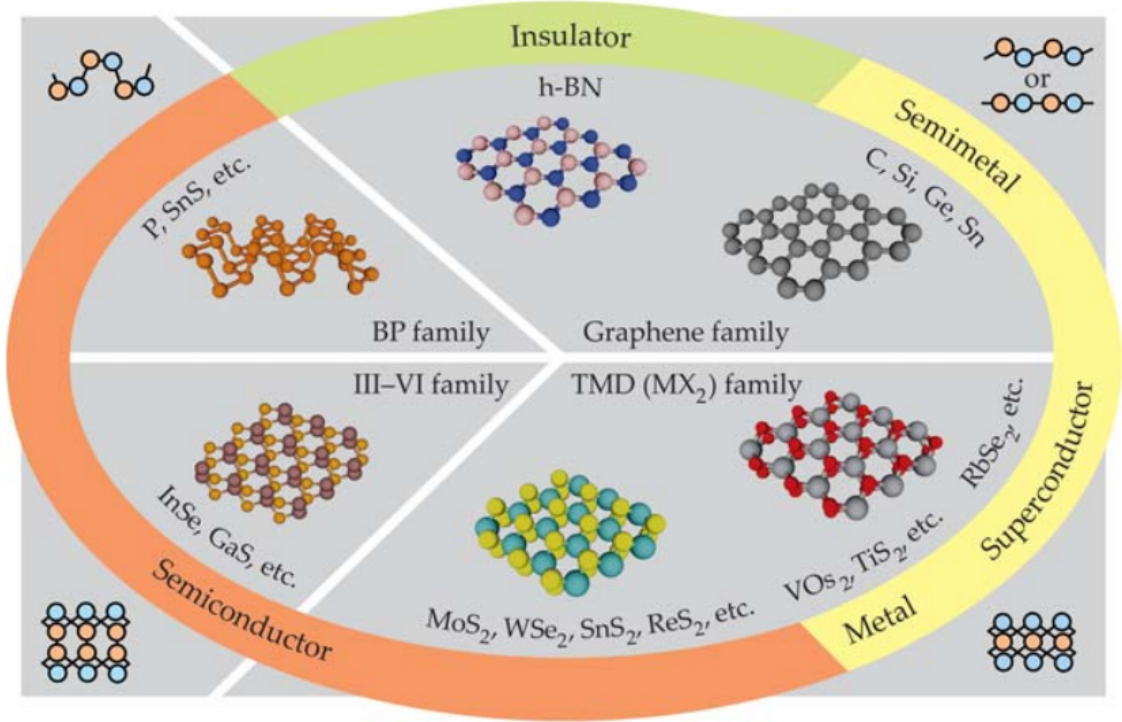


Figure 1.1: Family of two dimensional materials. Reproduced from [52]

A schematic showing different two dimensional materials with the respective part of the electromagnetic spectrum to which their bandgap belongs to, is given in Figure 1.2.

More and more materials are being explored which can have two dimensional form. Ionic semiconductors like ZnO which favors polar wurtzite structure in bulk have been studied widely for a possible two dimensional form [16]. It was seen that even in an unbiased condition, when the thin film of ZnO was grown, it prefers the polar c direction, which was unexpected because with a polar surface one would expect the surface energy to diverge beyond a few layers. It was however found out on examination that the thin films of ZnO undergoes structural transformation to form planar graphitic monolayer [17] to get rid of the problems associated with a polar surface [18]. While going from the bulk wurtzite form to the planar graphitic form, there is a reduction in coordination number which is compensated by shortening of the bondlengths in the planar graphitic form. In this thesis, we asked the question what happens when we form binary semiconductors involving elements beyond the first row of the periodic table? We tried to investigate if a graphitic phase in such cases exist at the monolayer limit by taking various examples belonging to II-VI and III-V rows of the periodic table because as we move beyond the first row the atom size of the atoms increases and hence the Coulomb repulsion between the electrons on different atoms increases in a planar graphitic form. We therefore propose a non-polar buckled structure for these semiconductors at the monolayer limit which decreases the

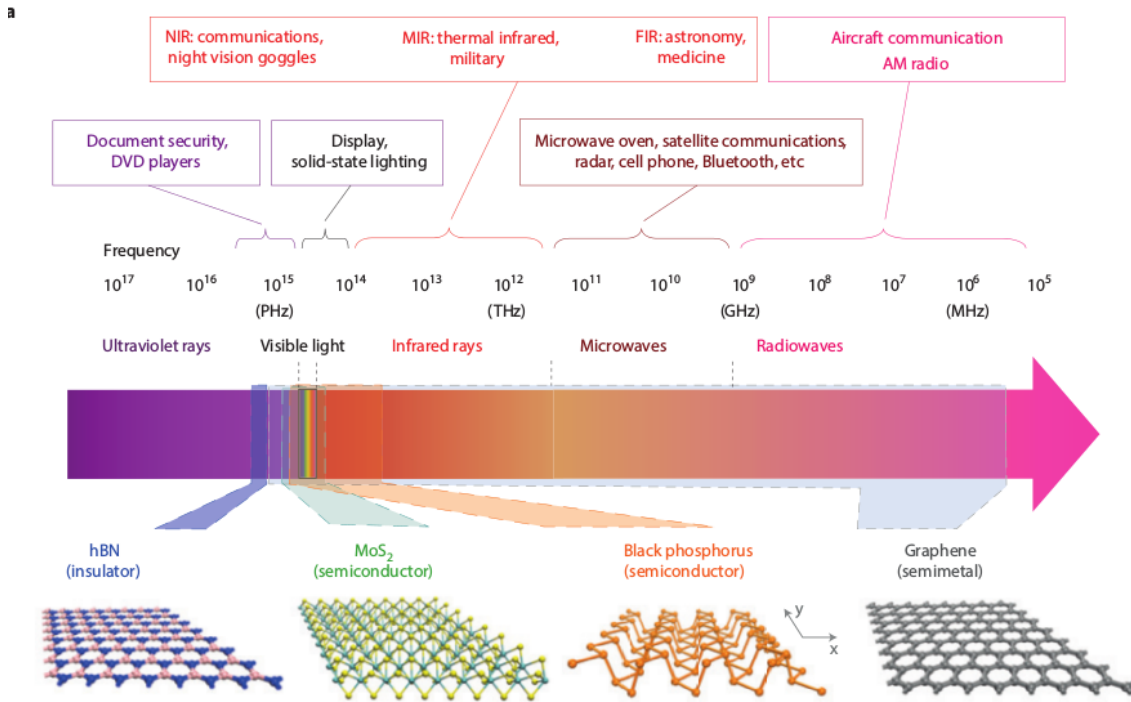


Figure 1.2: Two dimensional materials covering different range of electromagnetic spectra. Reproduced from [53]

Coulomb repulsion between the electrons on different atoms. We also looked at another way of reducing the Coulomb repulsion by applying a biaxial tensile strain on the planar graphitic form and then went on to study the effect of strain on their electronic structure and propose strain as a route to bring the valence band maxima (VBM) in these planar graphitic monolayers from Γ to K thus making the splitting of valence band maxima at K, due to spin-orbit coupling useful for application purpose.

Apart from these binary semiconductors, another class of materials, where spin-orbit coupling plays a very important role in the electronic structure are transition metal dichalcogenides and monolayers of heavy metals which are predicted to be quantum spin hall insulators, and hence they also form an important part of this thesis. We therefore discuss them in detail below with emphasis on their structure and their electronic structure.

Transition metal dichalcogenides (TMDs) is the name given to a class of materials with MX_2 as the general formula, here M represents a transition metal and X represents a chalcogen atom. These are layered Van der Waals materials, where atoms in one layer are covalently bonded to each other but each of the layers are weakly attached to each other by Van der Waals interactions. Since the layers have weak interactions between them, it is easy to separate the layers and form monolayer, bilayer, trilayer and so on. This property of TMDs is very useful, as it allows us to study their properties at extreme

two dimensional limit, whose properties differ significantly from that of the bulk. For example MoS_2 , a member of the TMD family has a bulk bandgap of 1.3 eV [57] and is an indirect bandgap semiconductor, however when we look at the same material at the monolayer limit, we see that the monolayer is a direct bandgap material with a bandgap of 1.9 eV [58]. This has been seen in a lot of other members of TMD family [60].

TMDs are found in three main types of polymorphs. These are called 1T, 2H and 3R where T represents trigonal, H hexagonal and R rhombohedral [61]. The schematics of these three polymorphs are shown in Figure 1.3.

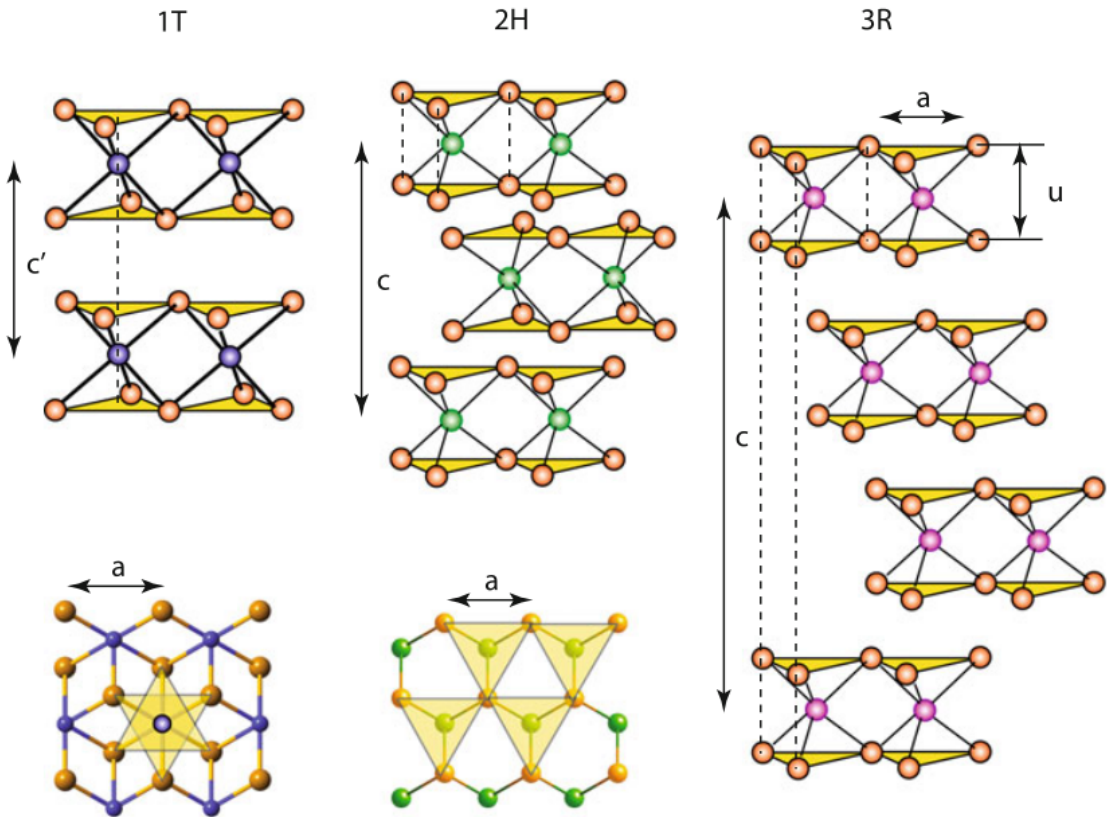


Figure 1.3: Different polymorphs of TMDs. Reproduced from [62].

In each of these cases, a and b axes are along the minimum chalcogen-chalcogen distance while the c axis is the axis perpendicular to the layers. In the 1T polymorph, the transition metal and the chalcogen atoms form an octahedra whereas in 2H and 3R they form a trigonal prismatic structure. 2H and 3R differ in the stacking pattern of different layers as can be seen in the Figure 1.3. 2H is the most common and thermodynamically most stable type of polymorph. Monolayer of 2H polymorph is called 1H. In this thesis we have mainly focused on the 1H and 2H polymorph of TMDs and looked at their electronic structure in detail with an emphasis on the role played by spin orbit coupling.

Looking at the crystal structure of 2H polymorph of these materials, we can see that in a unit cell there is one transition metal and two chalcogen atoms, where the transition metal atom is sandwiched between the chalcogen atoms. In the 2H stacking when the next layer of MX_2 is placed it is done such that the transition metal atom sits on top of the chalcogen atom as can be seen in the middle panel of Figure 1.3. Each MX_2 motif however is rotated by an angle of 60 degrees with respect to each other. Now if we look at the primitive unit cell of this structure and consider \vec{a}_1 and \vec{a}_2 to be the two primitive lattice vectors of the real space two dimensional lattice and a be the lattice constant, we can represent them as

$$\vec{a}_1 = \frac{a}{2} (\sqrt{3}\hat{x} + \hat{y}); \quad \vec{a}_2 = \frac{a}{2} (-\sqrt{3}\hat{x} + \hat{y}) \quad (1.15)$$

Also the reciprocal lattice vectors \vec{b}_1 and \vec{b}_2 of such lattice are described as

$$\vec{b}_1 = \frac{2\pi}{a} \left(\frac{\sqrt{3}}{3}\hat{k}_x + \hat{k}_y \right); \quad \vec{b}_2 = \frac{2\pi}{a} \left(-\frac{\sqrt{3}}{3}\hat{k}_x + \hat{k}_y \right) \quad (1.16)$$

The hexagonal Brillouin formed by this is shown in Figure 1.4.

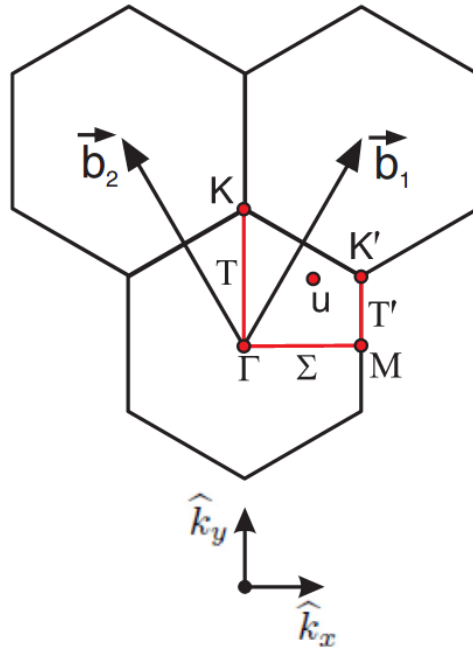


Figure 1.4: Hexagonal Brillouin zone of TMDs with high symmetry points indicated. Reproduced from [63]

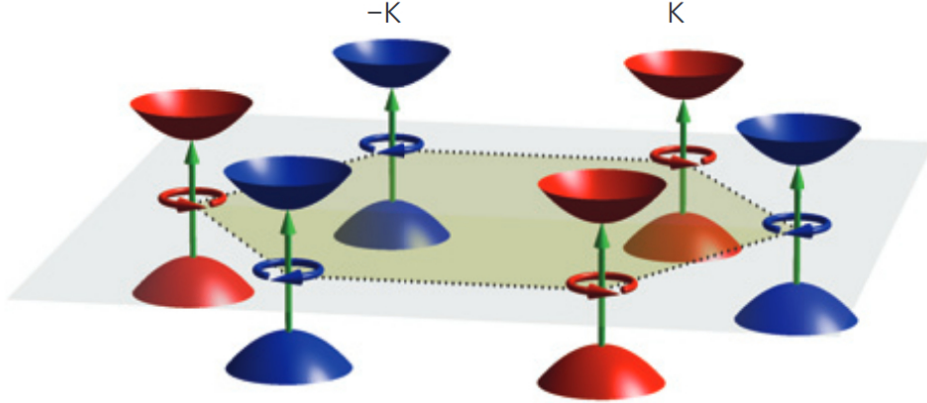


Figure 1.5: Opposite splitting of K and -K valley in monolayer of TMDs. Reproduced from [64]

This hexagonal Brillouin zone of these TMDs play a vital role in their electronic structure. In monolayer 1H TMD, which lacks inversion symmetry, the valence band maxima (VBM) lies at the edge of the Brillouin zone at K point and forms a valley. In the absence of spin-orbit interactions, these valleys are all equivalent. However, with the introduction of spin-orbit coupling as discussed in the previous section the bands at K and -K splits in the opposite direction. This has been pictorially depicted in Figure 1.5 where we can see that the VBM at K points splits up with up spin higher in energy than the down spin however at the -K point we can see that the down spin is higher in energy than the up spin [64]. Since there is no magnetism in the system and the time reversal symmetry is preserved as it can't be broken by spin-orbit interaction, the magnitude of the splitting at K and -K point is the same.

This spin-splitting of VBM in TMDs have been extensively studied both experimentally and theoretically for various members of the family [65–68]. The magnitude of the spin-splitting is different for different members [69]. In this thesis, within a tight binding model, we have addressed this aspect of difference in the magnitude of spin-splitting in different members of TMD family and have successfully captured the splitting pattern within our model. Figure 1.6 shows angle resolved photo emission spectra (ARPES) obtained for monolayer of MoS₂ along Γ to K direction by Wencan Jin et al. in 2013 [70]. Theoretically calculated bandstructure using Density Functional Theory (DFT) along Γ to K direction for MoS₂ by Z. Y. Zhu et al. in 2011 [66] is superimposed on top of it. At K we can see that there are two bands which results from the splitting of the VBM at the K point. At the -K point this splitting will be same in magnitude but opposite in direction.

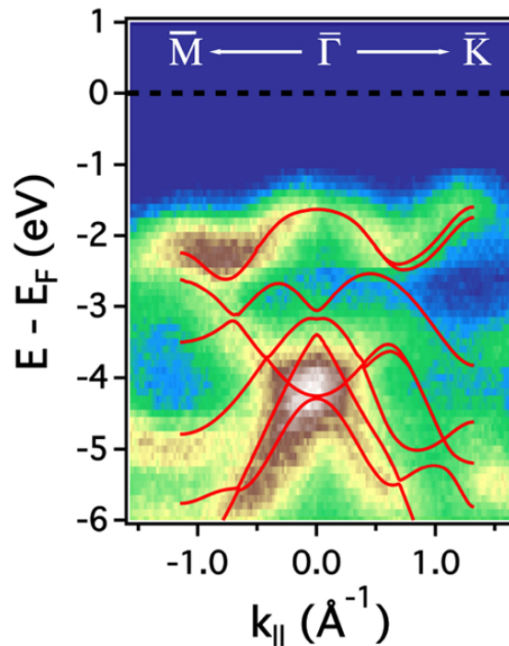


Figure 1.6: Angle Resolved Photo Emission Spectroscopy (ARPES) band dispersion of monolayer of MoS_2 in the Γ to K direction reproduced from [70] as well as bandstructure calculated from Density Functional Theory (DFT) along Γ to K direction superimposed on it reproduced from [66]

The opposite splitting of VBM at K and $-\text{K}$ allows labeling of these two valleys with different spin index, which opens up new avenues to explore exciting physics [13,14]. This introduction of new degree of freedom is referred to as valley degree of freedom and can be viewed as pseudospin. Using light of different polarization (left circularized or right circularized) one can selectively polarize each of the valleys depending on the selection rules. In monolayers of various TMDs this selective polarization of valleys has been shown experimentally by various groups [73,74]. We present results of one such study done on WSe_2 monolayer by Xiaodong Xu et al. in 2014 [64]. In this experiment, electron-hole pair in one valley is selectively excited depending on the polarization of the incident light. The results are shown in Figure 1.7

The two opposite valleys (K and $-\text{K}$) have large separation in momentum space, due to which intervalley scattering is suppressed making this a robust route to selectively polarize the valleys.

Now when we go to the bilayers of these materials, and place another of the MX_2 motif on top of the monolayer, we find that, various stackings are possible depending on the arrangement of atoms. There are five high symmetry stackings proposed in literature as shown in Figure 1.8.

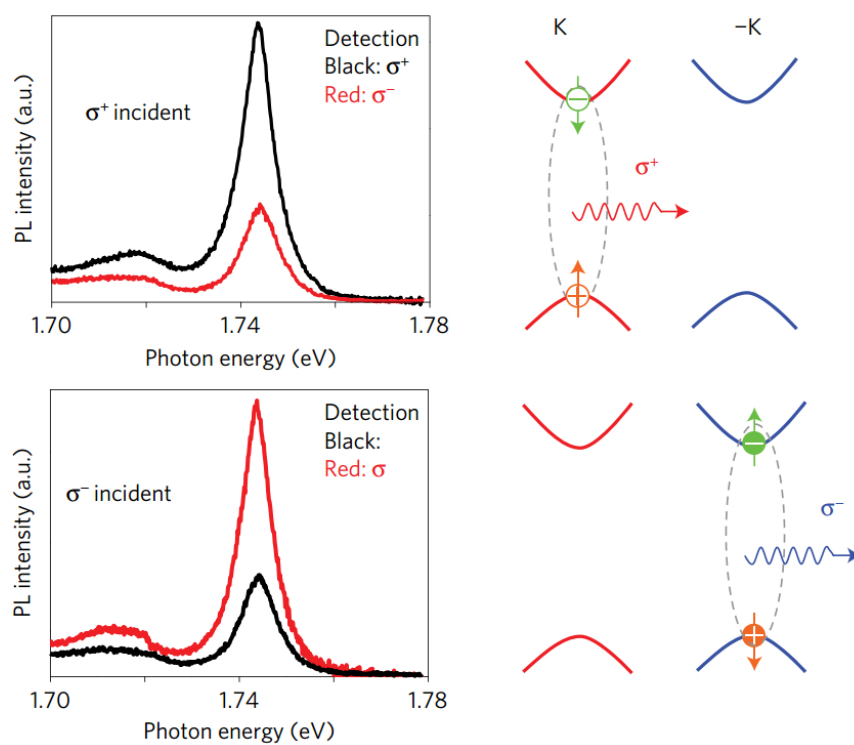


Figure 1.7: Selective valley polarization in monolayer of WSe_2 . Reproduced from [64]

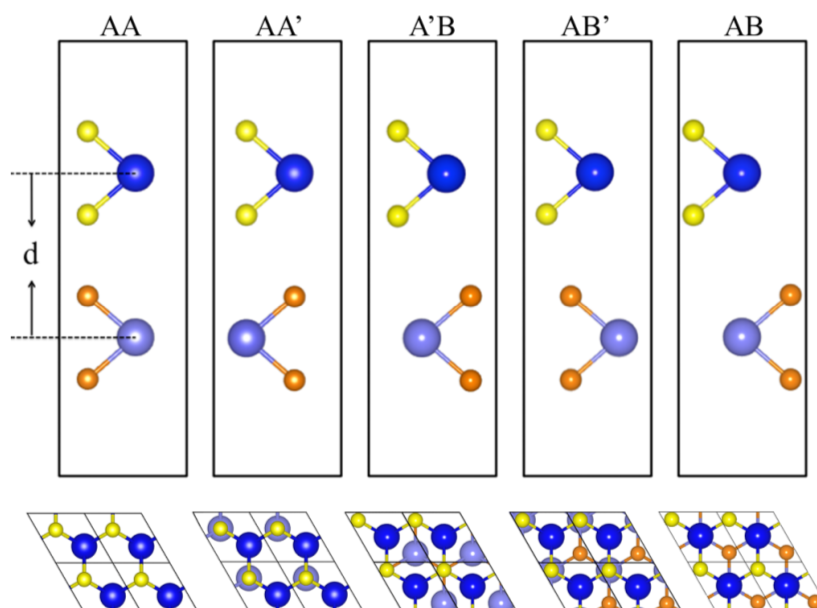


Figure 1.8: High symmetry stackings possible in bilayer TMDs. Reproduced from [75]

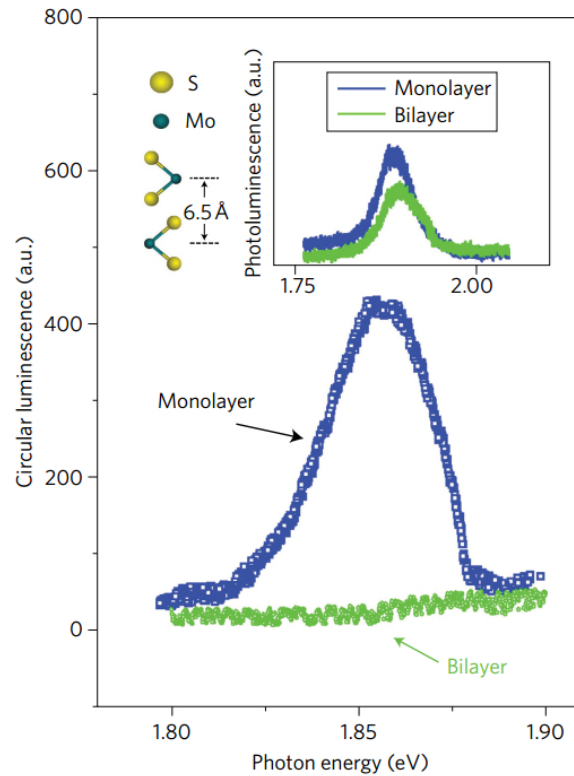


Figure 1.9: Circular luminescence for monolayer (blue) and bilayer (green) of MoS_2 . Left panel of the inset shows 2H stacking of bilayer MoS_2 . Right panel of the inset shows Photoluminescence spectra for monolayer (blue) and bilayer (green) MoS_2 . Reproduced from [76]

Considering bulk stacking(AA') in bilayers, one finds that there is a point of inversion symmetry in these structures. As a result, there is no net spin-splitting of the VBM at K and hence there is no selective polarization of the valleys. This aspect has been demonstrated experimentally, by Hualing Zeng et al. in 2012 [76]. Their results have been presented in Figure 1.9. Inset of Figure 1.9 shows photoluminescence spectra for both monolayer (blue) and bilayer (green) MoS_2 which shows excitation at 1.96 eV at 10 K in both the cases. This represents the K valley excitation when no particular polarization was selected. However the main panel of the Figure 1.9 shows spectra of monolayer (blue) and bilayer (green) at 10 K. We can see that for bilayer there is negligible emission at 1.96 eV in this case, whereas for monolayer there is a significant emission, indicating selective polarization of the valley in the case of the monolayer as opposed to the bilayer.

Circular polarization in bilayers can be achieved if the inversion symmetry associated with the 2H bilayer of TMDs can be broken. Usually to break the inversion symmetry in the bilayers, one has to apply an external electric field [77]. In this thesis, we study the twisted bilayers, where one of the layers is rotated with respect to another and hence the inversion

symmetry is broken in such bilayers. We then go on to find some interesting aspects of spin-splitting in these class of bilayers which emerge from the hexagonal symmetry of these materials.

So far we have discussed spin-valley physics in TMDs as a result of spin-orbit interactions. Spin-orbit interactions also lead to other exotic phenomena like quantum spin hall effect in some two dimensional materials. Predictions have been made for monolayers of heavy metals. These are another class of materials studied in this thesis. We therefore discuss quantum spin hall effect in detail in the next section.

1.4 Quantum Spin Hall Effect

Quantum spin hall (QSH) insulators are a class of two dimensional materials which have insulating bulk phase at the same time, edges are conducting and are protected topologically from back scattering. The edge states in these materials have two oppositely spin polarized channels for propagation. A schematic of this has been pictorially depicted in Figure 1.10.

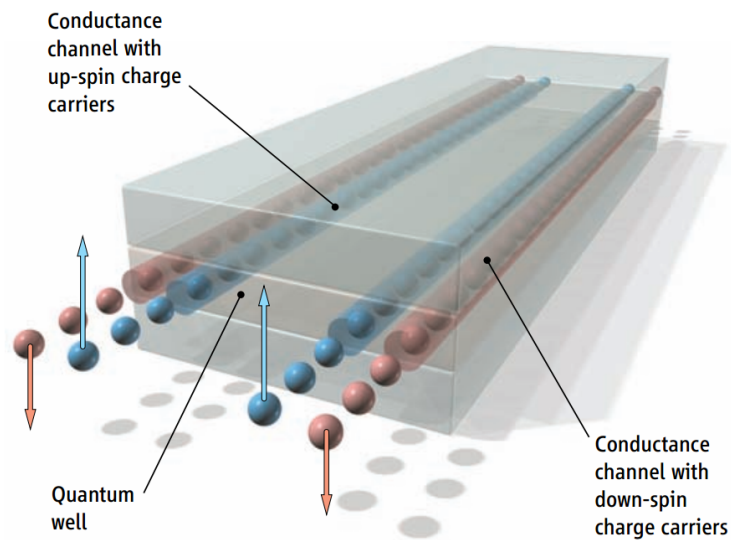


Figure 1.10: Spin polarized channels in QSH insulators. Reproduced from [78]

These class of materials have very different electronic structure from normal insulators or even quantum hall (QH) insulators. In normal insulators, the atoms keeps the outer electrons pinned and there is a gap at all momentum values as can be seen in Figure 1.11a. As a result, a band gap is present in the bandstructure of insulators. In quantum hall insulators, an external magnetic field keeps the electrons pinned and a gap is opened.

Edge states are however present in these materials and these edge states cross the gap and carry current. This can be seen in Figure 1.11b. Now in quantum spin hall insulators, a bulk gap is always present and spin-orbit coupling plays a vital role in splitting the conducting edge states into up spin and down spin channels (figure 1.11c).

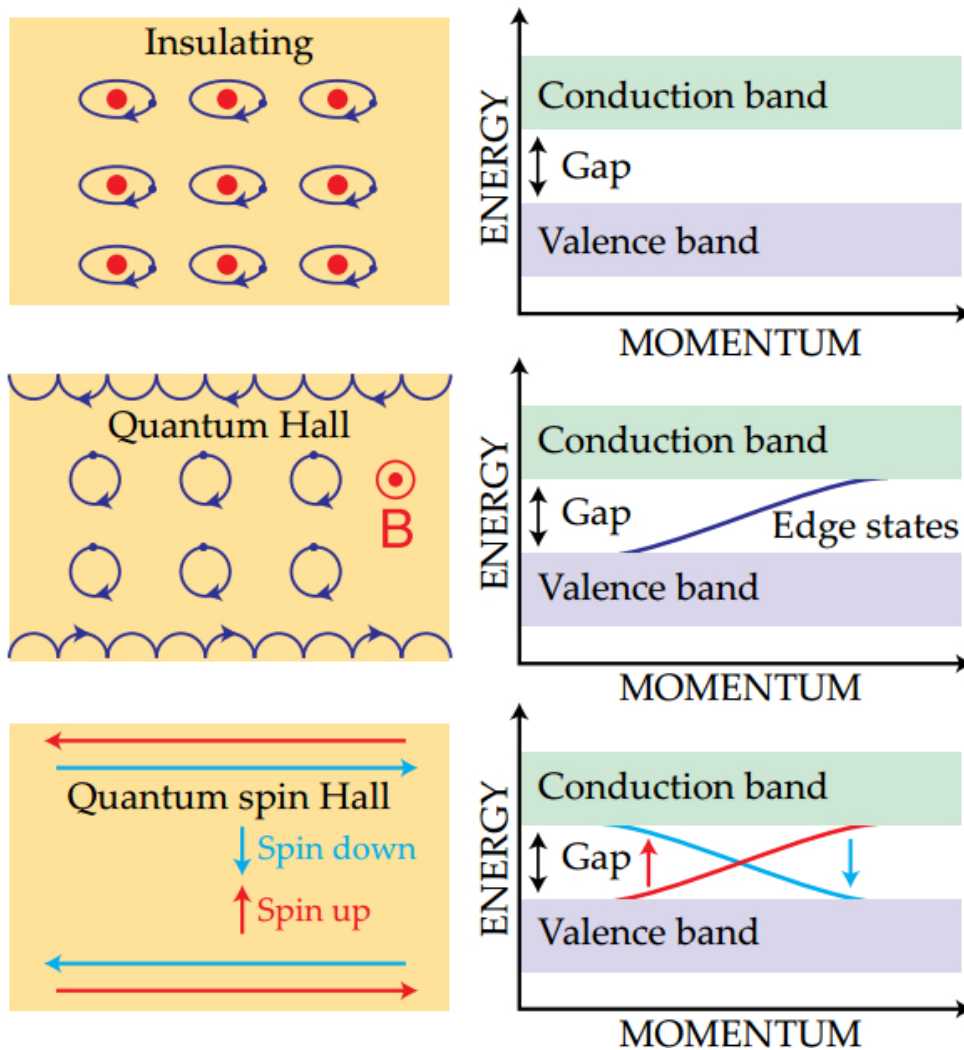


Figure 1.11: Normal insulators, quantum hall insulators and quantum spin hall insulators. Reproduced from [79].

QSH was first predicted in 2005 for graphene by Kane and Mele [48, 49]. In 2007 it was first experimentally realized in mercury telluride quantum wells [50]. After this a lot of other materials have been predicted to be QSH insulators among these are monolayers of heavy metals like bismuth, antimony etc [84, 85]. Planar graphitic monolayers of bismuth has recently been experimentally shown by F. Reis et al. in 2017 [67] to have conducting edge states residing in the bulk gap (Figure 1.12).

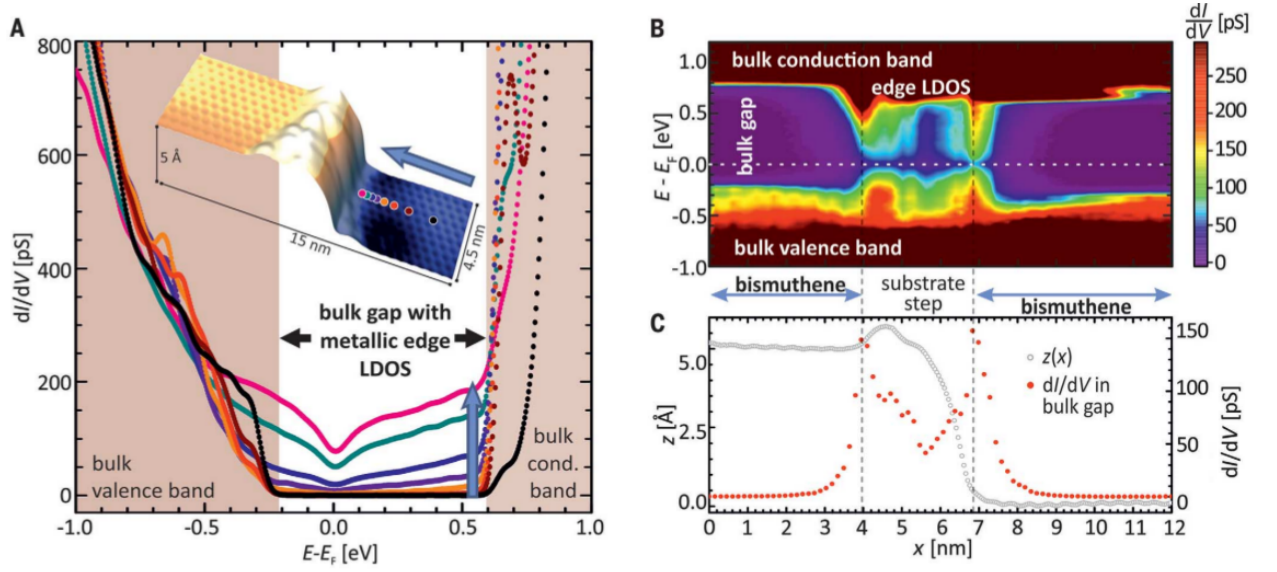


Figure 1.12: conducting edge states in graphitic monolayer of bismuth. Reproduced from [67]

In this thesis we have studied this material and its electronic structure. We reevaluate the method of realizing planar graphitic bismuthene on the substrate and propose a novel route to realize a quasi free standing bismuthene, keeping its electronic structure intact.

So far in this thesis we have discussed the effect of spin-orbit coupling on two dimensional materials like TMDs and QSH insulators, where the system does not have intrinsic magnetism. Spin-orbit interactions also play a very important role in the electronic structure and long range magnetic ordering in magnetic materials. In order to study this aspect, we chose one of the well known example in literature which is Sr_2IrO_4 . Sr_2IrO_4 is a transition metal oxide (TMO) with iridium being the transition metal (TMO). In the next section we discuss briefly the TMOs in general and some of its properties, which will help us understand the iridates better.

1.5 Transition Metal Oxides

Transition metal oxides (TMOs) constitute a very important class of solids. They exhibit a large variety of structures and properties. The unique nature of the outer d electrons is the reason for the unusual properties of TMO. The metal–oxygen bond in these compounds can vary from nearly ionic to metallic. Oxides like RuO_2 [86] and LaNiO_3 [87] are metallic whereas BaTiO_3 [88] on the other hand is highly insulating. There are some oxides which show metal to insulator transition with change in temperature, pressure, and composition,

example V_2O_3 [89]. These oxides also show variety of magnetic properties for example CrO_2 [91] and $La_{0.7}Sr_{0.3}MnO_3$ [92] are ferromagnetic whereas $NdNiO_3$ [93] and Sr_2IrO_4 [?] are antiferromagnetic. Transition metal oxides can be best described by the Hubbard model which is given by the following Hamiltonian:

$$H = -t \sum_{\langle i,j \rangle} \sum_{\sigma} (c_{j\sigma}^{\dagger} + c_{j\sigma}) + U \sum_j \hat{n}_{j\uparrow} \hat{n}_{j\downarrow} \quad (1.17)$$

Here $c_{j\sigma}^{\dagger}$ creates an electron at the j th site with spin σ and $c_{j\sigma}$ annihilates an electron from the j th site with spin σ . $\hat{n}_{j\sigma}$ is the corresponding occupation number operator. This Hubbard model is a many body Hamiltonian which describes two opposing tendencies. The first term describes the kinetic energy of the electron. It is also called the hopping term. It tends to delocalize the electrons. The second term is the electron-electron interaction term. It is here approximated by the onsite Coulomb interaction. This term wants to localize the electrons. A lot of properties of TMOs are determined by relative strength of U/t or U/W , where W is the bandwidth. In transition metal oxides if we go from $3d$ to $4d$ to $5d$ the spatial extent of the orbitals increases, as a result, the bandwidth (W) increases and U decreases. The electron electron correlation is expected to be weak as we go from $3d$ to $4d$ to $5d$ TMOs. With the prevailing picture of magnetism, which is centered around moments on the localized electrons, one doesn't expect long range magnetic ordering in $5d$ TMOs. But some of the members of $5d$ TMOs like Sr_2IrO_4 and Ba_2IrO_4 have been reported to be antiferromagnetic insulator.

In this thesis we examined one $5d$ TMO taking Sr_2IrO_4 , which belong to a class of material called iridates as an example to examine the role played by spin-orbit coupling in determining long range magnetic ordering. In these class of materials most of the electronic and magnetic properties is due to the presence of d orbitals of the iridium atom and its interaction with oxygen. In an isolated atom, the d orbitals are all degenerate but this degeneracy is lifted when this atom is placed in the local environment of a crystal. In Sr_2IrO_4 , the iridium atom sits in the middle of an octahedra with oxygen atoms at the corner. To see the effect of this environment, let us consider in plane view of two different types of d -orbitals also shown in the Figure 1.13

As we can see that the d_{xy} orbitals have a lower overlap with the neighbouring p -orbital than the $d_{x^2-y^2}$ orbital, and hence they will have a lower electrostatic energy as shown in Figure 1.14

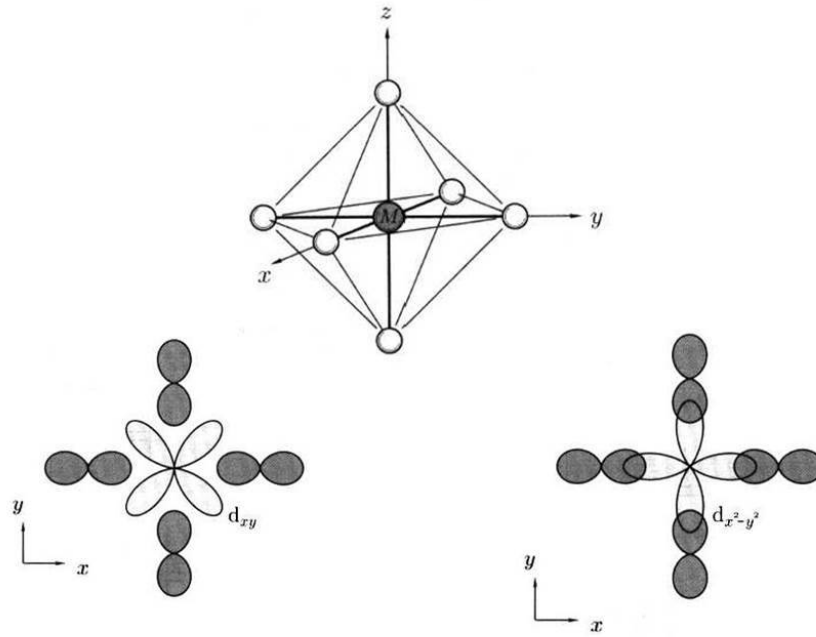


Figure 1.13: Octrahedral environment. Reproduced from [95]

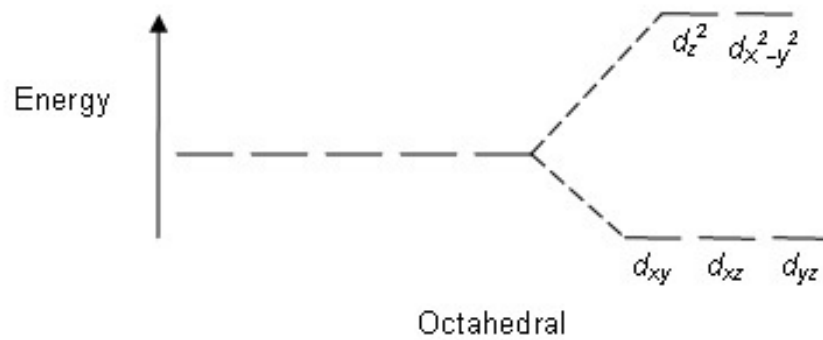


Figure 1.14: Octrahedral splitting of d-orbitals. Reproduced from [95]

In Sr_2IrO_4 , Ir is in d^5 configuration, as a result, all the electrons are present in the three degenerate t_{2g} orbitals and are widely separated by the unoccupied e_g orbitals. This octahedral crystal field splitting between t_{2g} and e_g orbitals in $5d$ compounds are large. It leads to the quenching of the orbital momentum from $l = 2$ to $l = 1$ [96]. The $l = 1$ states are characterized by $|l_z = 0\rangle = |d_{xy}\rangle$ and $|l_z = \pm 1\rangle = -\frac{1}{\sqrt{2}}(i|d_{xz}\rangle \pm |d_{yz}\rangle)$. Now on introduction of spin-orbit interactions these t_{2g} states splits into $J_{eff}=3/2$ and

$J_{eff}=1/2$ states. This plays a vital role in making this material insulating and stabilizing long range magnetic ordering and therefore has been discussed in detail later in this thesis.

1.6 Overview of the thesis

The focus of the work carried out in this thesis is on the spin-orbit effect on the electronic structure and magnetism in low dimensional compounds. Spin-orbit coupling is a relativistic effect which leads to many interesting properties in materials like spin-valley physics, spin hall effect and quantum spin hall effect etc.

In **Chapter 2** We discuss the various tools used in the work carried out in the thesis. The electronic structure of the materials discussed in this thesis has been investigated theoretically using both density functional theory which in some instances are complemented by model Hamiltonian calculations. Both these techniques have been discussed in detail in this chapter.

In **Chapter 3** We studied the effect of spin-orbit interactions in Transition metal dichalcogenides. In these materials spin-orbit interactions lead to a large spin-splitting of the valence band maximum at K at the monolayer limit where there is no inversion symmetry present. This allows a labeling of the levels with additionally the spin index. While spin-orbit interactions bring about a large spin-splitting at the K point, they cannot however bring about magnetic ordering. This would then imply that one has an equivalent but opposite spin-splitting at -K point compared to that found at K point, thereby bringing about a coupling between the spin and valley degrees of freedom in these materials with a lot of interesting consequences. However, on stacking a second layer of MoSe₂ in the same manner (2H) as found in the bulk, one finds that there is no net spin splitting, which has been attributed to inversion symmetry. An obvious route to making the bilayers useful for exploring the coupled spin and valley physics is through breaking inversion symmetry. We examined this by rotating the top layer by an angle theta with respect to the lower layer. We find that for some angles of rotation, the spin splitting vanishes, even though there is no inversion symmetry in these structures. In this chapter we demonstrate and explain a mechanism for vanishing of the spin-splitting in these systems where the hexagonal symmetry of the lattice brings about an unexpected dependence of the electronic structure on the angle of rotation.

As mentioned in the previous work, the hexagonal lattice of two dimensional materials plays an important role in its electronic structure, therefore in **Chapter 4** we looked for the structural properties of free standing II-VI and III-V semiconductors at the monolayer

limit to explore the possibility of formation of planar graphitic hexagonal lattice. In literature binary semiconductors like ZnO have been investigated for the possibility of having a stable 2D structure. It was found that it undergoes structural distortion by shortening the bondlengths to compensate for reduction in coordination number, to form a graphitic structure. The question that we asked was what happens when we go down the periodic table and the size of the atom increases? We find that the system undergoes buckling. A non-polar buckled structure was found to be favoured over a polar buckled structure. While an obvious reason for this may be traced to the contribution from dipole-dipole interactions present in the polar structure which would destabilize it with respect to the nonpolar structure, Coulomb interactions between electrons on the cations and anions are found to be the reason for the nonpolar structure to be favoured. A route to tune the Coulomb interaction between the electrons on the cations and anions is through biaxial tensile strain. This allows for a planar graphitic phase in CdS to be stabilized at just 2% tensile strain. Strain also shifts the valence band maximum from the Γ point to the K point, opening up opportunities for exploring spin-valley physics in these materials. In these semiconductors, the spin-splitting is mainly due to the anion and is of the order of 20-30 meV, we therefore we examined the possibility of stabilizing a planar graphitic structure for monolayers of heavy metal taking bismuth as an example, as an extension of this work where spin-orbit coupling becomes predominant as the size of the atom increases. Predictions have been made for monolayers of Bismuth to be a topological insulator in a graphitic lattice. The realization of such models have failed as the presence of a substrate for growing the monolayers, usually interacts with the monolayer and makes its properties substantially different from that of a freestanding one. In this work, we explored a route to quasi free-standing bismuthene. This is found to have a band gap of 0.8 eV and is a topological insulator.

So far in this thesis we have discussed the effect of spin-orbit coupling in the materials which do not show magnetism. In **Chapter 5** we investigated the role of spin-orbit coupling in stabilizing long range magnetic ordering taking iridates as an example. While studying magnetism the widely accepted idea is that it is associated with localized electrons as a result, the $3d$ TMOs which have highly correlated electrons are known to have long range magnetic ordering, but as we go to $4d$ and $5d$ TMOs the electron-electron correlation decreases and hence they are not expected to have long range magnetic ordering. In this thesis, we examine the case of $5d$ TMO taking Sr_2IrO_4 as an example and investigate the role played by spin-orbit coupling in stabilizing the long range magnetic ordering using a multiband hubbard hamiltonian. We find that for a very small range of U , antiferromagnetic state is stable.

Bibliography

- [1] G. E. Moore, *Electronics* **38** 8 (1965).
- [2] L. D. Landau and E. M. Lifshitz, *Quantum Mechanics (Non-relativistic Theory)*. 3rd. edition (Pergamon, New York), p. 198.
- [3] S. Bandyopadhyay and M. Cahay, *Introduction To Spintronics*. 1st. edition (CRC Press), p. 4.
- [4] G. E. Uhlenbeck and S. Goudsmit, *Naturwissenschaften* **13**, 953 (1925).
- [5] W. Pauli, *Zur Quantenmechanik des magnetischen Elektrons* *Zeitschrift für Physik* **43** 601-623 (1927).
- [6] W. Gerlach and O. Stern, *Zeitschrift für Physik*. **9** 1 349-352 (1922).
- [7] W. Gerlach and O. Stern, *Zeitschrift für Physik*. **9** 1 353-355 (1922).
- [8] W. Gerlach and O. Stern, *Zeitschrift für Physik*. **8** 110-111 (1922).
- [9] L. D. Anh, P. N. Hai and M. Tanaka, *Nat. Comm.* **7** 13810 (2016).
- [10] Md. A. U. Absor, H. Kotaka, F. Ishii and M. Saito *Phys. Rev. B* **94** 115131 (2016).
- [11] W.-F. Li, C. Fang, and M. A. van Huis *Phys. Rev. B* **94** 195425 (2016).
- [12] P. Carrier and S.-H. Wei *Phys. Rev. B* **70** 035212 (2004).
- [13] X. Qian, J. Liu, L. Fu, J. Li, *Science* **346** 6215 (2006).
- [14] A. Shitade, H. Katsura, J. Kunes, X.-L. Qi, S.-C. Zhang, and N. Nagaosa, *Phys. Rev. B* **102** 256403 (2009)
- [15] C.-C. Liu, W. Feng, and Y. Yao, *Phys. Rev. Lett.* **107** 076802 (2011).

-
- [16] C. Liu, T. L. Hughes, X.-L. Qi, K. Wang and S.-C. Zhang, *Phys. Rev. Lett.* **100** 236601 (2008).
- [17] A. D. Jackson. *Classical electrodynamics*. John Wiley and Sons, Inc., 1962.
- [18] E. Francisco and L. Pueyo *Phys. Rev. B* **38** 10 (1988).
- [19] L. F. Mattheiss *Phys. Rev. B* **13** 6 (1976).
- [20] E. I. Rashba, *Sov. Phys. Solid State* **2**, 1109-1122 (1960).
- [21] H. Min, J. E. Hill, N. A. Sinitsyn, B. R. Sahu, Leonard Kleinman and A. H. MacDonald *Phys. Rev. B* **74** 165310 (2006).
- [22] A. D. Caviglia, M. Gabay, S. Gariglio, N. Reyren, C. Cancellieri and J.-M. Triscone *Phys. Rev. Lett.* **104** 126803 (2010).
- [23] A. Manchon¹, H. C. Koo, J. Nitta, S. M. Frolov and R. A. Duine *Nat. Mat.* **14** 871-882 (2015).
- [24] Yu. S. Dedkov, M. Fonin, U. Rüdiger, and C. Laubschat, *Phys. Rev. Lett.* **100** 107602 (2008).
- [25] G. Dresselhaus, *Phys. Rev.* **100**, 580-586 (1955).
- [26] M. I. Dyakonov and V. Y. Kachorovski, *Fiz. Tekh. Poluprovodn.* **20**, 178 (1986) [*Sov. Phys. Semicond.* **20**, 110 (1986)].
- [27] E. A. de Andrada e Silva, *Phys. Rev. B* **46**, R 1921 (1992)
- [28] R. Eppenga and M. F. H. Schuurmans, *Phys. Rev. B* **37**, 10923 (1988).
- [29] X. Zhang, Q. Liu¹, J.-W. Luo, A. J. Freeman and Alex Zunger *Nat. Phys.* **10** 387-393 (2014).
- [30] T. Vossmeier, L. Katsikas, M. Giersig, I. G. Popovic, K. Diesner, A. Chemseddine, A. Eychemueller and H. Weller, *J. Phys. Chem.* **98** 7665 (1994).
- [31] V. L. Colvin, M. C. Schlamp and A. P. Alivisatos, *Nature*, **370**, 354 (1994).
- [32] M. A. Schreuder, K. Xiao, I. N. Ivanov, S. M. Weiss and S. J. Rosenthal, *Nano Lett.*, **10**, 573 (2010).
- [33] P. Crespo, R. Litran, T. Rojas, M. Multigner, J. De la Fuente, J. Sanchez-Lopez, M. Garcia, A. Hernando, S. Penades, A. Fernandez, *Phys. Rev. Lett.*, **93**, 87204 (2004).

- [34] E. Roduner, Chem. Soc. Rev. **35**, 583-592 (2006).
- [35] K. Koga, T. Ikeshoji and K. Sugawara, Phys. Rev. Lett., **92** 115507 (2004).
- [36] A. Corma and H. Garcia Chem. Soc. Rev. **37**, 2096-2126 (2008)
- [37] H. M. T. Galvis, J. H. Bitter, C. B. Khare, M. Ruitenbeek, A. I. Dugulan, K. P. de Jong Science. **335**, 835-838 (2012)
- [38] P. Harrison, Quantum wells, wires and dots: Theoretical and computational physics, John Wiley and Sons, USA (2000).
- [39] T. Takagahara and K. Takeda, Phys. Rev. B **46** 23 (1991).
- [40] A. Balandin and K. L. Wang, J. App. Phys. **84** 11 (1998).
- [41] Y. Tian, Md. R. Sakr, J. M. Kinder, D. Liang, M. J. MacDonald, R. L. J. Qiu, H.-J. Gao and X. P. A. Gao, Nano Lett. **12** 6492-6497 (2012).
- [42] P. Tyagi, S. M. Arveson and W. A. Tisdale, J. Phys. Chem. Lett. **84** 6 1911-1916 (2015).
- [43] J.G. Bednorz and K.A. Mueller, Z. Phys. B. **64** 2 189-193 (1986).
- [44] K. S. Novoselov, A. K. Geim, S. V. Morozov, D. Jiang, Y. Zhang, S. V. Dubonos, I. V. Grigorieva, and A. A. Firsov, Science **306**, 666 (2004).
- [45] K. S. Novoselov, A. K. Geim, S. V. Morozov, D. Jiang, M. I. Katsnelson, I. V. Grigorieva, S. V. Dubonos, and A. A. Firsov, Nature **438**, 197 (2005).
- [46] Z. Chen, W. Ren, L. Gao, B. Liu, S. Pei and H.-M. Cheng Nat. Mat. **10**, 424-428 (2011).
- [47] C. Mattevi, H. Kima and M. Chhowalla J. Mater. Chem., **21**, 3324-3334 (2011).
- [48] S. A. Chambers, Surface Science Reports, **39**, 150-180 (2000).
- [49] H. Amano, N. Sawaki, I. Akasaki and Y. Toyoda, Appl. Phys. Lett. **48**, 353 (2019)
- [50] S. Das, H.-Y Chen, A. V. Penumatcha, J. Appenzeller, Nano Lett. **13** 100-105 (2012)
- [51] G. A. Salvatore, N. Munzenrieder, C. Barraud, L. Petti, C. Zysset, et al. ACS Nano **7** 8809-8815 (2013).

- [52] P. Ajayan, P. Kim and K. Banerjee, *Physics Today* **69** 38 (2016).
- [53] F. Xia, H. Wang, D. Xiao, M. Dubey and A. Ramasubramaniam, *Nature Photonics* **8** 899-907 (2014).
- [54] F. Claeyssens, C. L. Freeman, N. Allan, Y. Sun, M. N. R. Ashfolda, and J. H. Harding, *Journal of Mater. Chem.*, **15**, 139 (2005).
- [55] C. Tusche, H. L. Meyerheim, and J. Kirschner, *Phys. Rev. Lett.* **99**, 026102 (2007).
- [56] B. Rakshit, and P. Mahadevan, *Phys. Rev. Lett.* **107** , 085508 (2011).
- [57] G. L. Frey, S. Elan, M. Homyonfer, Y. Feldman and R. Tenne, *Phys. Rev. B* **57**, 11 (1997).
- [58] C. Lee, H. Yan, L. E. Brus, T. F. Heinz, J. Hone and S. Ryu, *ACS Nano* **4**, 5 (2010).
- [59] A. Splendiani, L. Sun, Y. Zhang, T. Li, J. Kim, C.-Y. Chim, G. Galli and F. Wang, *Nano Lett.* **10**, 1271-1275, (2010).
- [60] W. S. Yun, S. W. Han, S. C. Hong, I. G. Kim and J. D. Lee, *Phys. Rev. B* **85**, 033305 (2012).
- [61] R. J. Toh, Z. Sofer, J. Luxa, D. Sedmidubsky and M. Pumera, *Chem. Commun.* **53**, 3054, (2017)
- [62] A. V. Kolobov and J. Tominaga, *Two-Dimensional Transition-Metal Dichalcogenides*, (Springer Nature, Switzerland 2016)
- [63] J. Ribeiro-Soares, R. M. Almeida, E. B. Barros, P. T. Araujo, M. S. Dresselhaus, L. G. Cancado, and A. Jorio, *Phys. Rev. B* **90**, 115438 (2014).
- [64] X. Xu, W. Yao, D. Xiao and T. F. Heinz, *Nat. Phys.* **10**, 343-350 (2014).
- [65] D. W. Latzke, W. Zhang, A. Suslu, T.-R. Chang, H. Lin, H.-T. Jeng, S. Tongay, J. Wu, A. Bansil and A. Lanzara, *Phys. Rev. B* **91** 235202 (2015).
- [66] Z. Y. Zhu, Y. C. Cheng, and U. Schwingenschogl, *Phys. Rev. B* **84**, 153402 (2011).
- [67] N. Alidoust, G. Bian, S.-Y. Xu, R. Sankar, M. Neupane, C. Liu, I. Belopolski, D.-X. Qu, J. D. Denlinger, F.-C. Chou and M. Z. Hasan, *Nat. Comm.* **5**, 4673 (2014).
- [68] S. Tongay, W. Fan, J. Kang, J. Park, U. Koldemir, J. Suh, D. S. Narang, K. Liu, J. Ji, J. Li, R. Sinclair, and J. Wu, *Nano Lett.* **14**, 3185-3190 (2014).

- [69] G.-B. Liu, D. Xiao, Y. Yao, X. Xude and W. Yao, *Chem. Soc. Rev.* **44**, 2643 (2015).
- [70] W. Jin, P.-C. Yeh, N. Zaki, D. Zhang, J. T. Sadowski, A. Al-Mahboob, A. M. van der Zande, D. A. Chenet, J. I. Dadap, I. P. Herman, P. Sutter, J. Hone, and R. M. Osgood Jr., *Phys. Rev. Lett.* **111**, 106801 (2013).
- [71] A. M. Jones, H. Yu, N. J. Ghimire, S. Wu, G. Aivazian, J. S. Ross, B. Zhao, J. Yan, D. G. Mandrus, D. Xiao, W. Yao and X. Xu, *Nature Nanotechnology* **8** 634-638 (2013).
- [72] D. Xiao, G.-B. Liu, W. Feng, X. Xu, and W. Yao, *Phys. rev. Lett.* **108**, 196802 (2012).
- [73] L. Yang, N. A. Sinitsyn, W. Chen, J. Yuan, J. Zhang, J. Lou and S. A. Crooker, *Nature Physics*, **11**, 830-835 (2015).
- [74] L. Du, Q. Zhang, B. Gong, M. Liao, J. Zhu, H. Yu, R. He, K. Liu, R. Yang, D. Shi, L. Gu, F. Yan, G. Zhang, and Q. Zhang, *Phys. Rev. Lett.* **97**, 115445 (2018).
- [75] J. He, K. Hummer and C. Franchini, *Phys. Rev. B* **89**, 075409 (2014).
- [76] H. Zeng, J. Dai, W. Yao, D. Xiao, X. Cui *Nat. Nanotech.* **7**, 290 (2012).
- [77] A. M.-S. Sanchez, D. Sangalli, L. Wirtz, and A. Marini, *Nano Lett.* **17**, 4549-4555 (2017).
- [78] M. König, S. Wiedmann, C. Brüne, A. Roth, H. Buhmann, L. W. Molenkamp, X.-L. Qi and S.-C. Zhang, *Science*. **318**, 766-770 (2007).
- [79] C. Day, *Physics Today*, **61**, 1, 19-22 (2008).
- [80] C. L. Kane and E. J. Mele *Phys. Rev. Lett.* **95**, 226801 (2005)
- [81] C. L. Kane and E. J. Mele *Phys. Rev. Lett.* **95**, 146802 (2005)
- [82] M. König, S. Wiedmann, C. Brüne, A. Roth, H. Buhmann, L. W. Molenkamp, Xiao-Liang Qi, and Shou-Cheng Zhang *Science* **318**, 766 (2007).
- [83] F. Reis, G. Li, L. Dudy, M. Bauernfeind, S. Glass, W. Hanke, R. Thomale, J. Schäfer, R. Claessen, *Science* **357** 287 (2014).
- [84] F. Dominguez, B. Scharf, G. Li, J. Schäfer, R. Claessen, W. Hanke, R. Thomale, and E. M. Hankiewicz, *Phys. Rev. B* **98**, 161407(R) (2018).

-
- [85] G. Wang, R. Pandey, and S. P. Karna, *ACS Appl. Mater. Interfaces*, **7**, 11490-11496 (2015).
- [86] Z. H. Zhu, J. Stremper, R. R. Rao, C. A. Occhialini, J. Pellicciari, Y. Choi, T. Kawaguchi, H. You, J. F. Mitchell, Y. Shao-Horn and R. Comin, *Phys. Rev. Lett.* **122**, 017202 (2019).
- [87] H. Guo¹, Z.W. Li, L. Zhao, Z.Hu, C.F. Chang, C.-Y. Kuo, W. Schmidt, A. Piovano, T.W. Pi, O. Sobolev, D.I. Khomskii, L.H. Tjeng and A.C. Komarek, *Nat. Comm.* **9**, 43 (2018).
- [88] X. Guo, *Phys. Chem. Chem. Phys.* **16**, 20420 (2014).
- [89] J. Trastoy, Y. Kalcheim, J. del Valle, I. Valmianski, and Ivan K. Schuller, *J. Mater. Sci.* **58** 9131-9137 (2018).
- [90] I. V. Solovyev, I. V. Kashin, and V. V. Mazurenko, *Phys. Rev. B* **92** 144407 (2015).
- [91] B. J. Kim, Hosub Jin, S. J. Moon, J.-Y. Kim, B.-G. Park, C. S. Leem, Jaejun Yu, T. W. Noh, C. Kim, S.-J. Oh, J.-H. Park, V. Durairaj, G. Cao and E. Rotenberg, *Phys. Rev. Lett.* **101**, 076402 (2008).
- [92] Michael C. Martin and G. Shirane, *phys. Rev. B* **53**, 21 (1996).
- [93] J. L. Garcia-Munoz, M. A. G. Aranda, J. A. Alonso and M. J. Martinez-Lope *Phys. Rev B* **79** 134432 (2009).
- [94] B. J. Kim, Hosub Jin, S. J. Moon, J.-Y. Kim, B.-G. Park, C. S. Leem, Jaejun Yu, T. W. Noh, C. Kim, S.-J. Oh, J.-H. Park, V. Durairaj, G. Cao, and E. Rotenberg, *Phys. Rev. Lett.* **101**, 076402 (2008).
- [95] S. Blundell *Magnetism in Condensed matter* (Oxford University Press, 2001).
- [96] A. Abragam and B. Bleaney. *Electron paramagnetic resonance of transition ions*. International series of monographs on physics. Clarendon P., (1970).

Chapter 2

Theoretical Concepts

2.1 Many body Hamiltonian

Properties of materials are determined by the electrostatic interaction between its electrons and nuclei. The theory for such system of interacting charged particle is inherently quantum mechanical and can be described by time independent many body Schrödinger equation of the form $H\Psi = E\Psi$, Here H is the many body Hamiltonian and Ψ is a set of eigenstates of H . The many body Hamiltonian, H can be written as follows

$$H = -\frac{\hbar^2}{2m_e} \sum_i \nabla_i^2 - \frac{\hbar^2}{2M_I} \sum_I \nabla_I^2 + \frac{1}{2} \sum_{i \neq j} \frac{e^2}{|\mathbf{r}_i - \mathbf{r}_j|} + \frac{1}{2} \sum_{I \neq J} \frac{Z_I Z_J e^2}{|\mathbf{R}_I - \mathbf{R}_J|} - \sum_{i,I} \frac{Z_I e^2}{|\mathbf{R}_I - \mathbf{r}_i|} \quad (2.1)$$

In the above equation, the variables i and j belong to the electrons whereas the indices I and J correspond to the nuclei. r_i and R_I are the positions of the electrons and the nuclei respectively. Similarly m_e and M_I represent the masses of the electrons and nuclei respectively. $Z_I e$ is the charge of the nucleus and \hbar is the Plank's constant.

The first two term in Equation 2.1 are the kinetic energies of the electrons and the nuclei respectively where, ∇_i^2 and ∇_I^2 are the Laplacians containing second order derivatives with respect to electronic and ionic coordinates respectively. The third term is the electron electron repulsion term whereas the fourth term is the repulsive interaction term between the nuclei. The fifth and the last term is the interaction between electrons and nuclei. Equation 2.1 can thus be written in a compact form as

$$H = T_e(\mathbf{r}) + T_N(\mathbf{R}) + V_{ee}(\mathbf{r}) + V_{NN}(\mathbf{R}) + V_{eN}(\mathbf{r}, \mathbf{R}) \quad (2.2)$$

Solving this many body Hamiltonian using Schrödinger equation should give us all the properties of the system. However because of the large number of coordinates involved and the coupled degrees of freedom, solving this many body Schrödinger equation becomes almost impossible except for very simple cases like an isolated hydrogen atom. One therefore has to make appropriate approximations and then solve it by various methods like hartree [1], hartree-fock [2,3] and density functional theory [4]. In the coming sections we will discuss one such approximation called the Born-Oppenheimer Approximation and then the various methods to solve the many body Schrödinger equation.

2.2 Born-Oppenheimer Approximation

Born-Oppenheimer Approximation is named after Max Born, and J. Robert Oppenheimer [5]. It is a simple yet very powerful approximation and takes advantage of the fact that the mass of the nucleus is ~ 1800 times heavier than the mass of the electron. As a result the nucleus can be considered fixed compared to the motion of the electrons. This allows the electron and nuclei degrees of freedom to be decoupled. As the nuclei are considered fixed, their kinetic energy can be ignored and the nuclear-nuclear interaction term can be considered a constant and is called Madelung energy [6]. Thus the Hamiltonian after Born-Oppenheimer Approximation becomes

$$H_{BOA}^{ele} = T_e(\mathbf{r}) + V_{ee}(\mathbf{r}) + V_{eN}(\mathbf{r}, \mathbf{R}) \quad (2.3)$$

This adiabatic approximation simplifies the problem to a great extent but it still remains a many body problem. Solution to this Hamiltonian is still very difficult because of large number of variables and the presence of electron-electron interaction term. Various attempts have been made to further simplify the problem and solve it. In the coming section, we will discuss one such theory, namely the density functional theory (DFT) which describes the theory of the analysis used in this thesis.

2.3 Density Functional Theory (DFT)

In 1964 Hohenberg and Kohn developed an approach for solving the many body system and describing its ground state properties, which aimed at reducing the number of variables involved. It was called the density functional theory (DFT) [11]. We have used DFT as implemented within the Vienna ab-initio simulation package (VASP) [9, 10, 25, 26] to

study the electronic structure of materials. The fundamental proposition of DFT is the introduction of a new variable called the electron density. It is defined as the probability of finding an electron in a specific location around an atom or molecule. Density for an N-electron system is derived from normalized N-electron wavefunction. Mathematically, density for an N-electron system can be given as

$$n(\mathbf{r}_i) = N \int \Psi^*(\mathbf{r}_1, \dots, \mathbf{r}_i, \dots, \mathbf{r}_N) \Psi(\mathbf{r}_1, \dots, \mathbf{r}_i, \dots, \mathbf{r}_N) d\mathbf{r}_1 d\mathbf{r}_2 \dots d\mathbf{r}_{(i-1)} d\mathbf{r}_{(i+1)} \dots d\mathbf{r}_N \quad (2.4)$$

For a normalized wavefunction, integrating the electron density over all space, gives the number of electrons. The electron density is a physical quantity and it can be measured experimentally in X-ray diffraction experiments [12]. There are many advantages of using the electron density. It is a function of only three spatial variables where as the many body wave-function $\Psi(\mathbf{r})$ is a function of $3N$ variable with N being the number of electrons. The two theorems proposed by Hohenberg and Kohn form the backbone upon which the modern formulation of density functional theory rests [11].

The term defined in Equation 2.4 is single particle density. Similar to this, we can also define two particle density as follows

$$n(\mathbf{r}_i, \mathbf{r}_j) = N \int \Psi^*(\mathbf{r}_1, \dots, \mathbf{r}_i, \dots, \mathbf{r}_j, \dots, \mathbf{r}_N) \Psi(\mathbf{r}_1, \dots, \mathbf{r}_i, \dots, \mathbf{r}_j, \dots, \mathbf{r}_N) d\mathbf{r}_1 d\mathbf{r}_2 \dots d\mathbf{r}_{(i-1)} d\mathbf{r}_{(i+1)} \dots d\mathbf{r}_{(j-1)} d\mathbf{r}_{(j+1)} \dots d\mathbf{r}_N \quad (2.5)$$

This two particle density can be understood as probability that an electron exists at a point \mathbf{r}_i , in presence of another electron at a point \mathbf{r}_j

If we have a system, where two electrons are completely uncorrelated then $n(\mathbf{r}_i, \mathbf{r}_j)$ can simply be written as the product of two single particle density as

$$n(\mathbf{r}_i, \mathbf{r}_j) = n(\mathbf{r}_i)n(\mathbf{r}_j) \quad (2.6)$$

But that is unfortunately not the case in real systems and we do have electron-electron interactions, as a result, this two particle density can be written as

$$n(\mathbf{r}_i, \mathbf{r}_j) = n(\mathbf{r}_i)n(\mathbf{r}_j)\Delta n(\mathbf{r}_i, \mathbf{r}_j) \quad (2.7)$$

where $\Delta n(\mathbf{r}_i, \mathbf{r}_j)$ is the correlation term and is important in the density functional theory formulation.

2.3.1 The Hohenberg-Kohn Theorems

Theorem 1 : The ground state electron density of a system of interacting particles in an external potential $V_{ext}(\mathbf{r})$ is uniquely determined.

Proof: Let us assume two different external potentials, $V_1(\mathbf{r})$ and $V_2(\mathbf{r})$ differing by a constant and giving rise to the same ground state density $n(\mathbf{r})$. We further assume that Ψ_1 and Ψ_2 be the the ground state wave-function corresponding to $V_1(\mathbf{r})$ and $V_2(\mathbf{r})$ and they both gives the same ground state charge density $n(\mathbf{r})$.

Now, the Schrödinger equation corresponding to these two N electron systems is given by

$$E_1 = \langle \Psi_1 | H_1 | \Psi_1 \rangle \quad (2.8)$$

Now since Ψ_2 does not corresponds to the ground state wave-function of H_1 , we can write the following inequality

$$E_1 < \langle \Psi_2 | H_1 | \Psi_2 \rangle \quad (2.9)$$

we can further write

$$\langle \Psi_2 | H_1 | \Psi_2 \rangle = \langle \Psi_2 | H_2 | \Psi_2 \rangle + \langle \Psi_1 | [H_1 - H_2] | \Psi_1 \rangle \quad (2.10)$$

So now we can write the above inequality as

$$E_1 < \langle \Psi_2 | H_2 | \Psi_2 \rangle + \langle \Psi_1 | [H_1 - H_2] | \Psi_1 \rangle \quad (2.11)$$

$$E_1 < E_2 + \langle \Psi_1 | [V_1(\mathbf{r}) - V_2(\mathbf{r})] | \Psi_1 \rangle \quad (2.12)$$

Similarly we can obtain an expression for E_2

$$E_2 < E_1 + \langle \Psi_2 | [V_2(\mathbf{r}) - V_1(\mathbf{r})] | \Psi_2 \rangle \quad (2.13)$$

Adding the above two equations we have

$$E_1 + E_2 < E_2 + E_1 + \langle \Psi_1 | [V_1(\mathbf{r}) - V_2(\mathbf{r})] | \Psi_1 \rangle + \langle \Psi_2 | [V_2(\mathbf{r}) - V_1(\mathbf{r})] | \Psi_2 \rangle \quad (2.14)$$

And can be written as

$$E_1 + E_2 < E_2 + E_1 + \langle \Psi_1 | [V_1(\mathbf{r}) - V_2(\mathbf{r})] | \Psi_1 \rangle + \langle \Psi_2 | [V_2(\mathbf{r}) - V_1(\mathbf{r})] | \Psi_2 \rangle \quad (2.15)$$

or

$$E_1 + E_2 < E_2 + E_1 + \langle \Psi_1 | [V_1(\mathbf{r}) - V_2(\mathbf{r})] | \Psi_1 \rangle - \langle \Psi_2 | [V_1(\mathbf{r}) - V_2(\mathbf{r})] | \Psi_2 \rangle \quad (2.16)$$

Writing this in terms of density we get the following inequality

$$E_1 + E_2 < E_2 + E_1 + \int n(\mathbf{r})[V_1(\mathbf{r}) - V_2(\mathbf{r})]d^3r - \int n(\mathbf{r})[V_1(\mathbf{r}) - V_2(\mathbf{r})]d^3r \quad (2.17)$$

which finally gives

$$E_1 + E_2 < E_2 + E_1 \quad (2.18)$$

This is a contradiction and hence proves that two different external potentials can not give the same ground state density.

Theorem 2 : The statement of the second theorem is that the energy of a system can be written as functional of the charge density ($E[n(\mathbf{r})]$). The global minimum of this functional obtained variationally represents its ground state energy and the electron density that minimizes this energy ($E[n(\mathbf{r})]$) is the ground state charge density of the system.

We therefore can say that if $n_0(\mathbf{r})$ represents the ground state electron density of a system then we have the following relation for any other density, $n'(\mathbf{r})$ which is not a ground state density.

$$E[n'(\mathbf{r})] \geq E[n_0(\mathbf{r})] \quad (2.19)$$

2.3.2 Kohn-Sham Formulation

For a set of N interacting electrons, in an external potential V_{ext} , we have the Hamiltonian as $H = T_e + V_{ee} + V_{ext}$. The total energy of the system as a functional of its electron density can be written as

$$E[n(\mathbf{r})] = T[n(\mathbf{r})] + E_{ee}[n(\mathbf{r})] + \int n(\mathbf{r})V_{ext}(\mathbf{r})d^3r \quad (2.20)$$

In the above equation, $T[n(\mathbf{r})]$ is the kinetic energy term and $E_{ee}[n(\mathbf{r})]$ is the electron-electron interaction term. Together, these two can be written as

$$F[n(\mathbf{r})] = T[n(\mathbf{r})] + E_{ee}[n(\mathbf{r})] \quad (2.21)$$

This term $F[n(\mathbf{r})]$ is called Hohenberg-Kohn functional. At this point we try to express both the terms of the Equation 2.21 in terms of density.

$$E_{ee}[n(\mathbf{r})] = \frac{1}{2} \int \int d\mathbf{r}_i d\mathbf{r}_j \frac{n(\mathbf{r}_i)n(\mathbf{r}_j)}{|\mathbf{r}_i - \mathbf{r}_j|} + \Delta E_{ee} \quad (2.22)$$

or

$$E_{ee}[n(\mathbf{r})] = E_H[n(\mathbf{r})] + \Delta E_{ee} \quad (2.23)$$

where

$$E_H[n(\mathbf{r})] = \frac{1}{2} \int \int d\mathbf{r}_i d\mathbf{r}_j \frac{n(\mathbf{r}_i)n(\mathbf{r}_j)}{|\mathbf{r}_i - \mathbf{r}_j|} \quad (2.24)$$

It is called the Hartree energy and represents the classical electron-electron interaction term. ΔE_{ee} in Equation 2.23 is due to the electron-electron correlation discussed in Equation 2.7. Writing the kinetic energy term $T[n(\mathbf{r})]$ in term of density becomes very difficult because of the presence of a derivative term. This poses a difficult situation and in order to solve this, the N -electron interacting system was replaced by a hypothetical system of non-interacting system of N -electron. The electron density can now be written in terms of these hypothetical non-interacting single electron wave-functions $\phi_i(\mathbf{r})$ known as Kohn-sham orbitals [13] as

$$n(\mathbf{r}) = 2 \sum_{i=1}^N \phi_i^*(\mathbf{r})\phi_i(\mathbf{r}) \quad (2.25)$$

One important point to note here is that these Kohn-Sham orbitals are purely mathematical entities and have no physical interpretation. The multiplicative factor of 2 in the Equation 2.25 is due to the fact that we are dealing here without the spin degree of freedom as a result each of the orbital is occupied with two electrons each with opposite spins. Now we can express the kinetic energy of the N electron interacting system term using Kohn-Sham orbitals as a sum of kinetic energies of the individual Kohn-Sham orbitals then this will not be equal to the kinetic energy of the real system. In order to tackle this we write the kinetic energy term as

$$T[n(\mathbf{r})] = T_0[n(\mathbf{r})] + \Delta T \quad (2.26)$$

Now, both ΔE_{ee} and ΔT from Equation 2.23 and Equation 2.26 respectively are due to electron electron correlations and can be clubbed together in one term as

$$E_{XC}[n(\mathbf{r})] = \Delta E_{ee} + \Delta T \quad (2.27)$$

Now using Equation 2.23, Equation 2.26 and Equation 2.27 we can rewrite Equation 2.21 as

$$F[n(\mathbf{r})] = T_0[n(\mathbf{r})] + E_H[n(\mathbf{r})] + E_{XC}[n(\mathbf{r})] \quad (2.28)$$

Now, minimizing the energy functional given in Equation 2.20 with respect to the charge density one can obtain the ground state energy. This minimization needs to be done with the constraint that the total number of electrons remain conserved, i.e.

$$\int n(\mathbf{r})d\mathbf{r} = N \quad (2.29)$$

This minimization is done using the Lagrange multiplier method. It can be written as follows

$$\frac{\delta}{\delta n(\mathbf{r})} \left[T_0[n(\mathbf{r})] + E_{ee}[n(\mathbf{r})] + \int n(\mathbf{r})V_{ext}(\mathbf{r})d^3r - \mu_L \left(\int n(\mathbf{r})d^3r - N \right) \right] = 0 \quad (2.30)$$

or

$$\frac{\delta}{\delta n(\mathbf{r})} \left[T_0[n(\mathbf{r})] + E_H[n(\mathbf{r})] + E_{XC}[n(\mathbf{r})] + \int n(\mathbf{r})V_{ext}(\mathbf{r})d^3r - \mu_L \left(\int n(\mathbf{r})d^3r - N \right) \right] = 0 \quad (2.31)$$

Here μ_L is the Lagrange multiplier constant. Equation 2.30 can also be written as

$$\mu_L = \frac{\delta T_0[n(\mathbf{r})]}{\delta n(\mathbf{r})} + \frac{E_H[n(\mathbf{r})]}{\delta n(\mathbf{r})} + \frac{E_{XC}[n(\mathbf{r})]}{\delta n(\mathbf{r})} + V_{ext}(\mathbf{r}) \quad (2.32)$$

This can also be written as

$$\mu_L = \frac{\delta T_0[n(\mathbf{r})]}{\delta n(\mathbf{r})} + V_{XC}(\mathbf{r}) + V_H(\mathbf{r}) + V_{ext}(\mathbf{r}) \quad (2.33)$$

with $V_{XC}(\mathbf{r}) = \frac{E_{XC}[n(\mathbf{r})]}{\delta n(\mathbf{r})}$ and $V_H(\mathbf{r}) = \frac{E_H[n(\mathbf{r})]}{\delta n(\mathbf{r})}$ We now return to the minimization of the total energy functional and find out that using variational principle, when Equation 2.30

is minimized, it leads to a self consistent Kohn-Sham equation using Kohn-Sham orbitals

$$\left[-\frac{\hbar^2}{2m}\nabla^2 + V_{ext}(\mathbf{r}) + V_H(\mathbf{r}) + V_{XC}(\mathbf{r})\right]\phi_i(\mathbf{r}) = \epsilon_i\phi_i(\mathbf{r}) \quad (2.34)$$

All the terms in Equation 2.34 are known except for the $V_{XC}(\mathbf{r})$ term. $V_H(\mathbf{r}) + V_{XC}(\mathbf{r})\phi_i(\mathbf{r})$ is sometime referred to as V_{KS} . Thus the Kohn-Sham equation is also written as

$$\left[-\frac{\hbar^2}{2m}\nabla^2 + V_{KS}(\mathbf{r})\right]\phi_i(\mathbf{r}) = \epsilon_i\phi_i(\mathbf{r}) \quad (2.35)$$

The most important point to remember here is that, the ground state charge density which is obtained by solving the Kohn-Sham equation is the exact ground state charge density of the system, even though the Kohn-Sham equation is written for the non-interacting system. To get the ground state charge density, we need the ground state Kohn-Sham wavefunction and to get this we need to solve the Kohn-Sham equation. To solve the Kohn-Sham equation we need $V_H(\mathbf{r})$ which is the Hartree potential, but again this $V_H(\mathbf{r})$ depends on the electron density and hence we need to know the electron density. So in order to solve this loop problem, charge density is calculated in an iterative way in the following way. (At this point we will not worry about the form of $V_{XC}(\mathbf{r})$). We will discuss it in the next section).

Step 1 : An initial trial electron density, $n(r)$ is defined.

Step 2 : Using the trial electron density, Kohn-Sham equations are solved to find the single particle wave function ϕ_i .

Step 3 : From the Kohn-Sham single particle wave function obtained above, electron density is calculated $n_{KS}(\mathbf{r}) = 2 \sum_i \phi_i^*(\mathbf{r})\phi_i(\mathbf{r})$.

Step 4 : The calculated electron density in the previous step, $n_{KS}(\mathbf{r})$ is compared with the initial trial electron density, $n(\mathbf{r})$. If the two densities satisfy some convergence criteria and are consistent, then the electron density thus calculated is the ground state electron density otherwise we go to step 2 with the updated electron density $n_{KS}(\mathbf{r})$.

This has been pictorially shown in Figure 2.1

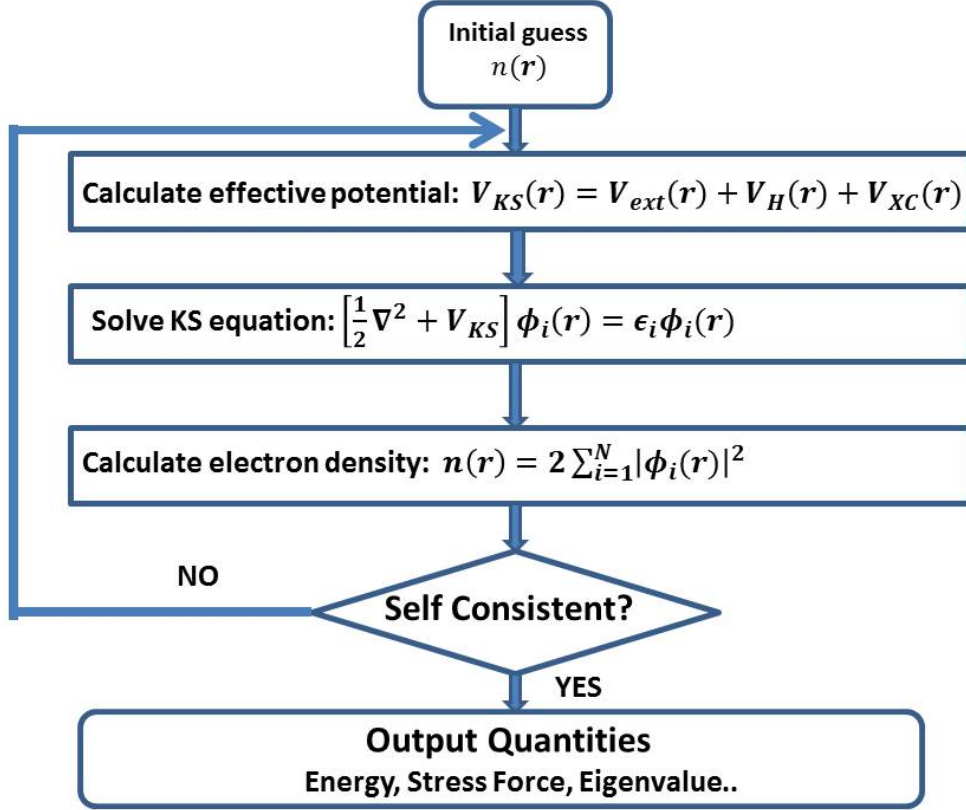


Figure 2.1: Flowchart of DFT

2.3.3 Approximations For Exchange Correlation Functional

As said earlier, we have so far not discussed the functional form of $V_{KS}(\mathbf{r})$. In this section, we discuss the various functional forms of $E_{XC}[n(\mathbf{r})]$, which lead to the calculation of $V_{KS}(\mathbf{r})$.

Local Density Approximation(LDA): Local density approximation(LDA) was proposed by Hohenberg and Kohn in their original DFT paper [11]. In this approximation, the exchange-correlation energy of a system at each point in space is approximated by the exchange-correlation energy of a homogeneous electron gas(HEG) of the same density observed at that point. This form of the exchange correlation energy is precisely known only for the homogeneous electron gas. LDA uses the local density, and the exchange-correlation energy functional is written as,

$$E_{XC}^{LDA}[n(\mathbf{r})] = \int n(\mathbf{r}) \varepsilon_{XC}^{HEG}(\mathbf{r}) d^3r \quad (2.36)$$

here $\varepsilon_{XC}^{HEG}(\mathbf{r})$, is the exchange-correlation energy density and it corresponds to a homogeneous electron gas of density $n(\mathbf{r})$. $\varepsilon_{XC}^{HEG}(\mathbf{r})$ can be separated into exchange and correlation parts as,

$$\varepsilon_{XC}^{HEG}(\mathbf{r}) = \varepsilon_X^{HEG}(\mathbf{r}) + \varepsilon_C^{HEG}(\mathbf{r}). \quad (2.37)$$

Dirac derived this exchange part $\varepsilon_X^{HEG}(\mathbf{r})$ analytically [14]. But the analytic expression for the other term ε_C^{HEG} is known only in the limits of high [15,16] and low densities [17].

Generalized Gradient Approximation (GGA) :

The major drawback of LDA approximation is that it is not appropriate in a non uniform density which results from the formation of spatially directed bonds. The next approximation considered to take care of this drawback is the generalized gradient approximation (GGA), where the exchange-correlation energy is expressed in terms of both the local density and the gradient of the electron density. The exchange-correlation functional under GGA approximation can be expressed as,

$$E_{XC}^{GGA}[n(\mathbf{r})] = \int n(\mathbf{r}) \varepsilon_{XC}^{HEG}[n(\mathbf{r}), |\nabla n(\mathbf{r})|] d^3r \quad (2.38)$$

Perdew and co-workers initiated the most important work towards development of GGA functional [18]. Ever since many improvement have been done. Some popular form of GGA functionals are Perdew and Wang [19], Becke-Lee-Yang-Par (B-LYP) [20–22] and Burke and Enzerhof (PBE) [23] functionals.

Hybrid Functionals :

Hybrid functionals is another approximation for the exchange-correlation functional which has contributions from the exact (hartree-fock) energy with a GGA functional. It has a general form as

$$E_{XC}^{Hybrid} = \alpha(E_X^{HF} - E_X^{GGA}) + E_X^{GGA} \quad (2.39)$$

here E_X^{HF} is the hartree-fock exchange energy and is a non-local quantity. One needs to know the value of ϕ_i at all points in order to evaluate it at a particular point of the configuration space. The amount of exact-exchange mixing is determined by the coefficient α and is fitted semi empirically. One such functional is HSE, named after J. Heyd, G. E. Scuseria, and M. Ernzerhof [24]. These functionals are computationally expensive because of their non-local nature but at the same time they are expected to be

more accurate in the case of strongly correlated electron systems because of their large self-interaction correlation.

2.4 Numerical Approximations for DFT Calculations

We use DFT to calculate the electronic structure of materials which have many electrons using Kohn-Sham equations. Analytically it is not possible to solve this problem, however, we can solve it mathematically iteratively, using some approximations. As a result of these approximations, errors enter into the solution. Therefore it is important to work towards getting a well converged solution. In this section we will briefly discuss some of the numerical approximations used in DFT calculations.

2.4.1 Plane Wave Basis and Cut-off Energy

We need an appropriate basis set in order to solve the Kohn-Sham equations. We calculate electronic structure of crystals which have periodic arrangement of atoms as a result, we can write single particle electronic states in a periodic system for the non-interacting electrons as follows in terms of Bloch states [25].

$$\phi_{\mathbf{k}}(\mathbf{r}) = e^{i\mathbf{k}\cdot\mathbf{r}} u_{\mathbf{k}}(\mathbf{r}) \quad (2.40)$$

here, $u_{\mathbf{k}}(\mathbf{r})$ is the lattice periodicity given as $u_{\mathbf{k}}(\mathbf{r} + n_1\mathbf{a}_1 + n_2\mathbf{a}_2 + n_3\mathbf{a}_3) = u_{\mathbf{k}}(\mathbf{r})$, where \mathbf{a}_1 , \mathbf{a}_2 and \mathbf{a}_3 are the lattice vectors of the material and n_1 , n_2 , n_3 are integers. Now Bloch's theorem allows Fourier expansion of $u_{\mathbf{k}}(\mathbf{r})$ (because of its periodicity) in terms of plane waves as

$$u_{\mathbf{k}}(\mathbf{r}) = \sum_{\mathbf{G}} C_{\mathbf{G}} e^{i\mathbf{G}\cdot\mathbf{r}} \quad (2.41)$$

\mathbf{G} here is the reciprocal lattice vector and is defined in terms of reciprocal unit lattice vectors as $\mathbf{G} = m_1\mathbf{b}_1 + m_2\mathbf{b}_2 + m_3\mathbf{b}_3$. Now using the definition of $u_{\mathbf{k}}(\mathbf{r})$ from Equation 2.41 into the Equation 2.40 we get

$$\phi_{\mathbf{k}}(\mathbf{r}) = \sum_{\mathbf{G}} C_{\mathbf{G}+\mathbf{k}} e^{i(\mathbf{G}+\mathbf{k})\cdot\mathbf{r}} \quad (2.42)$$

Equation 2.42 represent infinite sum of plane waves whose kinetic energy is given as $E = \frac{\hbar^2}{2m} |\mathbf{k} + \mathbf{G}|^2$. For practical purpose therefore, we need to truncate the infinite sum

given in Equation 2.42. We do this by defining a cut off for the kinetic energy

$$E_{cut} = \frac{\hbar^2}{2m} G_{cut}^2 \quad (2.43)$$

Now once we have defined a cut off kinetic energy, only those plane wave whose kinetic energies are lower than the defined cut off energy are included in the basis set. One can minimize the error due to this approximation by increasing the cut off kinetic energy till the total energy calculated using that cut off does not show significant variations.

2.4.2 *K*-Space Integrations

While performing DFT calculations, we evaluate *k*-space integrals with the form [26].

$$g = \frac{V_{cell}}{(2\pi)^3} \int_{BZ} g(\mathbf{k}) d\mathbf{k} \quad (2.44)$$

Here volume of the unit cell of the material is given as V_{cell} , we evaluate the value of $g(\mathbf{k})$ within the Brillouin zone at some finite *k*-points with appropriate weights in order to evaluate the integral given in the Equation 2.44, numerically. It is important to choose the *k*-points properly so that the total energy of the system does not depend on the selection of *k*-point. One way to do this is to increase the *k*-point grid and calculate the total energy of the system until the changes in the total energy is insignificant.

2.4.3 Pseudopotential and Frozen core approximation

The electrons in an atom can be divided into two categories, the core electrons which are tightly bound to the nucleus and the valence electrons which are free to move. The kinetic energy of the core electrons are higher than that of the valence electrons and also their wavefunction show very rapid oscillations. In a solid however the physical and chemical properties are mainly decided by the valence electrons and the core electrons do not take part in bond formation. As the kinetic energy of the core electrons are higher, we need a very large cut off energy to represent them and this is computationally very expensive. So one approach to solve this problem can be to approximate the core electrons which replicates its effect in a way that the physical and chemical properties of the material remain unaltered.

One popular approach to handle this is the pseudopotential approximation. In this approximation, the core electron density is replaced by a smoothed function. This smooth function is chosen such that the properties of the system are best described. This is also

called the frozen core approximation. If we represent the core and the valence electrons by $|\psi^c\rangle$ and $|\psi^v\rangle$ respectively, then a smooth valence function can be constructed which are orthogonal to the core states as follows

$$|\phi^v\rangle = |\psi^v\rangle + \sum_c \alpha_c \psi^c(\mathbf{r}) \quad (2.45)$$

here the orthogonality condition $\alpha_c = \langle \psi^c | \phi^v \rangle$ can be used to determine α_c . Now, the Schrödinger equation gets modified as

$$\left[H + \sum_c (\epsilon^v - \epsilon^c) |\psi^c\rangle \langle \psi^c| \right] |\phi^v\rangle = \epsilon^v |\phi^v\rangle \quad (2.46)$$

hence a pseudo Hamiltonian is given as

$$H^{PH} = \left[H + \sum_c (\epsilon^v - \epsilon^c) |\psi^c\rangle \langle \psi^c| \right] \quad (2.47)$$

The eigenvalues of this Hamiltonian should be the same as the original Hamiltonian. The potential (called pseudo-potential) corresponding to this is given as

$$V^{PP} = V + \sum_c (\epsilon^v - \epsilon^c) |\psi^c\rangle \langle \psi^c| \quad (2.48)$$

Here, the nuclear potential is represented by V . The second term in Equation 2.48 is a correction term due to the repulsion of valence electrons by the core electrons. A schematic illustration of pseudo potential approach is given in Figure 2.2

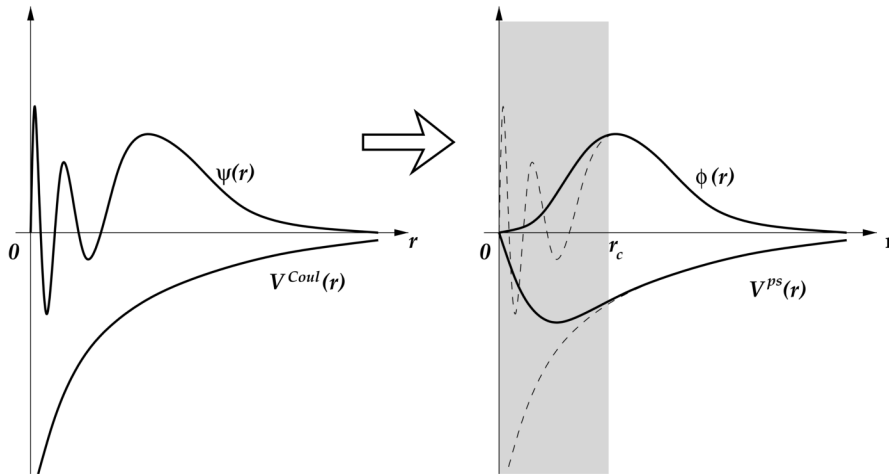


Figure 2.2: Core electrons in pseudo potential approach. Reproduced from [27]

From the figure, we can see that beyond a cut off radius, the pseudo potential as well as the pseudo wavefunction is identical to the all electron potential and the all electron wavefunction respectively. The cut off radius is defined by a cut off energy. One of the main point kept in mind while developing a pseudo-potential is to construct a pseudo wavefunction which is as smooth as possible and yet should be able to produce accurate results. Constant efforts are being made to generate pseudo-potentials which are accurate as well as efficient. Generation of norm-conserving pseudo-potential is one such example. In this method, the all-electron and pseudo-wave function agree beyond some chosen radius (r_c). Sometimes the pseudo-potentials generated using this method not smoother than the all-electron one because of the criteria imposed by norm-conserving. This difficulty was removed by the introduction of ultrasoft pseudo potentials (USPP) by Vanderbilt in 1990 [28]. The norm-conserving criteria was relaxed for this pseudo-potential. This method requires a very small planewave cut off and hence a very small number of plane wave. The major drawback of using USPP is that their construction requires a lot of empirical parameters. Another popular approach developed to overcome the disadvantages of USPP is projector augmented-wave(PAW) method.

2.4.4 Projector Augmented-Wave(PAW) Method

PAW or Projector augmented plane wave method is a pseudo potential technique developed by Blöchl [29]. Kresse and Joubert later adapted this method for plane-wave calculations [30]. This approximation is based on construction of all electron wave function using which all the integrals are calculated. These integrals are calculated as a combination of smooth functions which extend throughout space as well as contributions from localized muffin tin orbitals [31,32]. As a result, we have the total wavefunction which is a combination of wavefunction of the valence states $\tilde{\psi}_i^v(\mathbf{r})$ as well as a linear transformation function which relates an all electron valence function $\psi_j^v(\mathbf{r})$ to $\tilde{\psi}_i^v(\mathbf{r})$. This is given as

$$\psi_j^v(\mathbf{r}) = \tilde{\psi}_j^v(\mathbf{r}) + \sum_i (|\phi_i\rangle - |\tilde{\phi}_i\rangle) \langle \tilde{p}_i | \tilde{\phi}_i \rangle \quad (2.49)$$

In this equation, the atomic site \mathbf{R} is represented by the index i . $|\tilde{p}_i\rangle$ represents the projector functions for localized pseudo partial wave. They satisfy the orthogonality condition, $\langle \tilde{p}_i | \tilde{\phi}_j \rangle = \delta_{i,j}$. In this formalism, the all electron charge density can be derived from Equation 2.49 as

$$n(\mathbf{r}) = \tilde{n}(\mathbf{r}) + n^1(\mathbf{r}) - \tilde{n}^1(\mathbf{r}), \quad (2.50)$$

here,

$$\tilde{n}(\mathbf{r}) = \sum_i f_i |\tilde{\psi}_i(\mathbf{r})|^2 \quad (2.51)$$

$$n^1(\mathbf{r}) = \sum_i f_i \sum_{j,k} \langle \tilde{\psi}_i | \tilde{p}_j \rangle \phi_j(\mathbf{r}) \phi_k(\mathbf{r}) \langle \tilde{p}_k | \tilde{\psi}_i \rangle \quad (2.52)$$

$$\tilde{n}^1(\mathbf{r}) = \sum_i f_i \sum_{j,k} \langle \tilde{\psi}_i | \tilde{p}_j \rangle \tilde{\phi}_j(\mathbf{r}) \tilde{\phi}_k(\mathbf{r}) \langle \tilde{p}_k | \tilde{\psi}_i \rangle \quad (2.53)$$

In this expressions, f_i 's are the occupancies of the eigenstates $\tilde{\psi}_i$. $\tilde{n}(\mathbf{r})$ is the pseudo-charge density which is calculated from the pseudo-wavefunctions with plane wave basis. $n^1(\mathbf{r})$ and $\tilde{n}^1(\mathbf{r})$ are the onsite charge densities localized within the augmented sphere around each atom. The total energy of the system when calculated from these charge densities can also be divided into three parts.

2.5 Van der Waals Correction: DFT-D2 Method

In order to capture the long range non-local interactions such as van der Waals (vdW) interactions, there are various estimations made in DFT because the standard exchange correlation functionals used do not describe these interactions in DFT. One such approach is DFT-D2, which was proposed by Grimme [22]. This approach is also called DFT-D. In this method a semi-empirical term which is attractive in nature is added to the total energy calculated by DFT. This term takes into consideration the long range dispersive forces and hence we call it E_{disp} . The total energy thus becomes

$$E_{DFT-D2} = E_{DFT} + E_{disp} \quad (2.54)$$

E_{disp} is given as

$$E_{disp} = -s_6 \sum_{i=1}^{N_{at}-1} \sum_{j=i+1}^{N_{at}} \frac{C_6^{ij}}{R_{ij}^6} f_{damp}(R_{ij}) \quad (2.55)$$

The number of atoms in the system here is given here by N_{at} . s_6 is a scaling factor and it depends on the exchange correlation functional used. R_{ij} is the distance between the atoms i and j . C_6^{ij} are the dispersion coefficients between the i -th and the j -th atom. The singularity at R_{ij} can be avoided by the damping factor $f_{damp}(R_{ij})$ and is given as

$$f_{damp}(R_{ij}) = \frac{1}{e^{-d(R_{i,j}/R_0^{i,j}-1)}} \quad (2.56)$$

For a pair of atoms, $R_0^{i,j}$ is the cut off radius. It is given as the average of their van der Waal radii [34]. d is a damping constant and it determines the steepness of the function [22].

2.6 Tight Binding Method

Tight binding method is an extension of Blöch's linear combination of atomic orbital (LCAO) [25]. It is a simple approach for calculation of bandstructure of solids. The tight binding method rests on the assumption that the wavefunctions can be expanded in terms of atomic orbitals which are assumed to be tightly binded to their sites. In order to understand this method let us consider a set of atomic wavefunctions $\phi_l(\mathbf{r} - \mathbf{t}_i)$ in a primitive cell. Here $\phi_i(r)$ represents the atomic state of the i -th atom. Also here different types of orbitals are labeled using the index l . Now using Blöch's theorem, we construct a basis set for a periodic lattice as

$$\Phi_{\mathbf{k},l,i}(\mathbf{r}) = \frac{1}{\sqrt{N}} \sum_{\mathbf{R}'} e^{i\mathbf{k}\cdot\mathbf{R}'} \phi_l(\mathbf{r} - \mathbf{t}_i - \mathbf{R}') \quad (2.57)$$

here the total number of unit cell is given by N and \mathbf{R}' represents the translation vectors. Now using these basis functions we write the single particle eigenstates as follows

$$\psi_{\mathbf{k}}^n(\mathbf{r}) = \sum_{\mathbf{i},\mathbf{j}} c_{\mathbf{k},l,i} \Phi_{\mathbf{k},l,i}(\mathbf{r}) \quad (2.58)$$

In the above equation the coefficients $c_{k,l,i}$ can be evaluated by the assumption that $\psi_{\mathbf{k}}^n(\mathbf{r})$ are solutions of the single particle Schrödinger's equations

$$H^{SP} \psi_{\mathbf{k}}^n(\mathbf{r}) = \epsilon_{\mathbf{k}} \psi_{\mathbf{k}}^n(\mathbf{r}), \quad (2.59)$$

$$\sum_{i,l} \{ \langle \Phi_{\mathbf{k},m,j} | H^{SP} | \Phi_{\mathbf{k},m,j} \rangle - \epsilon_{\mathbf{k}} \langle \Phi_{\mathbf{k},m,j} | \Phi_{\mathbf{k},m,j} \rangle \} c_{k,l,i}^n = 0 \quad (2.60)$$

considering orthogonality condition

$$\langle \psi_{\mathbf{k}}^n(\mathbf{r}) | \psi_{\mathbf{k}'}^n(\mathbf{r}) \rangle = \delta(\mathbf{k} - \mathbf{k}') \quad (2.61)$$

The values of \mathbf{k} and \mathbf{k}' are restricted to the first Brillouin zone. In order to solve this, we need to solve the integral in the above equation. This can be done as follows

$$\begin{aligned}
\langle \Phi_{\mathbf{k},l,i} | \Phi_{\mathbf{k},l,i} \rangle &= \frac{1}{N} \sum_{\mathbf{R}', \mathbf{R}''} e^{i\mathbf{k} \cdot (\mathbf{R}' - \mathbf{R}'')} \langle \phi_m(\mathbf{r} - \mathbf{t}_j - \mathbf{R}'') | \phi_l(\mathbf{r} - \mathbf{t}_i - \mathbf{R}') \rangle \quad (2.62) \\
&= \frac{1}{N} \sum_{\mathbf{R}, \mathbf{R}'} e^{i\mathbf{k} \cdot \mathbf{R}} \langle \phi_m(\mathbf{r} - \mathbf{t}_j) | \phi_l(\mathbf{r} - \mathbf{t}_i - \mathbf{R}) \rangle \\
&= \sum_{\mathbf{R}} e^{i\mathbf{k} \cdot \mathbf{R}} \langle \phi_m(\mathbf{r} - \mathbf{t}_j) | \phi_l(\mathbf{r} - \mathbf{t}_i - \mathbf{R}) \rangle \quad (2.63)
\end{aligned}$$

In the Equation 2.63, the bracket term is the overlap integral of the atomic orbitals on the neighboring sites. We then calculate the expectation value using these basis set as

$$\langle \Phi_{\mathbf{k},m,j} | H | \Phi_{\mathbf{k},l,i} \rangle = \sum_{\mathbf{R}} e^{i\mathbf{k} \cdot \mathbf{R}} \langle \phi_m(\mathbf{r} - \mathbf{t}_j) | H | \phi_l(\mathbf{r} - \mathbf{t}_i - \mathbf{R}) \rangle \quad (2.64)$$

The Orthogonality condition

$(\langle \phi_m(\mathbf{r} - \mathbf{t}_j) | \phi_l(\mathbf{r} - \mathbf{t}_i - \mathbf{R}) \rangle = \delta_{l,m} \delta_{i,j} \delta(\mathbf{R}))$ should be used to get the solution. These integrals are very difficult to compute. For certain periodic lattices they can be however parametrized in terms of Slater-Koster parameters [35].

In this thesis we set up the tight binding hamiltonian for a system at various \mathbf{k} points in the Brillouin zone using an initial guess value for the Slater-Koster parameters and the on site energies. After that a least squared error minimization fitting was done to fit the eigenvalues obtained from ab-initio calculation at those \mathbf{k} points. Using this process we obtain the values for the Slater-Koster parameters as well as the on site energies.

Bibliography

- [1] D. R. Hartree, The wave mechanics of an atom with non-coulombic central field: Parts I, II, III. Proc. Cambridge Phil. Soc. **24**, 89, 111, 426 (1928).
- [2] V. Fock, Z. Phys. **61**, 126 (1930).
- [3] J. C. Slater, Phys. Rev. **34**, 1293 (1929).
- [4] W. Kohn, Rev. Mod. Phys. **71**, 1253 (1999).
- [5] M. Born and J. R. Oppenheimer, Zur Quantentheorie der Molekeln, Ann. Physik **84**, 457(1927).
- [6] C. Kittel, Introduction to Solid State Physics, Wiley, New York, (1996).
- [7] G. Kresse and J. Hafner, Phys. Rev. B **47**, 558 (1993).
- [8] G. Kresse and J. Hafner, Phys. Rev. B **49**, 14251 (1994).
- [9] G. Kresse and J. Furthmüller, Phys. Rev. B **54**, 11169 (1996).
- [10] G. Kresse and J. Furthmüller, Comput. Mater. Sci., **6**, 15 (1996).
- [11] P. Hohenberg and W. Kohn, Phys. Rev. **136** 3B (1964).
- [12] W. Koch and M. C. Holthausen. A Chemist's Guide to Density Functional Theory. Wiley-VCH, (2001).
- [13] W. Kohn and L. J. Sham, Phys. Rev. **140**, A1133 (1965).
- [14] P. A. M. Dirac, Proc. Cambridge Phil. Roy. Soc. **26**, 376 (1930).
- [15] M. Gell-Mann and K. A. Brueckner, Phys. Rev. **106**, 364 (1957).
- [16] W. J. Carr and A. A. Maradudin, Phys. Rev. **133**, A371 (1964).
- [17] E. Wigner, Phys. Rev. **46**, 1002 (1934).

-
- [18] J. P. Perdew, Phys. Rev. Lett. **55**, 2370 (1985).
- [19] J. P. Perdew and Y. Wang, Phys. Rev. B **45**, 13244 (1992).
- [20] A. D. Becke, Phys. Rev. A **38**, 3098 (1988).
- [21] C. Lee, W. Yang, R. G. Parr, Phys. Rev. B **37**, 785 (1988)
- [22] A. D. Becke, J. Chem. Phys. **96** 2155 (1992).
- [23] J. P. Perdew, K. Burke, and M. Ernzerhof, Phys. Rev. Lett. **77**, 3865 (1996).
- [24] J. Heyd, G. E. Scuseria, and M. Ernzerhof, J. Chem. Phys. **118**, 8207 (2003).
- [25] F. Blöch, Z. Physik **52**, 555 (1928).
- [26] D. S. Sholl and J. A. Steckel, Density Functional Theory : A Practical Introduction (Wiley-Interscience) (2009).
- [27] J. A. Alonso, M. J. Martinez-Lope, M. T. Casais, J. L. Garcia-Munoz, and M. T. Fernandez-Diaz, Phys. Rev. B **61**, 1756 (2000).
- [28] D. Vanderbilt, Phys. Rev. B. **41**, 8412 (1990).
- [29] P.E. Blöchl, Phys. Rev. B **50**, 17953 (1994).
- [30] G. Kresse, and J. Joubert, Phys. Rev. B **59**, 1758 (1999).
- [31] O. K. Andersen and R. V. Kasowski, Phys. Rev. B **4**, 1064 (1971).
- [32] O. K. Andersen, 1971, Computational Methods in Band Theory, p. 178, edited by P. M. Marcus, J. F. Janak and A. R. Williams (Plenum Press).
- [33] S. Grimme, Journal of Computational Chemistry, **27** 15 1787-1799, (2006).
- [34] S. Grimme, Journal of Computational Chemistry **25** 12, 1463-1473, (2004).
- [35] J. C. Slater and G. F. Koster, Phys. Rev. **94** 6 1498-1524 (1954).

Chapter 3

Effect Of Spin Orbit Coupling On Electronic Structure Of Transition Metal Dichalcogenides

3.1 Introduction

In recent years the isolation of graphene [1,2] has resulted in an avalanche of research in two dimensional materials because of their potential application in electronic devices [3,4]. However, the absence of a bandgap has shifted the focus onto other materials like transition metal dichalcogenides [5–8]. These are materials with a direct bandgap at the monolayer limit [9,10]. As the band extrema are at K point of the two dimensional Brillouin zone, there has been a lot of interest in using the valley index for low energy carriers [11,12]. The large separation in momentum space of the degenerate valleys is expected to protect the index against scattering. Additionally, the large spin-orbit interactions associated with the transition metal atom brings about a large spin splitting of the valence band extremum at K point. This allows a labeling of the levels with additionally the spin index. While spin-orbit interactions bring about a large spin-splitting at the K point, they cannot however bring about magnetic ordering. This would then imply that one has an equivalent but opposite spin-splitting at -K point compared to that found at K point, thereby bringing about a coupling between the spin and valley degrees of freedom in these materials with a lot of interesting consequences [13,14]. We examined the spin splitting of the valence band maximum (VBM) in MoS₂, MoSe₂ and MoTe₂ monolayer

and found that as the size of the anion increases, the spin-splitting increases. We capture and explain this using a tight binding model.

However, as we build the structure layer by layer, using the stacking which is seen in the bulk (2H stacking), one finds that for the bilayers as well as for instances where one has an even number of layers, the structure has inversion symmetry. This leads to a zero spin splitting. Additionally, with an increase in the number of layers, one finds that the valence band maximum shifts away from K to Γ [15]. This arises because the out of plane orbitals contribute at Γ . As each additional layer is added, these orbitals interact with those in the next layer leading to shifts in the position of the highest occupied band at Γ such that it becomes the valence band maximum. However, at the few layers limit one finds that the growth techniques used don't always ensure the bulk type of stacking. Focusing on the bilayers, one finds that in some instances one has situations where the top layer is rotated with respect to the bottom layer [16]. This could then lead to various types of stacking seen locally, and consequently, even for the bilayer, one would have a situation where inversion symmetry is broken. The immediate question that followed was whether the slightest rotation of the top layer with respect to the bottom layer would allow us to explore spin valley physics in bilayers, with the zero spin splitting case corresponding to just one point of rotation.

Bilayers of MoSe₂ with those rotation angles which lead to smaller unit cells, were studied. The valence band maximum of these rotated bilayers was found to be at K of the supercell denoted as (\bar{K}) . Contrary to what was speculated earlier, the spin splitting of the VBM did not emerge for the slightest angle of rotation from the configuration where we had inversion symmetry. It was observed that for certain angles of rotation, which were otherwise arbitrary, there is a net spin-splitting of the VBM at \bar{K} whereas for other angles this net spin-splitting vanishes. Our results suggest that there is an alternate mechanism at work which can lead to a vanishing spin splitting at arbitrary angles of rotation. This is operational even when there is no inversion symmetry in the lattice, indicating a distinct origin. Additionally we find that for every angle of rotation θ that we find a spin splitting, there is no spin splitting for $60 - \theta$. As the choice of rotation angles was arbitrary, this relation emerges from the hexagonal symmetry of the lattice.

3.2 Methodology

The bandstructure was calculated within a projector augmented-wave method implementation of density function theory (DFT) within the Vienna Ab-initio Simulation Package (VASP) [25, 26]. The experimental crystal structure of MoS₂, MoSe₂ and MoTe₂ were

taken, with the lattice constant of 3.160 Å [19] 3.289 Å [20] and 3.519 Å [21] respectively additionally, in each of the layered structures a vacuum of 20 Å was added to minimize the interaction between images in the periodic supercell imposed by the method we use. The lattice parameters were kept fixed at the experimental values while the internal positions were optimized in each case. In bilayer MoSe₂, in addition to the optimization of internal positions, we included the optimization of the interlayer separation. This was done including van der Waals interactions implemented using the DFT-D2 method of Grimme [22,23]. The electronic structure was solved self consistently using a k-point mesh of 12x12x1 [24,25]. Twisted bilayers were generated such that the top layer is rotated counterclockwise with respect to the bottom layer. We started by taking the primitive cell for both the unrotated and rotated layers for a particular angle of rotation. We then found all the translation vectors in both cases and found the set of lattice vectors where the supercell of the rotated layer coincides with that for the unrotated layer. Only those twist angles were considered which had reasonable sized commensurate supercells. For the supercells, we appropriately scaled the k-mesh so that the same density of points was sampled in each case. Perdew Burke-Ernzerhof potentials were used for the exchange correlation functional [28,29]. We have extracted the spectral weight of primitive cell K point contributing to the supercell VBM [28]. This was done as follows

Invoking Bloch's theorem, the supercell eigenvector for the k-point \mathbf{K} and band number m , $|\mathbf{K}m\rangle$ can be written as

$$|\mathbf{K}m\rangle = u_{\mathbf{K}m}(r)e^{i\mathbf{K}r} \quad (3.1)$$

Here $u_{\mathbf{K}m}$ is the periodic part of the wavefunction. This can be expanded in terms of its Fourier coefficients as

$$|\mathbf{K}m\rangle = \left[\sum_{\mathbf{G}} \mathbf{C}_{\mathbf{K}m}(\mathbf{G}) e^{i\mathbf{G}r} \right] e^{i\mathbf{K}r} \quad (3.2)$$

We use the open source software WaveTrans to extract these expansion coefficients [29]. The primitive cell k-point \mathbf{k} and band number n has a contribution at $|\mathbf{K}m\rangle$ which is given as

$$\langle \mathbf{k}n | \mathbf{K}m \rangle^2 = |\mathbf{C}_{\mathbf{K}m}(\mathbf{g} + \mathbf{k} - \mathbf{K})|^2 \quad (3.3)$$

where only those coefficients given by the relation $\mathbf{G} = \mathbf{g} + \mathbf{k} - \mathbf{K}$ contribute. Here \mathbf{g} are the reciprocal lattice vectors of the primitive cells.

This method was first tested on a simple system GaAs. For this as the primitive cell we took conventional fcc GaAs unit cell and calculated the bandstructure along Γ to X direction. This is shown in Figure 3.1a. We then created a supercell of GaAs $2 \times 1 \times 1$ and calculated its bandstructure along the primitive cell Γ to X direction, which is shown in Figure 3.1b. The unfolded bandstructure using the method described above with the thickness of the bands proportional to the spectral weight from the respective primitive cell k-point is shown in Figure 3.1c.

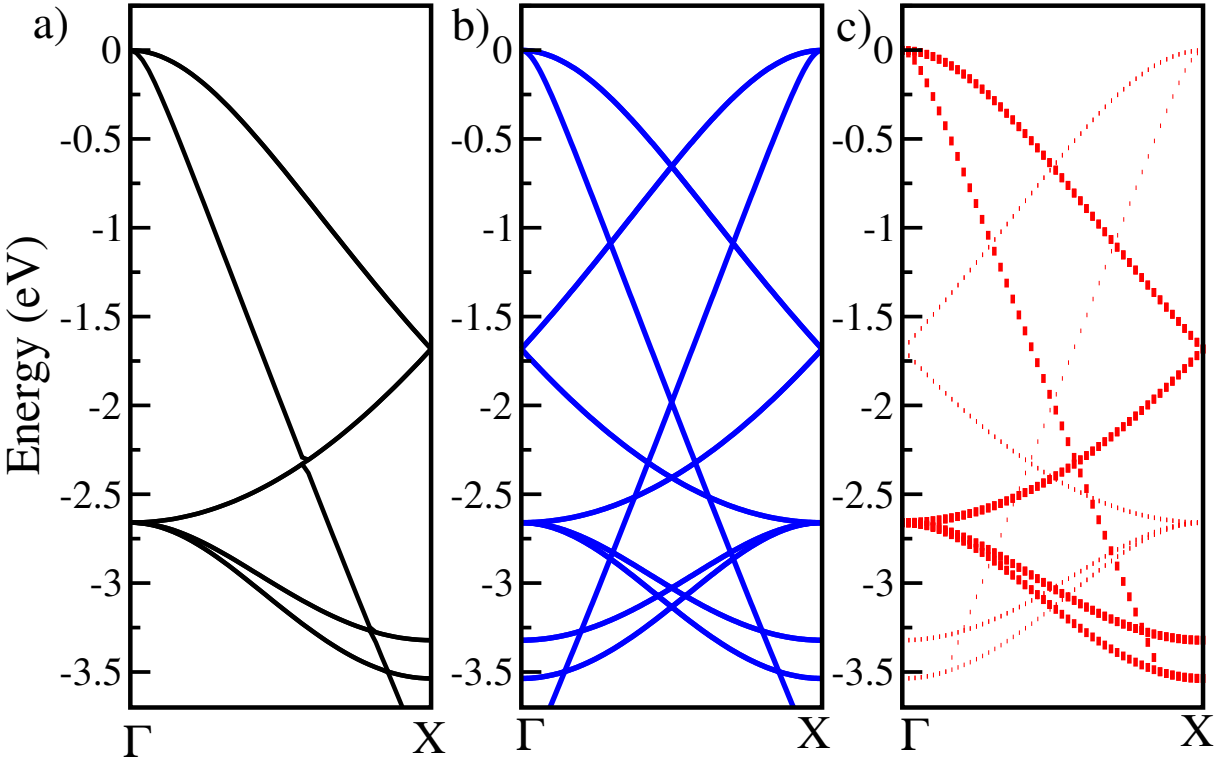


Figure 3.1: a) Ab-initio bandstructure along the Γ to X direction for GaAs conventional cell. b) The supercell bandstructure along Γ to X direction c) The unfolded bandstructure of the $2 \times 1 \times 1$ supercell of GaAs along Γ to X direction with the spectral weights proportional to band thickness

For further analysis, a tight binding model with Mo s, p, d and S/Se/Te s, p, d states was set up. The tight binding parameters were determined by least square error minimization of the ab-initio bandstructure within the tight binding model. The spin-orbit interaction was incorporated as $H_{SO} = \lambda \vec{L} \cdot \vec{S}$, where λ is the spin-orbit coupling constant, \vec{L} is the orbital angular momentum and \vec{S} is the spin angular momentum. Spin-Orbit constant

Compound	Spin-splitting of VBM (meV)
MoS ₂	147
MoSe ₂	187
MoTe ₂	214

Table 3.1: The magnitude of the spin-splitting of VBM at K for MoS₂, MoSe₂ and MoTe₂ monolayer.

(λ) for Mo, S, Se and Te were taken to be 0.119, 0.045, 0.214 and 0.472 respectively as obtained from atomic hartree-fock calculations.

3.3 Results and discussion

Monolayer MoSe₂ consists of a layer of Mo atoms sandwiched between two layers of Se atoms. In its bulk form the stacking found in MoSe₂, is referred to as 2H stacking. In this kind of stacking, the Mo atoms in one layer lie above the Se atoms in the layer beneath. However the MoSe₂ motif in each layer is rotated by an angle of 60° with respect to the adjacent layers above and below it. These layers in the optimized structure are found to be at a distance of 3.21 Å, while the in-plane bondlengths are 2.53 Å. This leads to the nature of the bonding between layers being discussed as arising from van der Waals interactions while that within the layer arise from covalent interactions. Monolayer MoSe₂ is a direct bandgap material, with the valence band maximum (VBM) and the conduction band minimum (CBM) both at the K point of the Brillouin zone. The highest occupied band at Γ , however, is 0.24 eV below. On analyzing the character of the valence band at these high symmetry points, one finds that the VBM at K is contributed by Mo d_{xy} and $d_{x^2-y^2}$ orbitals, where $m_l = \pm 2$. However, the highest occupied band at Γ is mainly contributed by Mo d_{z^2} orbitals, where $m_l = 0$. As a result, on introduction of spin-orbit interactions, which has the form $\lambda \vec{L} \cdot \vec{S}$, the VBM at K-point gets perturbed and splits into two bands with opposite spin whereas the highest occupied band at Γ remains unaffected and hence has no spin-splitting. The spin-splitting of the VBM at K-point is 187 meV (Figure 3.2).

At this point we examined the spin-splitting of VBM in other members of transition metal dichalcogenides MoS₂ and MoTe₂. The results are given in Table 3.1. It can be noticed that as the size of the anion increases in these materials, the spin splitting increases as well.

We wanted to understand the reason for increasing the spin-splitting of VBM as the size of the anion increases. In order to so do we went to a tight binding model with Mo s , p , d and

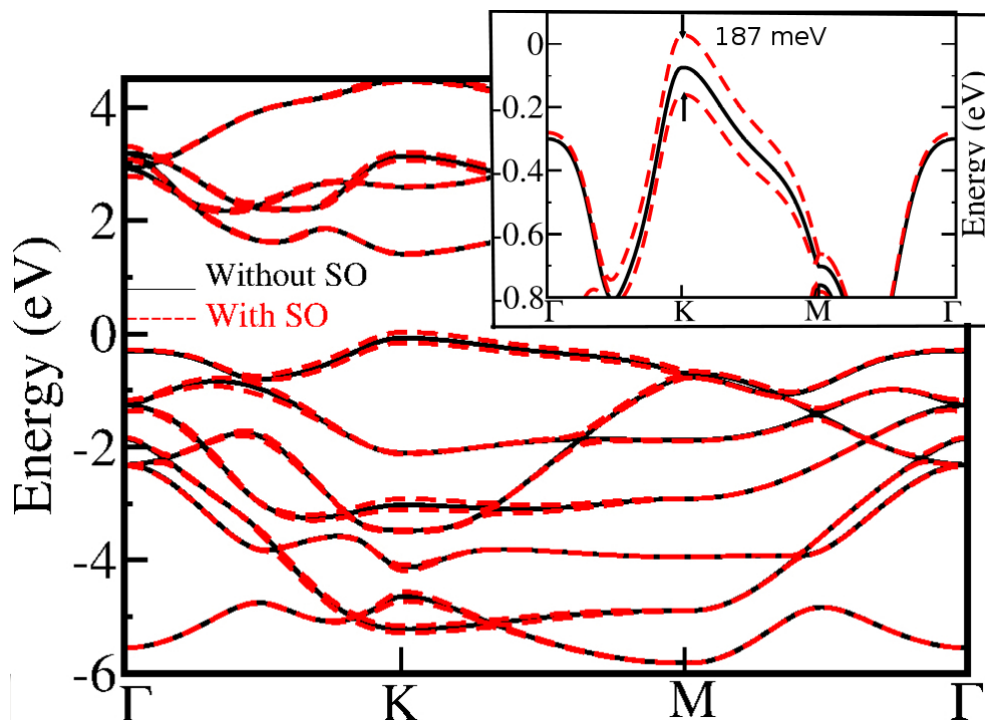


Figure 3.2: Ab-initio bandstructure of monolayer MoSe₂ calculated along various symmetry directions with (dashed red line) and without (solid black line) spin-orbit interactions. The inset shows an expanded view with the magnitude of the spin splitting indicated.

S/Se/Te s, p, d as the basis states. The tight binding parameters were then determined by least square error minimization of the ab-initio bandstructure within this tight binding model for MoS₂, MoSe₂ and MoTe₂. Figures 3.3, 3.4 and 3.5 shows a comparison of the ab-initio bandstructure and the tight binding bandstructure for monolayer of MoS₂, MoSe₂ and MoTe₂ respectively. The tight binding parameters obtained from the fit are listed in Tables 3.2 3.3 and 3.4 for MoS₂, MoSe₂ and MoTe₂ respectively.

We then went on to examine the character of the VBM at K point in each of these compounds within our model. We find that the K point in each of these compounds are hybridized and are composed of Mo d_{xy} and $d_{x^2-y^2}$ orbitals and the anion p_x and p_y orbitals. So we incorporated spin-orbit interactions for d orbitals of Mo as well as p orbitals of the anion. This model of ours was able to capture the spin splitting of these materials. Figures 3.6, 3.7 and 3.8 shows the bandstructure obtained using our tight binding model with spin-orbit coupling incorporated along various symmetry directions for MoS₂, MoSe₂ and MoTe₂ respectively. The values for spin-splitting of the VBM obtained using this model have been summarized in Table 3.5 where the magnitude of spin-splitting is given in meV for MoS₂, MoSe₂ and MoTe₂ along with the respective values obtained from ab-initio calculation.

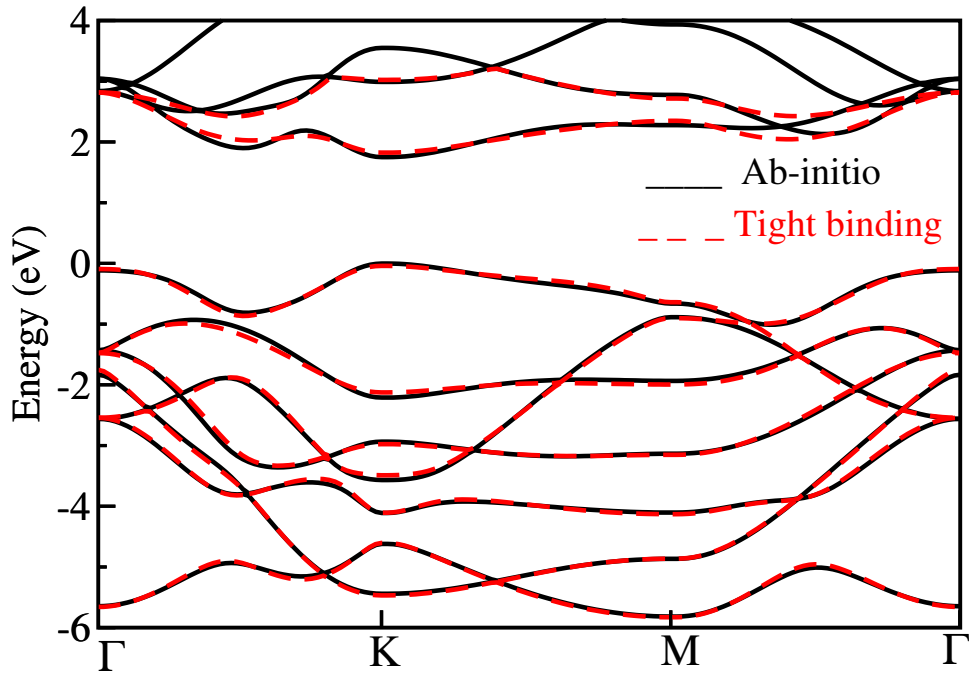


Figure 3.3: Comparison of ab-initio band dispersions (solid black line) for monolayer MoS_2 and the fitted tight binding bands (red dashed line), using a basis consisting of Mo s , p , d and S s , p , d states, calculated along various symmetry directions.

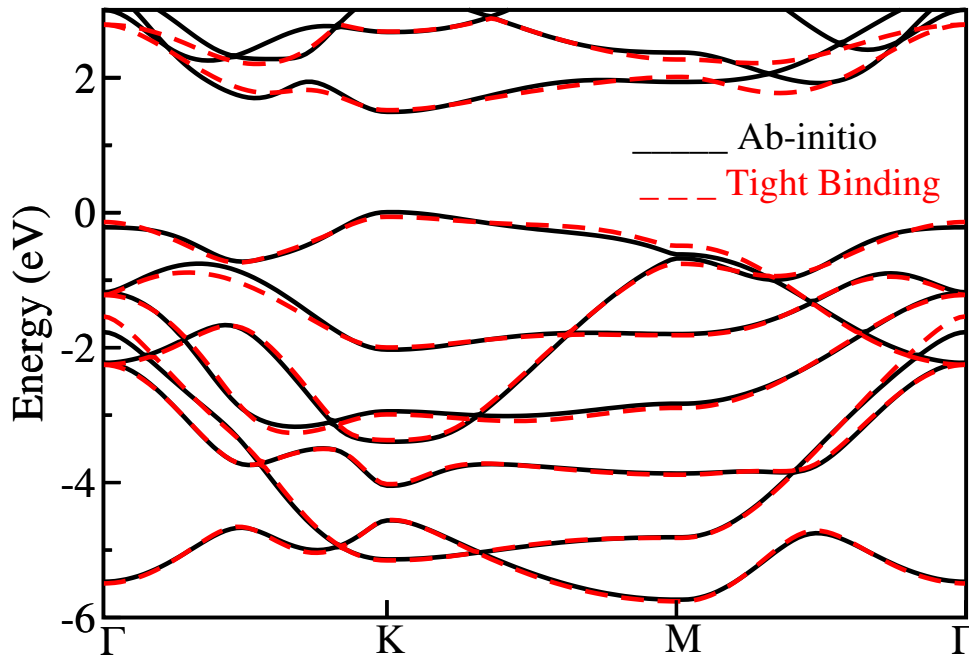


Figure 3.4: Comparison of ab-initio band dispersions (solid black line) for monolayer MoSe_2 and the fitted tight binding bands (red dashed line), using a basis consisting of Mo s , p , d and Se s , p , d states, calculated along various symmetry directions.

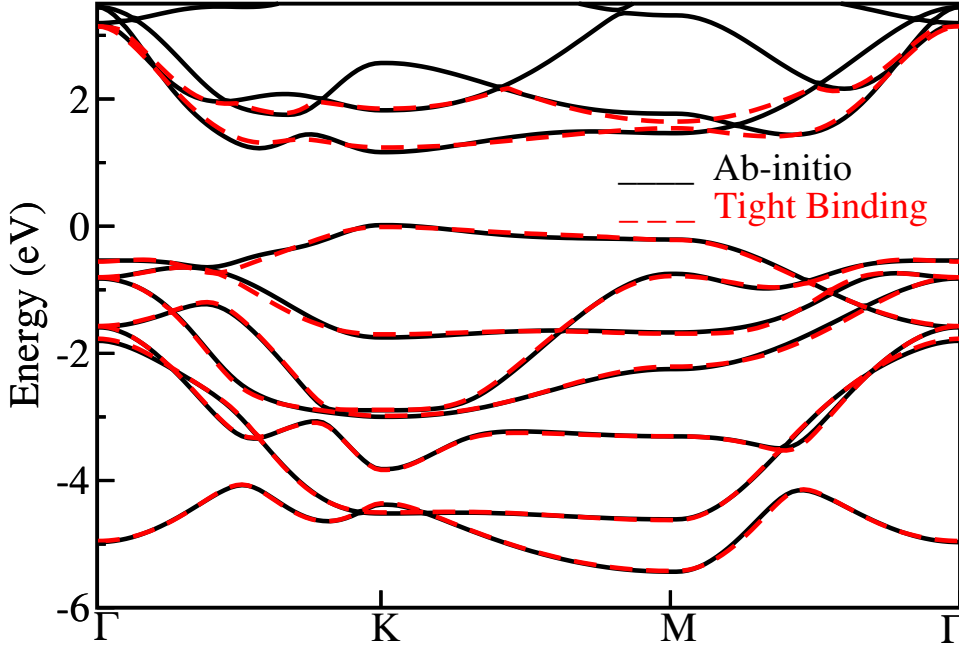


Figure 3.5: Comparison of ab-initio band dispersions (solid blk line) for monolayer MoTe_2 and the fitted tight binding bands (red dashed line), using a basis consisting of Mo s , p , d and Te s , p , d states, calculated along various symmetry directions.

	E_s	E_{p_x}	E_{p_y}	E_{p_z}	$E_{d_{xy}}$	$E_{d_{yz}}$	$E_{d_{zx}}$	$E_{x^2-y^2}$	E_{z^2}
Mo	4.41	12.13	12.13	12.13	1.46	1.46	1.70	1.70	1.01
S	-7.63	-1.15	-1.15	-1.79	11.82	11.82	11.82	11.82	11.82
	$E(\text{Mo}, \text{Mo})$	$E(\text{Mo}, \text{Se})$	$E(\text{Se}, \text{Se})$						
$ss\sigma$	-0.94	-0.83	-0.01						
$sp\sigma$	0.48	1.23	0.29						
$sd\sigma$	-0.59	-0.36	-0.28						
$pp\sigma$	0.00	1.12	0.86						
$pp\pi$	0.00	-0.68	-0.13						
$pd\sigma$	-1.41	-1.01	-0.24						
$pd\pi$	0.01	3.12	0.32						
$dd\sigma$	-0.62	-2.36	0.00						
$dd\pi$	0.10	1.11	1.30						
$dd\delta$	-0.00	-0.38	-0.47						
$ps\sigma$	-0.48	-3.13	-0.29						
$ds\sigma$	-0.59	-2.25	-0.28						
$dp\sigma$	1.41	2.30	0.24						
$dp\pi$	-0.01	-0.78	-0.32						

Table 3.2: Parameters obtained from least-squared-error minimization fitting of the ab-initio band structure onto a tight binding model using s , p , d orbitals of Mo and S for monolayer MoS_2

	E_s	E_{p_x}	E_{p_y}	E_{p_z}	$E_{d_{xy}}$	$E_{d_{yz}}$	$E_{d_{zx}}$	$E_{x^2-y^2}$	E_{z^2}
<i>Mo</i>	4.35	12.32	12.32	12.32	1.48	1.92	1.92	1.48	1.06
<i>Se</i>	-7.42	-0.99	-0.99	-1.67	11.67	11.67	11.67	11.67	11.67
	$E(Mo, Mo)$	$E(Mo, Se)$	$E(Se, Se)$						
<i>ss</i>	-0.70	-0.70	-0.07						
<i>sp</i>	0.42	1.29	0.29						
<i>sd</i>	-0.33	-0.01	-0.20						
<i>pp</i>	0.21	1.06	0.92						
<i>pp</i>	-0.38	-0.62	-0.13						
<i>pd</i>	-0.99	-1.76	-0.23						
<i>pd</i>	0.01	3.37	0.40						
<i>dd</i>	-0.44	-2.53	0.00						
<i>dd</i>	0.07	1.23	1.14						
<i>dd</i>	0.00	-0.36	-0.76						
<i>ps</i>	-0.42	-3.63	-0.29						
<i>ds</i>	-0.33	-2.09	-0.20						
<i>dp</i>	0.99	2.20	0.23						
<i>dp</i>	-0.01	-0.72	-0.40						

Table 3.3: Parameters obtained from least-squared-error minimization fitting of the ab-initio band structure onto a tight binding model using s , p , d orbitals of Mo and Se for monolayer MoSe₂

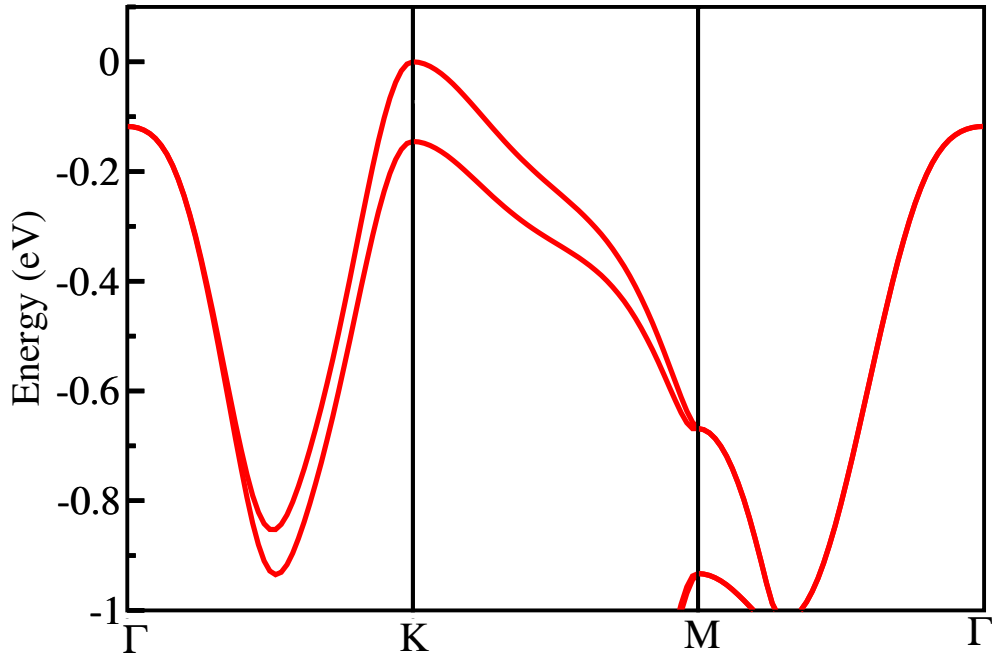


Figure 3.6: The bandstructure of MoS₂ monolayer using tight-binding model with spin-orbit coupling included, calculated along various symmetry directions.

	E_s	E_{p_x}	E_{p_y}	E_{p_z}	$E_{d_{xy}}$	$E_{d_{yz}}$	$E_{d_{zx}}$	$E_{x^2-y^2}$	E_{z^2}
<i>Mo</i>	5.70	13.74	13.74	13.74	0.98	2.26	2.26	0.98	0.87
<i>Te</i>	-10.65	-0.55	-0.55	-1.65	11.01	11.01	11.01	11.01	11.01
	$E(Mo, Mo)$	$E(Mo, Se)$	$E(Se, Se)$						
<i>ssσ</i>	-0.55	-0.41	-0.55						
<i>spσ</i>	0.74	1.14	0.49						
<i>sdσ</i>	-0.12	-0.01	-0.27						
<i>ppσ</i>	0.00	1.31	0.82						
<i>ppπ</i>	0.00	-0.35	-0.09						
<i>pdσ</i>	-0.61	-1.41	-0.16						
<i>pdπ</i>	0.01	2.85	0.44						
<i>ddσ</i>	-0.35	-2.91	-0.00						
<i>ddπ</i>	0.013	1.16	0.30						
<i>ddδ</i>	-0.05	-0.49	-3.04						
<i>psσ</i>	-0.74	-5.00	-0.49						
<i>dsσ</i>	-0.12	-2.60	-0.27						
<i>dpσ</i>	0.61	1.92	0.16						
<i>dpπ</i>	-0.01	-0.60	-0.44						

Table 3.4: Parameters obtained from least-squared-error minimization fitting of the ab-initio band structure onto a tight binding model using s , p , d orbitals of Mo and Te for monolayer MoTe₂

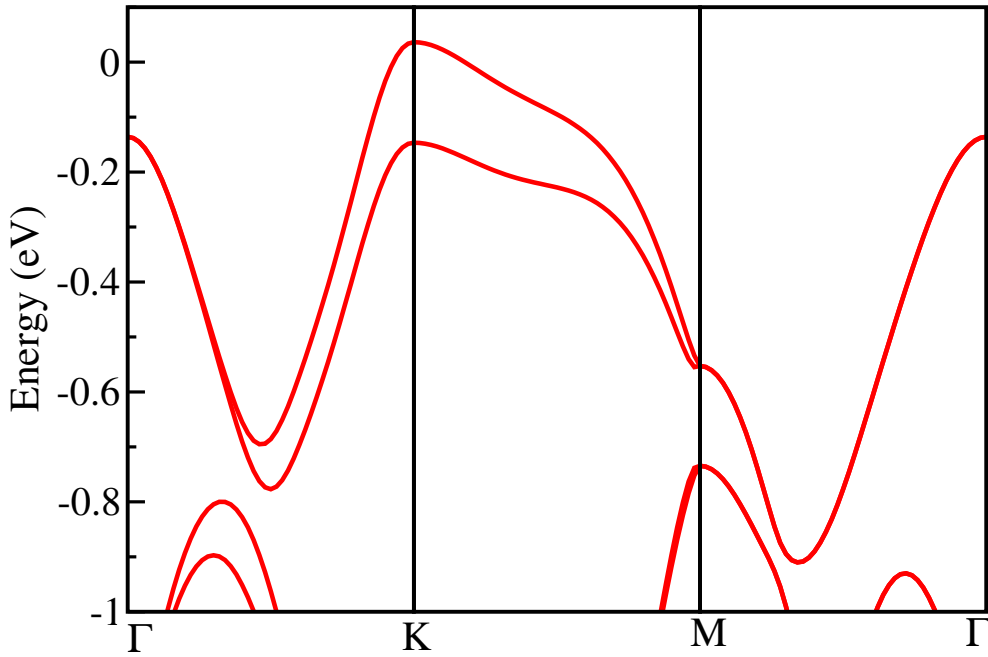


Figure 3.7: The bandstructure of MoSe₂ monolayer using tight-binding model with spin-orbit coupling included, calculated along various symmetry directions.

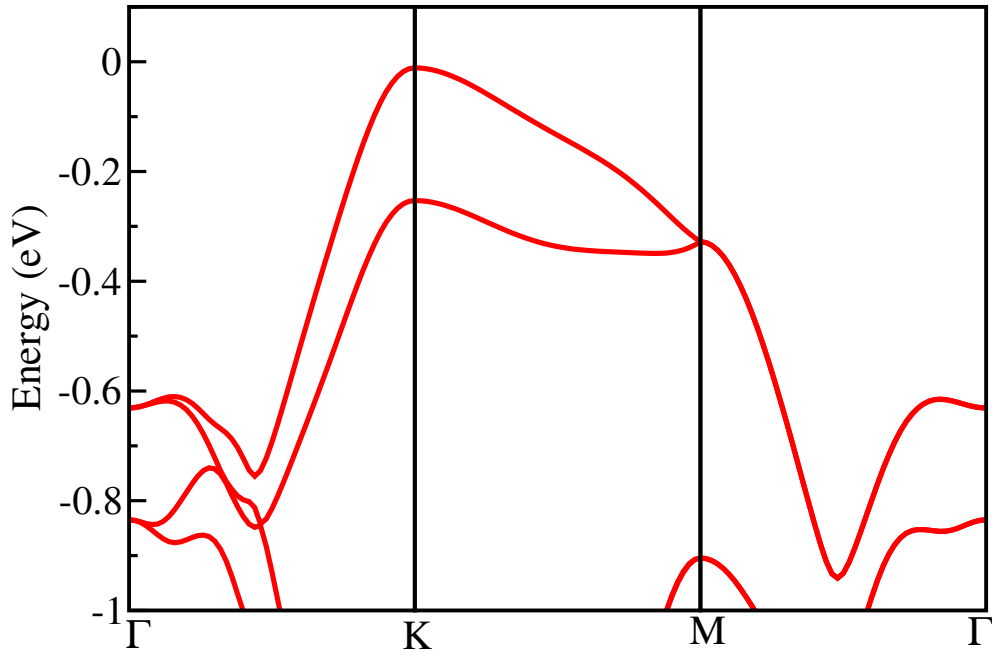


Figure 3.8: The bandstructure of MoTe₂ monolayer using tight-binding model with spin-orbit coupling included, calculated along various symmetry directions.

Compound	Spin-splitting of VBM (meV) (Ab-initio)	Spin-splitting of VBM (meV) (TB)
MoS ₂	147	145
MoSe ₂	187	183
MoTe ₂	214	241

Table 3.5: Comparison of the spin-splitting of VBM for MoS₂, MoSe₂ and MoTe₂ using ab-initio and tight-binding model.

As we go to the bilayer, considering the bulk stacking (2H) of the layers, the valence band maximum, which was at K point in the monolayer moves to Γ point. The conduction band minimum which was also at K point is now at T point, which is a non high symmetry point in the Γ to K direction as shown in Figure 3.9 for MoSe₂. This shifting of VBM and CBM on introduction of another layer can be understood by looking at the character of the bands at these points. As mentioned earlier, the VBM and CBM at K point in the monolayer are contributed by Mo d_{xy} and $d_{x^2-y^2}$ orbitals. These are in-plane orbitals and hence are weakly affected by the introduction of another layer above it. The VBM at Γ and CBM at T are however contributed by the out of plane Mo d_{z^2} orbitals. These orbitals interact with those on the atoms in the layer above and hence are perturbed by the presence of the next layer. Thus this of direct bandgap in monolayer to an indirect bandgap in multilayers can be attributed to interlayer interactions. Interlayer interactions in the bilayers also lead to a splitting of the VBM, at Γ (Δ) of 0.64 eV and at the K point of 0.09 eV. Unlike the monolayer structure, the 2H bilayer structure has a point of inversion symmetry. As a result when we introduce spin-orbit interactions, we find that there is no effective spin-splitting of the highest occupied band at K point. However, on closer examination we find that the highest occupied band at K point has contributions from the up spin states belonging to the Mo atom from the upper layer as well as down spin states belonging to the Mo atom from the lower layer. Its spin-split counterpart which is the second highest occupied band at K has contributions from the down spin states of the Mo atom of the top layer and up spin states of the Mo atom from the lower layer. This has been shown in Figure 3.9.

Alternately, one can project the wavefunction associated with the highest occupied band at K on to each layer and we find a spin polarization associated with each layer. In order to preserve inversion symmetry, the splitting in one layer is opposite to that in the other, resulting in a net zero spin splitting. So the question we asked was, whether the slightest deviation from a structure with an inversion symmetry point would restore spin splitting in the bilayers? In order to investigate this, we considered various angles of rotation so that we had small unit cells for which DFT calculations could be performed easily. Starting from the unrotated structure, where Mo and Se atoms in the top layer sit on top of the Mo and Se atoms in the layer beneath and the angle of rotation is 0° (denoted as AA), we considered 18 different angles, upto a rotation of 60° (denoted as AB) as angles beyond this can be mapped back to this range. The choice of angle was determined by our computational resources. This constrained us to consider only those angles where we got reasonable sized supercells. The angles considered by us and the number of atoms in the respective supercells are given in Table 3.6. Structure of one of the twisted bilayers with angle of rotation 38.2° is shown in Figure 3.10.

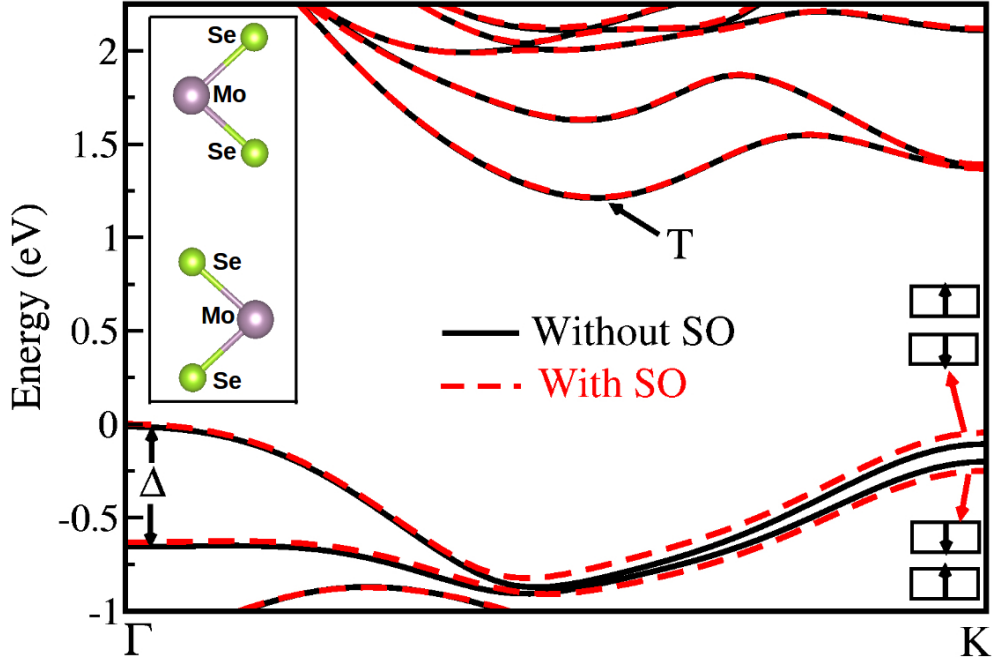


Figure 3.9: The ab-initio bandstructure with (dashed red line) and without (solid black line) spin-orbit interactions along Γ to K direction for 2H stacking MoSe₂ (structure shown schematically). The contributions from Mo atoms of each layer for the two highest occupied bands at K point after inclusion of spin-orbit interactions is also given.

Angle (θ)	Angle ($60 - \theta$)	No. of Atoms
0(AA)	60(AB)	6
10.40	49.60	546
14.10	45.90	1194
15.18	44.82	258
17.90	42.10	186
27.80	32.20	78
34.00	26.00	474
38.20	21.80	42
46.80	13.20	114

Table 3.6: The angle of rotation and the corresponding number of atoms in the supercell for different twisted MoSe₂ bilayers.

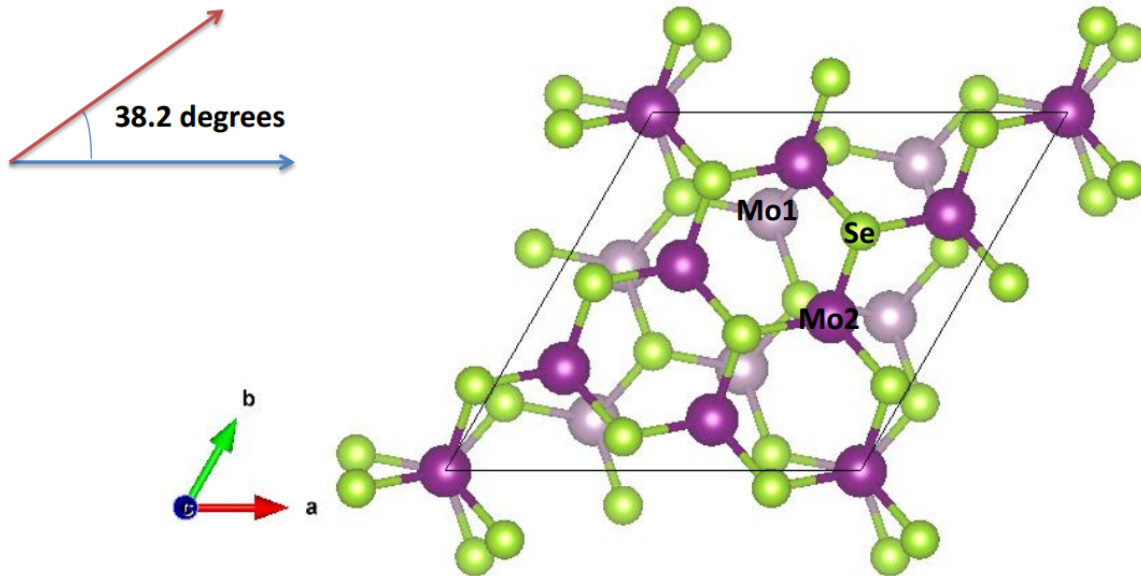


Figure 3.10: Structure of one of the twisted bilayers with angle of rotation 38.2° . Mo1 is the from the bottom layer whereas Mo2 represents Mo from the top layer.

We then went on to examine the electronic structure of each of these rotated structures. The calculated bandstructure with spin-orbit interactions included, for one of the rotation angles (38.2°) is shown in Figure 3.11 along Γ to \bar{K} direction of the supercell. One finds the VBM to be at \bar{K} . A similar result is found for the other twist angles considered by us.

In order to get meaningful information from a supercell bandstructure, we need to unfold it to the primitive cell Brillouin zone and to do so we first used the Brillouin zone of the supercell and found the eigenvalues for all the points which unfolded on to the Γ to K direction of the primitive cell. For simplicity it was done without spin-orbit interactions included. This is shown in Figure 3.12 for 38.2° .

Now we need the spectral weight of the supercell k-point at any primitive cell k-point to determine if it contributes or not. This is shown in Figure 3.13 with the thickness of the bands proportional to their contributions. This analysis establishes that the highest occupied band at \bar{K} has maximum contribution from the primitive cell K point. Although for simplicity we have carried out the analysis presented in Figure 3.12 and 3.13 in the absence of spin-orbit interactions. However only for VBM at \bar{K} point, the analysis has been carried out for the wavefunction obtained after including spin-orbit interactions for all angles. (The implications of this analysis is discussed later). Now, comparison of the bandstructure presented in Figure 3.13 with in the 2H bandstructure, we calculated the 2H bilayer MoSe_2 bandstructure at the interlayer separation equal to that of the twisted

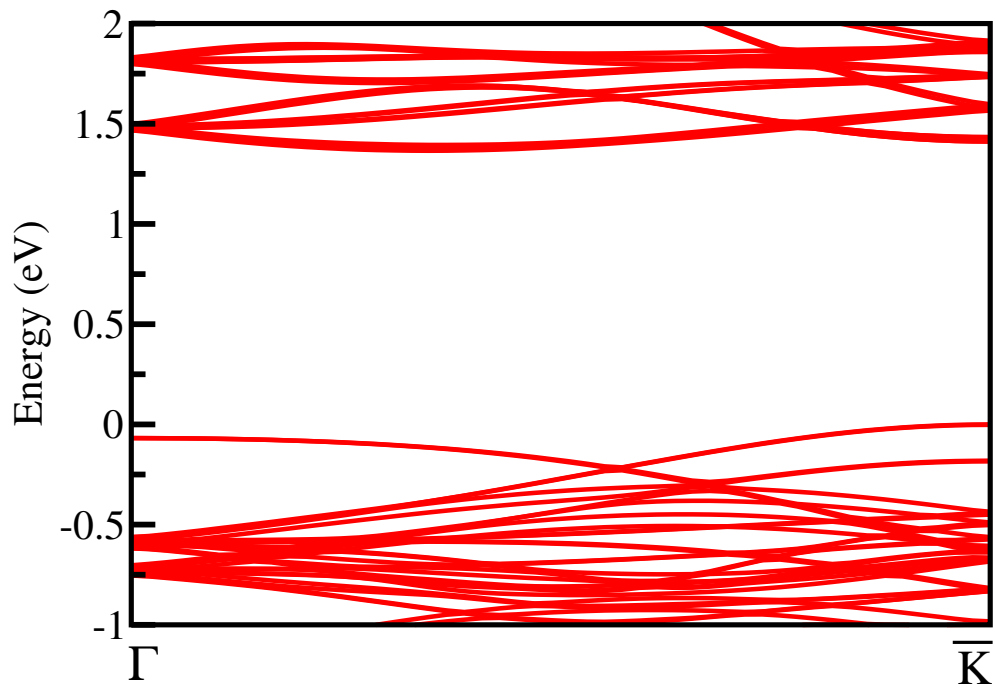


Figure 3.11: Ab-initio bandstructure with spin-orbit interactions included for MoSe₂ bilayer at a twist angle of 38.2° along the Γ to \bar{K} direction.

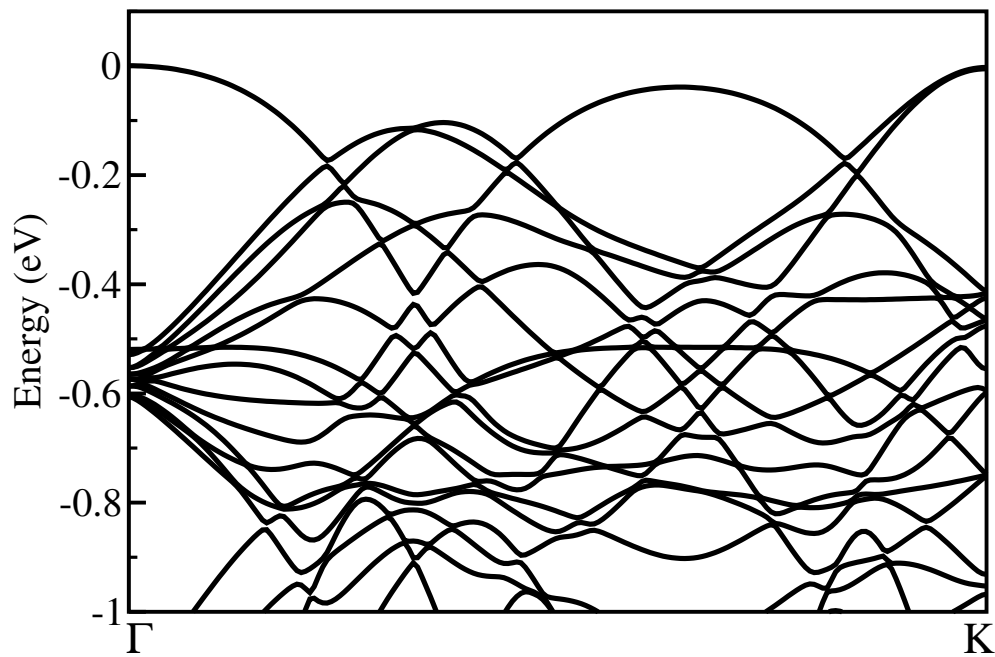


Figure 3.12: The supercell bandstructure without spin-orbit coupling included along Γ to K direction of the primitive cell.

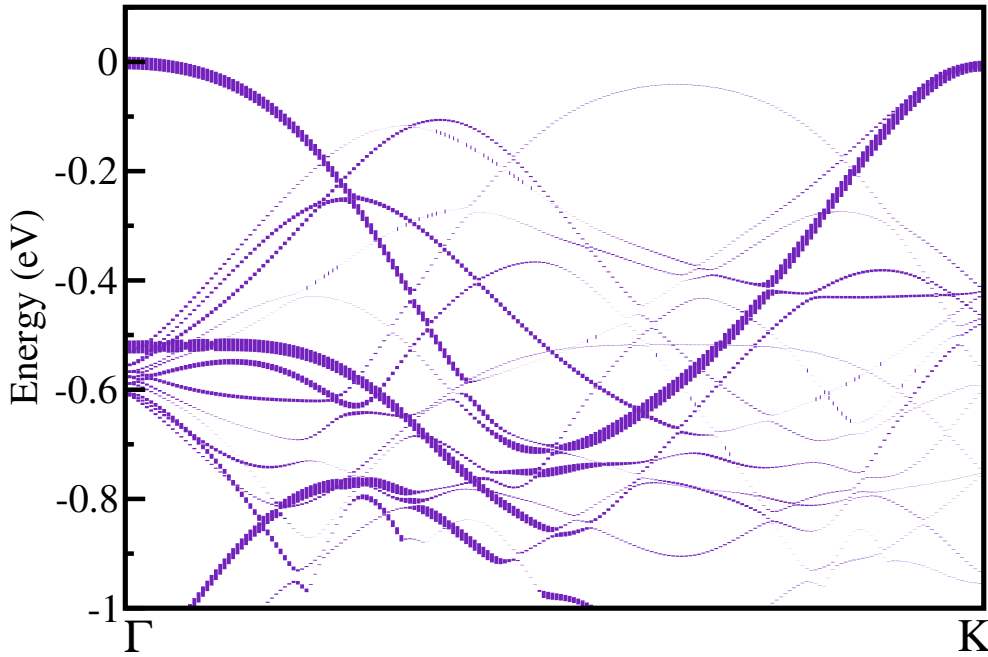


Figure 3.13: The unfolded bandstructure without spin-orbit coupling included along Γ to K direction of the primitive cell with spectral weights proportional to band thickness.

bilayer (3.44 \AA). This bandstructure with (dashed line) and without (solid line) has been shown in Figure 3.14 along various symmetry directions.

From Figure 3.14, we can see that even for the 2H stacking the VBM has shifted from Γ to K . This happens because of the decrease in interlayer interactions as the separation is increased. Comparing the bandstructures for Figures 3.14 and 3.13, we find remarkable similarities. The splitting of the highest occupied band at Γ (Δ) is found to be 0.52 eV in the twisted bilayer. This is related to the interaction between the layers and atleast at this angle it seems similar to what we have for 2H structure (0.50 eV) at the same interlayer separation. A similar analysis has been done for a rotation angle of 15.18° , where Δ was found to be 0.53 eV . This has been shown in Figure 3.15.

As the highest occupied band at \bar{K} has the spin-splitting associated with it, shifting of the VBM to \bar{K} allows us to explore the consequences of the spin valley physics in the bilayers also. To see if this is a general feature for all rotated angles, we studied the electronic structure of all the 18 rotated structures. In each case we had the VBM at \bar{K} . For the unrotated bilayer (rotation angle= 0°), there is no inversion symmetry in the structure. The bands associated with the two monolayers, split in the same direction giving rise to a net splitting of 147 meV [30]. Whereas in the 60° rotated bilayer, where the structure has inversion symmetry similar to that of 2H stacking, bands associated with both the monolayers, split in opposite directions resulting in a net zero spin splitting. The angles

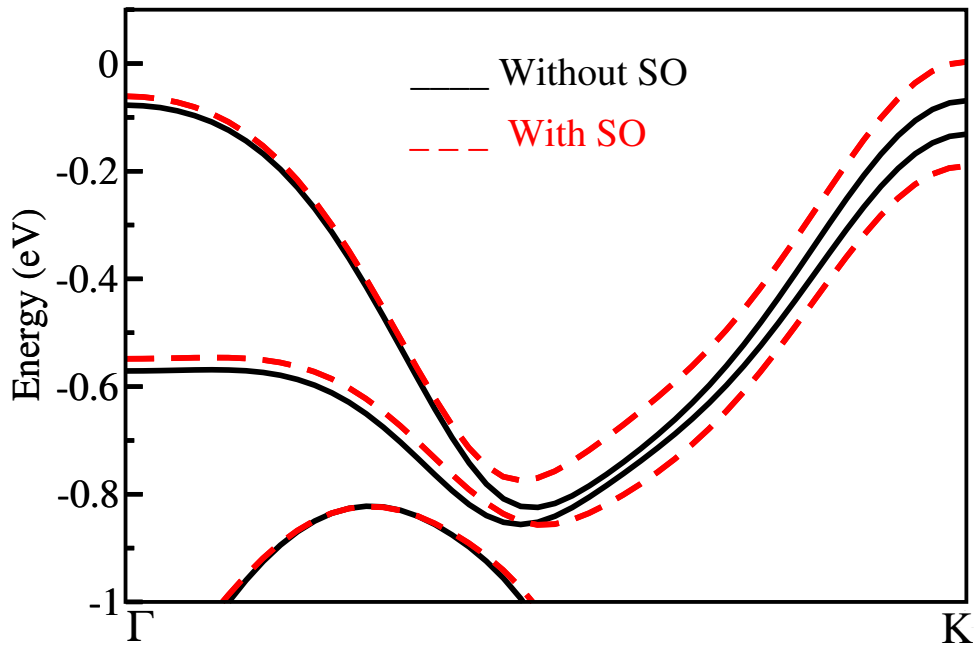


Figure 3.14: The ab-initio bandstructure with (dashed line) and without (solid line) spin-orbit interactions along Γ to K direction for MoSe₂ bilayer with 2H stacking at the interlayer separation equal to that of the twisted bilayers.

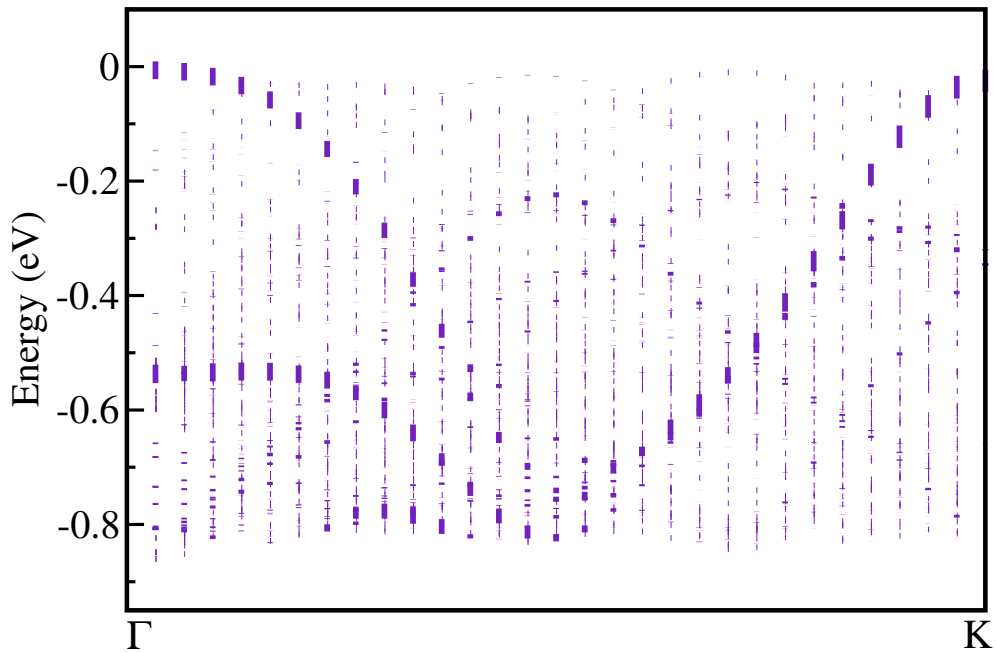


Figure 3.15: The unfolded bandstructure without spin-orbit coupling included along Γ to K direction of the primitive cell for MoSe₂ bilayer at a twist angle of 15.8° with spectral weights proportional to band thickness.

Angle (θ)	Spin-Splitting	Angle ($60-\theta$)	Spin-splitting
0(AA)	147	60(AB)	NO spin-splitting
10.40	183	49.60	NO spin-splitting
14.10	183	45.90	NO spin-splitting
15.18	183	44.82	NO spin-splitting
17.90	183	42.10	NO spin-splitting
27.80	183	32.20	NO spin-splitting
34.00	180	26.00	NO spin-splitting
38.20	179	21.80	NO spin-splitting
46.80	180	13.20	NO spin-splitting

Table 3.7: The angle of rotation and the corresponding spin-splitting of the VBM. The labels for specific choice of angles has also been given.

in between these two extreme cases, however show some interesting trends. The results have been summarized in Table 3.7.

It can be seen that for some angles of rotation (represented as θ in Table 3.7), the VBM has a spin splitting but angles which are $60 - \theta$ do not show a net spin-splitting of the VBM. In order to understand this we went on to examine the primitive cell k-point contributions to the VBM of the supercell. From our analysis we found that the cases where there is a spin-splitting, VBM at \bar{K} is contributed by K point of both the unrotated and rotated primitive cells, whereas the angles where there is no net spin-splitting, the contribution is from K and -K of the unrotated and rotated primitive cells respectively. In order to understand this we tried to examine the simplest case of 0° (θ) and 60° ($60 - \theta$). In case of 0° , the K point from the Brillouin zone of both the layers sit on top of each other whereas when the top layer is rotated by an angle of 60° the -K point from the top layer sits on top of the K point of the bottom layer. This explains the contributions to the highest occupied band at K for the bilayer in these two cases. However, when we go to other angles the case is not that simple as large unit cells are involved.

In order to understand the pattern of spin-splitting in these intermediate angles, we have to understand the structure of these supercell carefully and compare it with both the primitive cell structures (unrotated as well as rotated). We also need to understand the relation between both the primitive cell Brillouin zones and the supercell Brillouin zone. Let \vec{a}_1 and \vec{a}_2 be the unrotated primitive cell lattice vectors also \vec{a}'_1 and \vec{a}'_2 be the rotated primitive cell lattice vectors. Also let \vec{A}_1 and \vec{A}_2 be the supercell lattice vectors. Now let us further assume the unrotated primitive cell reciprocal lattice vectors be \vec{b}_1 and \vec{b}_2 , rotated primitive cell reciprocal lattice vectors be \vec{b}'_1 and \vec{b}'_2 and supercell reciprocal lattice vectors be \vec{B}_1 and \vec{B}_2 respectively. Now if we look at the angles made by each of the primitive cell lattice vectors with the supercell lattice vectors we have by definition $\alpha_{1,1}$,

θ	$\vec{A}_1 - \vec{a}_1$ $\alpha_{1,1}$	$\vec{A}_1 - \vec{a}_1'$ $\alpha_{1,1'}$	$\vec{A}_1 - \vec{a}_2$ $\alpha_{1,2}$	$\vec{A}_1 - \vec{a}_2'$ $\alpha_{1,2'}$	$\vec{A}_2 - \vec{a}_1$ $\alpha_{2,1}$	$\vec{A}_2 - \vec{a}_1'$ $\alpha_{2,1'}$	$\vec{A}_2 - \vec{a}_2$ $\alpha_{2,2}$	$\vec{A}_2 - \vec{a}_2'$ $\alpha_{2,2'}$
10.40	5.21	5.19	114.79	125.19	65.21	54.81	54.79	65.19
14.10	7.05	7.05	112.95	127.05	67.05	52.95	52.95	67.05
15.18	7.59	7.59	112.41	127.59	67.59	52.41	52.41	67.59
17.90	8.95	8.95	111.05	128.95	68.95	51.05	51.05	68.95
27.80	13.90	13.90	106.10	133.90	73.90	46.10	46.10	73.90
34.00	17.00	17.00	103.00	137.00	77.00	43.00	43.00	77.00
38.20	19.11	19.09	40.89	79.09	79.11	40.91	100.89	139.09
46.80	23.41	23.39	96.59	143.39	83.41	36.61	36.59	83.39
60- θ	$\vec{A}_1 - \vec{a}_1$ $\alpha_{1,1}$	$\vec{A}_1 - \vec{a}_1'$ $\alpha_{1,1'}$	$\vec{A}_1 - \vec{a}_2$ $\alpha_{1,2}$	$\vec{A}_1 - \vec{a}_2'$ $\alpha_{1,2'}$	$\vec{A}_2 - \vec{a}_1$ $\alpha_{2,1}$	$\vec{A}_2 - \vec{a}_1'$ $\alpha_{2,1'}$	$\vec{A}_2 - \vec{a}_2$ $\alpha_{2,2}$	$\vec{A}_2 - \vec{a}_2'$ $\alpha_{2,2'}$
49.60	5.21	54.81	125.21	174.81	54.79	5.19	65.21	114.81
45.90	52.95	7.05	67.05	112.95	112.95	67.05	7.05	52.95
44.82	52.41	7.59	67.59	112.41	112.41	67.59	7.59	52.41
42.10	8.95	51.05	128.95	171.05	111.05	68.95	8.95	51.05
32.20	46.10	13.90	73.90	106.10	106.10	73.90	13.90	46.10
26.00	43.00	17.00	77.00	103.00	103.00	77.00	17.00	43.00
21.80	40.89	19.09	79.11	100.91	100.89	79.09	19.11	40.91
13.20	36.59	23.40	83.41	96.60	96.59	83.40	23.41	36.60

Table 3.8: A table showing the angles made by primitive cell unrotated lattice vectors and primitive cell rotated lattice vectors to the supercell lattice vectors.

$\alpha_{1,2}$, $\alpha_{1,1'}$ and $\alpha_{1,2'}$, the angles made by \vec{A}_1 with \vec{a}_1 , \vec{a}_2 , \vec{a}_1' and \vec{a}_2' respectively. Similarly the angles made by \vec{A}_2 with \vec{a}_1 , \vec{a}_2 , \vec{a}_1' and \vec{a}_2' are labeled as $\alpha_{2,1}$, $\alpha_{2,2}$, $\alpha_{2,1'}$ and $\alpha_{2,2'}$. We measured these angles for each of the twisted bilayers and have listed them in Table 3.8. It can further be shown that the reciprocal lattice vectors of both the primitive cells also make the same angles with the supercell reciprocal lattice vectors as their real space counterparts.

Now looking at Table 3.8 we find that, when we consider any supercell lattice vector and look at angles made by the two sets of primitive lattice vectors (one from unrotated and other from the rotated) and find that they both make an angle less than 30° , there is a net spin splitting. These cases have been listed in the upper half of the Table 3.8. Whereas for the cases, where when we consider any supercell lattice vector and see that if one of the primitive cell lattice vector make an angle which is less than 30° but the same lattice

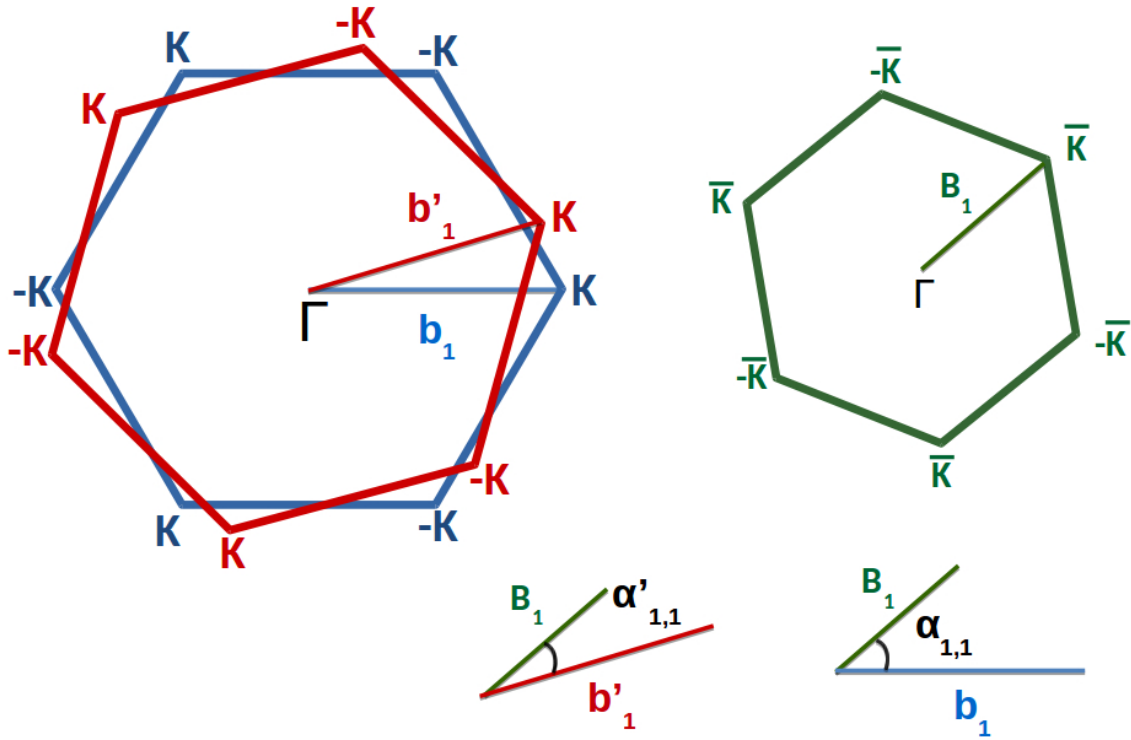


Figure 3.16: Schematic showing the contributions to \bar{K} from the Brillouin zone of the rotated and unrotated primitive cells

vector of the other primitive cell makes an angle between 30° and 60° , there is no spin splitting. These angles have been listed in the lower half of the Table 3.8.

In order to understand why in the cases where both primitive cell reciprocal lattice vectors make an angle $\alpha_{1,1}$ and $\alpha_{1,1}'$ are less than 30° , there is a spin splitting whereas there is no net spin-splitting in the cases where one of these angle is between 0° and 30° whereas the other one is between 30° and 60° , we have to look at the Brillouin zones of both the primitive cells and the supercells. This is shown in Figure 3.16, where the unrotated primitive cell Brillouin zone is shown in blue and the Brillouin zone of the rotated primitive cell is shown in red. The supercell Brillouin zone is shown in green. In this figure we have shown one of the reciprocal lattice vectors in each case and defined the two angles both the unit cells make with the supercell. What we found is that in the first case (First half of the Table 3.8), K point both the primitive cell Brillouin zones contributes to the \bar{K} of the supercell using the extraction method mentioned earlier whereas in the second case (Second half of the Table 3.8), K from one of the primitive cell Brillouin zone and -K from the other primitive cell Brillouin zone contributes at \bar{K} of the supercell Brillouin zone.

The question that followed was what determines which k-point would contribute. To understand this, we borrowed ideas from alloy theory for getting the weight of a primitive

\mathbf{k} point at a supercell one [31]. It is given by

$$P_i(\mathbf{k}) = \sum_{n=1}^{\infty} | \langle \psi_i(\mathbf{r}) | u_{n\mathbf{k}}(\mathbf{r}) e^{i\mathbf{k}\cdot\mathbf{r}} \rangle |^2 \quad (3.4)$$

Here, $\psi_i(\mathbf{r})$ is the eigenfunction of the supercell and $u_{n\mathbf{k}}(\mathbf{r})e^{i\mathbf{k}\cdot\mathbf{r}}$ is the complete set of Bloch functions of band index n , summed over of the projection at a given translationally invariant wave vector \mathbf{k} , which is inside the first Brillouin zone of the constituent monolayers. At the supercell $\bar{\mathbf{K}}$ point, the contribution is from \mathbf{K} or $-\mathbf{K}$ of the primitive cell is determined by Equation 3.4. Since $u_{n\mathbf{k}(\mathbf{r})}$ for both \mathbf{K} and $-\mathbf{K}$ is similar, the contribution is determined by the phase factor $e^{i\mathbf{k}\cdot\mathbf{r}}$ in Eq.(1). The overlap depends on the cosine of the angle between the primitive cell reciprocal lattice vectors and the reciprocal lattice vectors. As a result, whenever both the angles shown in Figure 3.16 are less than 30° both the \mathbf{K} points contributes at $\bar{\mathbf{K}}$ and when one of them is less than 30° but the other one between 30° and 60° \mathbf{K} from one and $-\mathbf{K}$ from the other contributes. Since the splitting due to \mathbf{K} is in opposite direction to that of $-\mathbf{K}$, the net splitting is zero at $\bar{\mathbf{K}}$. This unusual behavior of the spin splitting for rotation angle of θ and $60 - \theta$ can be attributed to the symmetries of the hexagonal Brillouin zone.

3.4 Conclusion

In conclusion, we have explored bilayers of twisted MoSe_2 . We find that for arbitrary angles of rotation θ , one could have a spin splitting at \mathbf{K} point, while the calculated electronic structure of $60 - \theta$ has no spin splitting. The mechanism at work is not the absence of inversion symmetry and can be related to the hexagonal symmetry of the lattice. This clearly demonstrate that the presence of inversion symmetry is not the only mechanism for vanishing spin splitting. Further the hexagonal symmetry of the lattice determines how θ and $60 - \theta$ would behave.

Bibliography

- [1] K. S. Novoselov, A. K. Geim, S. V. Morozov, D. Jiang, Y. Zhang, S. V. Dubonos, I. V. Grigorieva, and A. A. Firsov, *Science* **306**, 666 (2004).
- [2] K. S. Novoselov, A. K. Geim, S. V. Morozov, D. Jiang, M. I. Katsnelson, I. V. Grigorieva, S. V. Dubonos, and A. A. Firsov, *Nature* **438**, 197 (2004).
- [3] Y. Wu, Y. ming Lin, A. A. Bol, K. A. Jenkins, F. Xia, D. B. Farmer, Y. Zhu, and P. Avouris, *Nature* **472**, 74 (2011).
- [4] Y.-M. Lin, K. A. Jenkins, A. Valdes-Garcia, J. P. Small, D. B. Farmer, and P. Avouris, *Nano Lett.* **9**, 422 (2009).
- [5] Q. H. Wang, K. Kalantar-Zadeh, A. Kis, J. N. Coleman, and M. S. Strano, *Nat. Nano.* **7**, 699 (2012)
- [6] S. Balendhran, S. Walia, H. Nili, J. Z. Ou, S. Zhuiykov, R. B. Kaner, S. Sriram, M. Bhaskaran, and K. Kalantar-zadeh, *Adv. Funct. Mater.* **23**, 3952 (2013).
- [7] J. N. Coleman, M. Lotya, A. O'Neill, S. D. Bergin, P. J. King, U. Khan, K. Young, A. Gaucher, S. De, R. J. Smith, I. V. Shvets, S. K. Arora, G. Stanton, H.-Y. Kim, K. Lee, G. T. Kim, G. S. Duesberg, T. Hallam, J. J. Boland, J. J. Wang, J. F. Donegan, J. C. Grunlan, G. Mo-riarty, A. Shmeliov, R. J. Nicholls, J. M. Perkins, E. M. Grievson, K. Theuwissen, D. W. McComb, P. D. Nellist and V. Nicolosi, *Science* **331**, 568 (2011).
- [8] Y. Zhang, J. Ye, Y. Matsushashi, and Y. Iwasa, *Nano Lett.* **12**, 1136 (2012).
- [9] C. Lee, H. Yan, L. E. Brus, T. F. Heinz, J. Hone, and S. Ryu, *ACS Nano* **4**, 2695 (2010)
- [10] S. Lebgue and O. Eriksson, *Phys. Rev. B* **79**, 115409 (2009).

-
- [11] D. Xiao, G.-B. Liu, W. Feng, X. Xu, and W. Yao, *Phys. Rev. Lett.* **108**, 196802 (2012).
- [12] A. Srivastava, M. Sidler, A. V. Allain, D. S. Lembke, A. Kis, and A. Imamolu, *Nat. Phys.* **11**, 141 (2015).
- [13] L. Bawden, S. Cooil, F. Mazzola, J. Riley, L. Collins-McIntyre, V. Sunko, K. W. B. Hunvik, M. Leandersson, C. Polley, T. Balasubramanian, T. Kim, M. Hoesch, J. Wells, G. Balakrishnan, M. Bahramy, and P. King, *Nat. Comm.* **7**, 1 (2016).
- [14] K. F. Mak, K. He, J. Shan, and T. F. Heinz, *Nat. Nanotech.* **7**, 494 (2012).
- [15] R. Das, S. K. Pandey and P. Mahadevan, arXiv:1702.04535v1 (2017).
- [16] A. A. Puretzky, L. Liang, X. Li, K. Xiao, B. G. Sumpter, V. Meunier, and D. B. Geohegan, *ACS Nano* **10**, 2736 (2016).
- [17] G. Kresse and J. Hafner, *Phys. Rev. B* **47**, 558 (1993).
- [18] G. Kresse and J. Hafner, *Phys. Rev. B* **49**, 14251 (1994).
- [19] L. Liu, S. B. Kumar, Y. Ouyang et al., *IEEE Trans. Electron Devices* **58**, 3042 (2011).
- [20] J. He, K. Hummer, and C. Franchini, *Phys. Rev. B* **89**, 075409 (2014).
- [21] J. A. Champion, *Brit. J. Appl. Phys.* **16**, 1035-1037 (1965).
- [22] S. Grimme, *Journal of Computational Chemistry*, **27**, 15, 1787-1799, (2006).
- [23] J. Harl, L. Schimka, and G. Kresse, *Phys. Rev. B* **81**, 118126 (2010).
- [24] P. E. Blochl, *Phys. Rev. B* **50**, 17953 (1994).
- [25] G. Kresse and D. Joubert, *Phys. Rev. B* **59**, 1758 (1999).
- [26] J. P. Perdew, K. Burke, and M. Ernzerhof, *Phys. Rev. Lett.* **77**, 3865 (1996).
- [27] J. P. Perdew, B. Kieron, and E. Matthias, *Phys. Rev. Lett.* **78**, 1396 (1997).
- [28] V. Popescu and A. Zunger, *Phys. Rev. B* **85**, 085201 (2012).
- [29] R. M. Feenstra, N. Srivastava, Q. Gao, B. D. M. Widom, T. Ohta, G. L. Kellogg, J. T. Robinsonand, and I. V. Vlassiuk, *Phys. Rev. B* **87**, 041406 (2013).

-
- [30] In all the angles studied there were, two sets of doubly degenerate VBM, but in the case of 0° rotation (AA stacking), there were four bands, and the splitting mentioned here is the innermost separation between the bands with opposite spin.
- [31] L.-W. Wang, L. Bellaiche, S.-H. Wei, and A. Zunger, Phys. Rev. Lett. **80**, 4725 (1998).

Chapter 4

In Search Of Planar Graphitic Semiconductors

4.1 Motivation

Rapid minimization of devices has been the path followed by the electronic industry over the past several years towards smaller and more efficient devices. However soon the devices are going to enter a size regime where they will cease to be as efficient. Hence there is a need to explore alternate routes to new generation devices. Two dimensional materials have been intensively studied in this regard as they belong to the ultimate lengthscale of minimization [1–7]. There has been an upsurge in realizing more and more two dimensional materials, with useful electronic structure. Apart from layered materials like transition metal dichalcogenides [8–11], which were discussed in the previous chapters, there has been a lot of interest in obtaining two dimensional graphitic form of semiconductors and heavy metals [12–15]. As mentioned in the previous work, the hexagonal lattice of two dimensional materials play an important role in its electronic structure. In this chapter we examine the structural properties of free standing II-VI and III-V semiconductors at the monolayer limit in the first part. Our results showed that while those formed by elements belonging to the first row of the periodic table formed graphitic structures, those involving non first row elements required strain to stabilize them. In the second part of the chapter we explore how one could use a substrate to provide the strain and extend predictions made for free standing films to those on a substrate.

4.2 Structural Distortions in Monolayers Of Binary Semiconductors

4.2.1 Introduction

The field of layered semiconductors have been rejuvenated recently with the isolation of graphene. There has been an upsurge in research towards finding and isolating more and more layered materials. Binary semiconductors like ZnO have been investigated for the possibility of having a stable two dimensional structure [16]. These ionic semiconductors favor the wurtzite structure in bulk. When films of these materials are grown without any bias for the growth direction, the polar c-direction was found to be favored. This was a surprise as one would associate a higher energy with a polar surface, as it has no dipole moment associated with it. On closer analysis, a graphitic phase was found to be formed [17], which solves the problem associated with the polar surface [18]. In a graphitic phase one has a reduced coordination of atoms compared to the otherwise observed wurtzite phase. The system compensates for the lost coordination by decreasing the cation-anion bondlengths.

The natural question that followed was what happens to the compounds formed by elements beyond the first row at a few monolayers limit? Can the nearest neighbor bondlengths associated with these atoms with more extended wavefunctions be decreased so that a graphitic phase is realized? This question has been addressed earlier in the literature [21,22]. The stability of the planar graphitic structure for the binary semiconductors involving elements beyond the first row were analyzed by studying their phonon dispersions which shows soft phonon modes indicating that these planar structures are unstable at the monolayer limit [19,20] in the literature and a buckled structure for the monolayer has been proposed where the positively charged cations are at a different plane from the negatively charged anions. This structure has a dipole moment associated with it. This is surprising, as a polar surface should be energetically unfavorable. This led us to examine the phonon dispersions and we found that the deepest phonon instabilities were at M and K point. This suggested that a larger unit cell needed to be considered. A non-polar buckled structure was found to have the lowest energy. One would expect that a dominant contribution to the energy favoring the non-polar buckled structure to be associated with the absence of dipoles. Calculating the dipole moment per unit cell and evaluating its contribution to the total energy, one finds that it is negligible as the electronic polarization cancels the ionic polarization. It is purely electronic considerations

of a smaller Coulomb repulsion between electrons on cations and anions in the buckled non-polar structure that leads to a lower energy.

The Coulomb repulsions can be decreased by increasing the cation-anion distance. One of the methods to do this is by application of strain. So the next question we asked was, can strain stabilize the planar graphitic structure in these materials. We took CdS as an example and it was found that a strain of 2% could stabilize a planar graphitic structure. Strain showed some unusual effects on the electronic structure of planar CdS. A strain of 3% was found to bring the valence band maximum (VBM) from Γ in the unstrained case to the K-point in the strained case. This shifting of VBM from Γ to K gives an opportunity to explore spin-valley physics in these materials [23]. The valence band maximum at K is split by spin-orbit interactions. As time reversal symmetry cannot be broken by spin-orbit interactions, the splitting at -K is opposite to that of K. This introduces an additional label to identify levels and the unusual spin-valley physics discussed in the context of transition metal dichalcogenides [24] can be explored here also. This opens up an entire dimension of research in these materials.

4.2.2 Methodology

Monolayers of III-V and II-VI semiconductors have been generated by truncating two monolayers of cation and anion cut out from a bulk wurtzite unit cell [25] growing in the (0001) direction. The in-plane lattice constants (ab plane) were obtained after optimization and a vacuum of 20 Å has been introduced in the c-direction between images in the periodic unit cells used in our calculations. This is needed to break the periodicity along the growth direction and thus to discard the interactions between images otherwise present as we use periodic unit cells. In order to search for possible buckled structures in the monolayer limit, an analysis of the phonon dispersions suggests a larger 6x2x1 supercell. Ground state energies have been calculated within a plane-wave implementation of density functional theory using projector augmented wave (PAW) [26, 27] potentials as implemented in Vienna Ab-initio Simulation Package (VASP) [28]. We have used the local density approximation (LDA) for the exchange correlation functional because earlier work in literature using LDA [29] have found very good agreement between structural and elastic properties [30, 31]. Full geometrical optimization of internal coordinates have been done in absence of any symmetry till an energy convergence of 10^{-5} eV and force convergence of 5 meV/Å have been achieved. A dense gamma centred mesh of 16x16x1 k-points has been used. A cutoff energy of 500 eV has been used for the plane wave basis. We have also used Hybrid functional HSE06 [32] with the Hartree Fock mixing factor

equal to 0.2. To calculate the polarization, we have used the Berry phase [34] method as implemented in VASP.

4.2.3 Results and Discussion

Bulk CdS has wurtzite structure, with a lattice constant of 4.136 Å [25]. From the bulk wurtzite cell of CdS, one layer each of Cd and S were taken in order to examine if a graphitic phase was stable. Atoms were allowed to relax, and a graphitic phase was formed. It was found to be 197 meV/formula unit (f.u) lower in energy than the starting wurtzite derived structure. The wurtzite phase has sp^3 type bonding, whereas the graphitic phase has sp^2 type bonding. During this transformation from a three dimensional structure to a two dimensional one, there is a shortening of Cd-S bondlength in order to compensate for the lost coordination. Bulk Wurtzite and the planar graphitic monolayer are shown in Figure 4.1

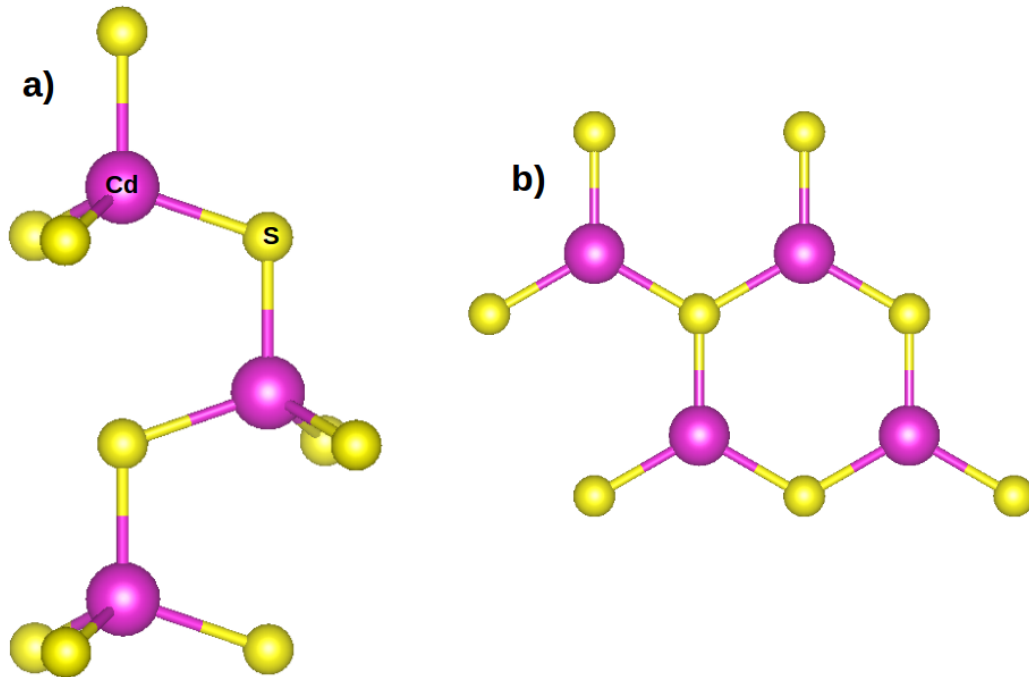


Figure 4.1: a) Bulk Wurtzite structure of CdS b) Planar graphitic structure at the bulk lattice constant.

We then went on to probe if this planar graphitic structure was stable. To study its stability, the phonon dispersions were calculated [35].

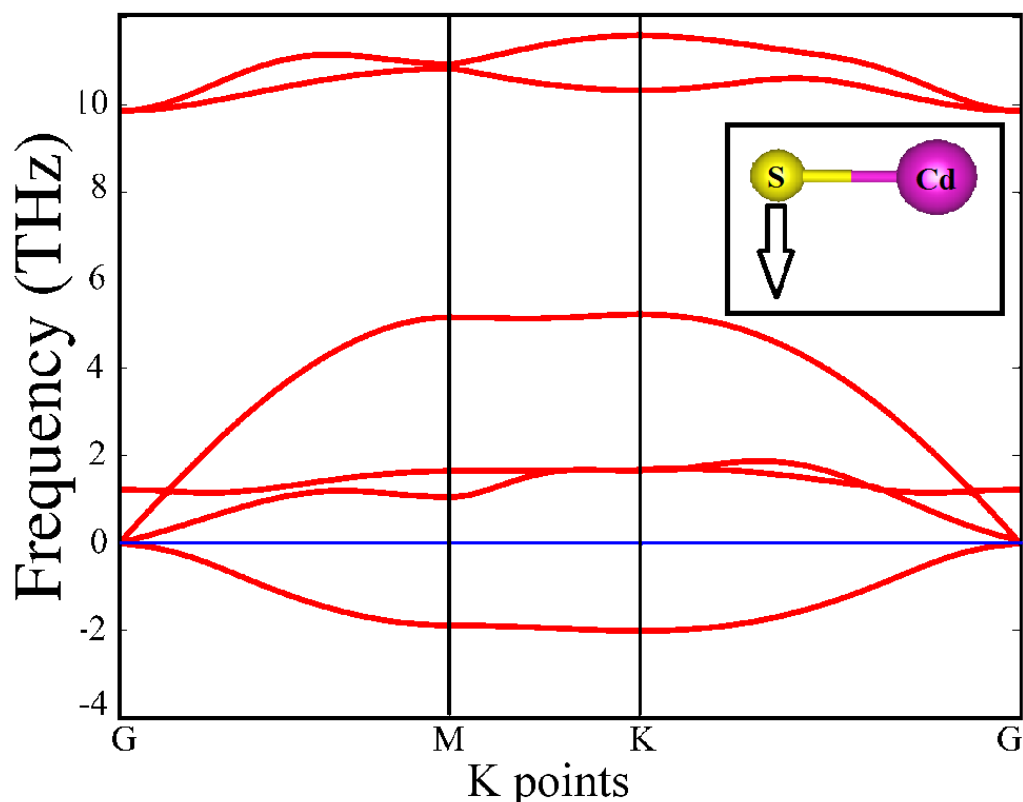


Figure 4.2: The phonon dispersion of graphitic phase of a monolayer of CdS along different symmetry directions using optimized in-plane lattice constants. The displacement of the atoms corresponding to the eigenfunction for the unstable phonon mode in one unit cell are shown in the inset. Reproduced from [35]

Figure 4.2 shows the phonon dispersions for planar CdS. Mode softening for one of the acoustic phonon mode is found along the entire Brillouin zone. This suggests that the planar graphitic structure is not stable. This can be attributed to the fact that the spatial extension of the wavefunction of the valence orbitals of the anions is large for the compounds involving elements beyond the first row. The Coulomb interaction between the electrons on the anions and cations is therefore large. In order to reduce this repulsion, the anions try to move away from the cations by moving out of the plane and the system no longer remains planar. This led to a buckled structure being proposed in the literature, which has cations in one plane and anions in the other. As a result, the system acquires a dipole moment. Consequently, as more layers are added, the surface energy is expected to diverge and the system tries to move away from this point. Therefore polar structures are not expected to be realized beyond a few monolayers [36]. Various mechanisms like surface reconstructions, adsorption of adatoms, vacancy formations, transfer of charges etc. may

help to overcome this polar divergence and for a non-polar structure to be stabilized [37]. We start by examining the structures favored at the monolayer limit.

In order to understand this, we took a closer look at the phonon dispersions. It was found that the deepest phonon instabilities are at M and K points. These have been found to arise from the force on S ion trying to move them out of plane from that of the Cd atoms. The non Γ character of the deepest phonon instabilities suggest that the movement of atoms are in the opposite directions in the neighboring unit cells. This means if a S atom moves out of plane in the upward direction in one unit cell, the S atom in the adjacent unit cell will move in the downward direction. Considering this movement of anions, we constructed a supercell of $6 \times 2 \times 1$ and allowed the atoms to move out of the plane as shown in Figure 4.3. Anions in the plane above and below the cation plane have been indicated with Up and Dn respectively.

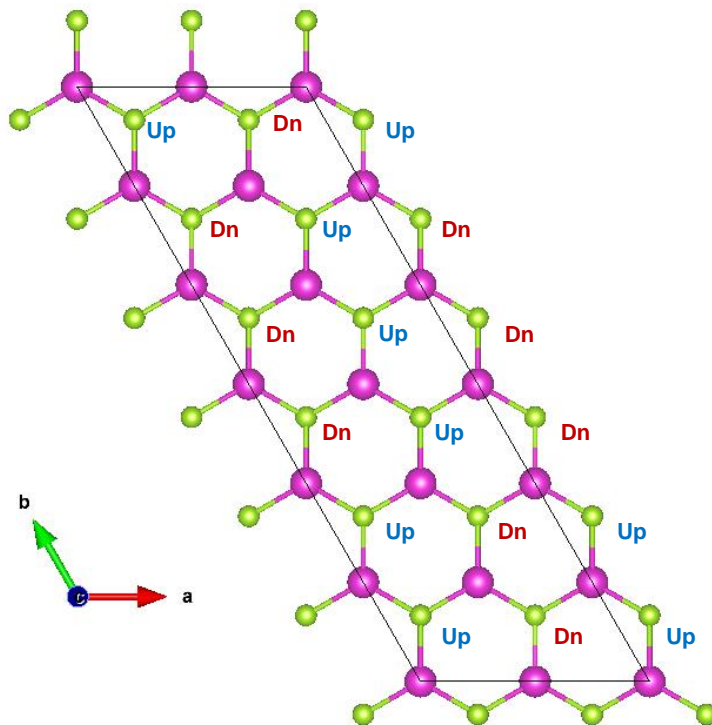


Figure 4.3: Top view of relaxed buckled non-polar structure for CdS where Up(Dn) denotes the anions that have moved in positive(negative) z-direction.

As the unit cell in this case was large, we calculated the phonon dispersion at the gamma point only and the phonon modes were found to be positive. On examining this buckled structure, it was found that it has no net dipole moment as opposed to the previously reported buckled structure. We considered a number of II-VI and III-V binary semiconductors and constructed similar structures for each of them. Energies per formula unit

of each of these structures were calculated and are compared in Table 4.1. Energies per formula unit of both the structures were also calculated using hybrid functionals (HSE06).

	E(BP-P) (eV)	E(NBP-BP) (eV)	E(NBP-BP) (eV) (HSE06)
CdS	0.000	-0.015	-0.016
CdSe	-0.008	-0.049	-0.060
CdTe	-0.027	-0.062	-0.083
ZnS	0.000	-0.011	-0.032
ZnSe	-0.001	-0.039	-0.054
ZnTe	-0.014	-0.050	-0.070
AlP	0.000	-0.018	-0.007
AlAs	-0.016	-0.030	-0.034
GaP	-0.020	-0.029	-0.037
GaAs	-0.091	-0.025	-0.042

Table 4.1: Table comparing the energies of the Planar(P), Buckled Polar (BP) and Buckled Non-Polar(BNP) structures for a monolayer of the listed semiconductor.

It can be seen that the non-polar buckled structure (BNP) is indeed lower in energy than the polar buckled structure (BP) in all the cases, indicating that even at the monolayer limit these semiconductors favor a non-polar structure. One might associate surface energy divergence from a polar surface being the reason for the non-polar buckled structure being lower in energy with respect to buckled polar structure. In order to investigate this, we calculated the dipole moment associated with the polar buckled structure. On analysis we found that indeed the ionic dipole moment is high but the electronic polarization almost compensates the ionic dipole moment. Hence the net dipole moment is very small and is not enough to sustain an electric field. We calculated the net dipole moment and the energy due to this (Table 4.2).

It can be seen that the energy due to the dipole moments are very small. Thus the surface energy divergence due to the presence of dipole moment in the polar buckled structure can not be the reason for it being higher in energy than our non-polar buckled structure.

To understand the reason behind the stability of the non-polar buckled structure we then went on to examined the bondlengths in both the cases. The nearest neighbor cation-anion and anion-anion bondlengths were measured in both the cases. These bondlengths are listed in Table 4.3.

It can be seen that in the non-polar buckled structure, the cation-anion as well as the anion-anion bondlengths have increased compared to the polar buckled structure, due

	Net Dipole moment eÅ	E(dp)meV
CdS	0.0003	0.0
CdSe	0.0824	1.2
CdTe	0.0943	1.3
ZnS	0.0004	0.0
ZnSe	0.0409	0.3
ZnTe	0.0674	0.8
AlP	0.0007	0.0
AlAs	0.0832	1.5
GaP	0.0712	1.2
GaAs	0.0805	1.4

Table 4.2: Table showing the net dipole moment and the energy due to the dipole (E(dp)) for the buckled polar structure.

	Polar Buckled Structure		Non-Polar Buckled Structure	
	Cation-Anion	Anion-Anion	Cation-Anion	Anion-Anion
CdS	2.40	4.16	2.44	4.23
CdSe	2.51	4.32	2.54	4.47
CdTe	2.70	4.59	2.74	4.79
ZnS	2.20	3.80	2.22	3.85
ZnSe	2.31	3.99	2.36	4.09
ZnTe	2.50	4.29	2.55	4.44
AlP	2.24	3.89	2.28	3.96
AlAs	2.35	4.03	2.39	4.16
GaP	2.28	3.87	2.29	3.99
GaAs	2.38	4.01	2.40	4.20

Table 4.3: Table showing the cation-anion and anion-anion bondlengths (in Å) for both polar buckled and non-polar buckled structures

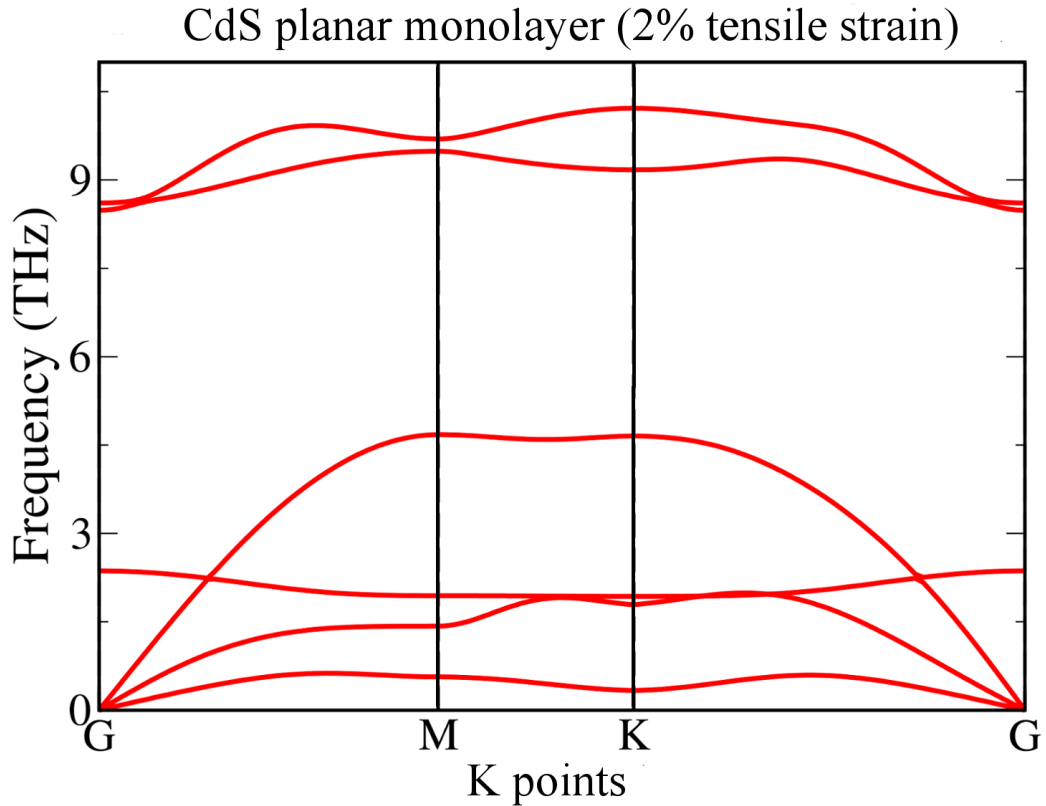


Figure 4.4: Phonon dispersion of monolayer of planar CdS under 2% biaxial tensile strain. This Figure has been taken from Ref([35])

to which the Coulomb repulsion between the electrons on different atoms reduces, which lowers the energy of the non-polar buckled structure. This idea has been further supported by a breakup of the total energy into various components and is given in the Table 4.4

In order to further verify if that is the case, we constructed non-polar buckled structure keeping the cation-anion bond lengths same as that of the polar buckled structure and calculated the energies. It was seen that the difference in energies are now very small and can be attributed to the difference in anion-anion bond lengths. Hence it can be concluded from this analysis that the only reason for the non-polar buckled structure to be favored is the increase in bond length which reduces the Coulomb repulsion between the electrons on different atoms.

Another method of decreasing the Coulomb repulsion between the electrons is by subjecting the system to biaxial tensile strain. A strain of 2%, 3% and 4% was applied on planar CdS monolayer and their stabilities were checked by studying their phonon dispersions [35]. Figure 4.4 shows phonon dispersions for 2 % strained planar graphitic structure.

		CdS	CdSe	CdTe	ZnS	ZnSe	ZnTe	AlP	AlAs	GaP	GaAs
Hartree	BP	4,099.398	3,824.221	3,452.448	5,292.867	4,905.700	4,402.119	722.301	653.601	722.560	654.318
Energy(eV)	BNP	4,040.153	3,745.800	3,375.044	5,233.907	4,818.262	4,321.735	703.309	629.739	698.752	624.183
Ewald	BP	584.986	469.903	315.343	877.073	705.759	483.440	163.718	136.824	163.084	135.778
Energy (eV)	BNP	554.377	429.458	275.408	846.204	659.641	441.335	153.488	124.534	150.769	120.501
-V(xc)+	BP	18.948	6.312	-21.749	70.256	57.595	29.451	-22.247	-37.219	-15.853	-30.733
E(xc) (eV)	BNP	18.826	6.172	-21.874	70.158	57.456	29.338	-22.363	-37.306	-15.916	-30.789
Eband	BP	-184.646	-186.566	-175.230	-176.038	-178.163	-164.470	-60.040	-60.836	-65.032	-65.326
(eV)	BNP	-183.772	-185.504	-174.198	-174.856	-176.056	-162.814	-59.246	-60.451	-64.634	-65.129
Eatom	BP	1,573.422	1,554.933	1,521.383	2,031.431	2,012.943	1,979.393	230.307	225.467	236.276	231.435
(eV)	BNP	1,573.422	1,554.933	1,521.383	2,031.431	2,012.943	1,979.393	230.307	225.467	236.276	231.435
PAW double	BP	33.498	42.913	68.399	-178.507	-168.800	-142.842	38.863	51.666	30.858	43.701
counting(eV)	BNP	33.717	43.176	68.661	-178.215	-168.408	-142.523	38.901	51.695	30.906	43.744
Alpha Z	BP	16.871	18.647	12.800	14.763	16.910	10.372	0.415	1.624	2.694	3.759
(eV)	BNP	16.871	18.647	12.800	14.763	16.910	10.372	0.415	1.624	2.694	3.759

Table 4.4: Table showing the breakup of the total energies in the ab-initio calculations performed using VASP are given. The energy associated with the sum of the occupied eigenvalues is called Eband. It also includes the Hartree energy(electron-ion interaction). This is the reason why 1/2 of the Hartree energy must be subtracted out while evaluating the total energy. Ewald energy is the ion-ion interaction term.E(xc) and V(xc) are energies associated with the exchange and correlation functional. The PAW double counting accounts for the double counting in the Hartree energy. All components in the above Table must be added except the Hartree energy. 1/2 times the Hartree energy must be subtracted out in order to get the total energy.

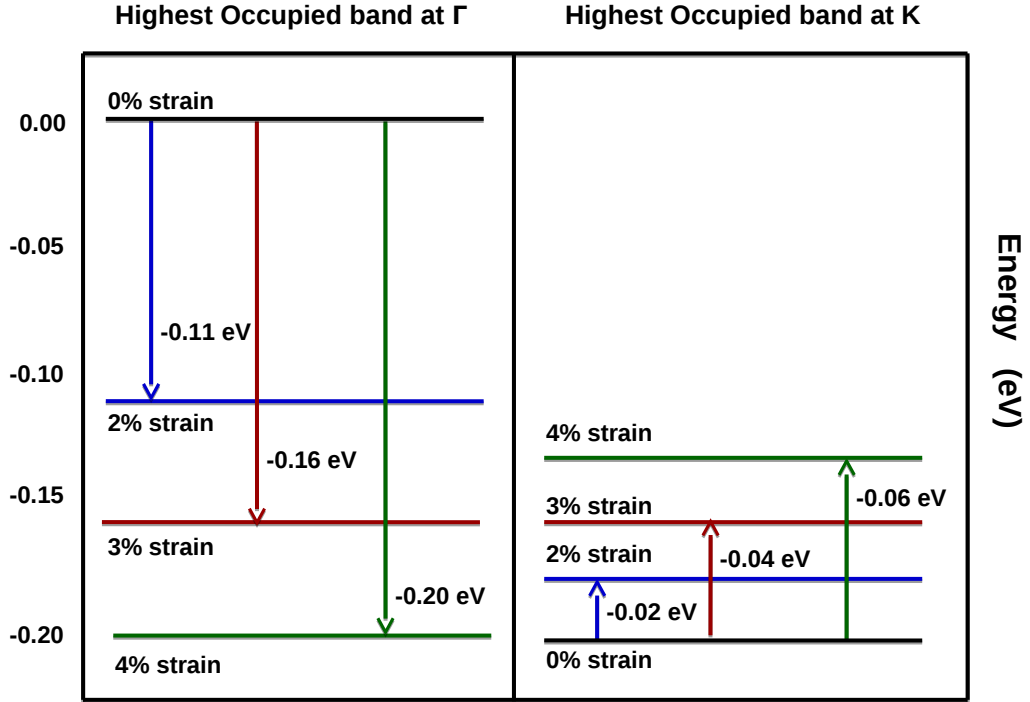


Figure 4.5: Shift in Energy (in eV) of the highest occupied bands at Γ and K on application of strain in planar CdS.

It can be seen that only positive phonon modes are present, indicating that the structure is stable. Thus we have a rare realization of a sp^2 bonded phase for CdS. We then went on to examine the effect of biaxial tensile strain on the electronic structure of CdS monolayer. The unstrained films are found to have their valence band maximum at Γ . The highest occupied band at K is ~ 0.2 eV deeper inside the valence band (Figure 4.5).

An analysis of the charge density (Figure 4.6) reveals that the valence band maximum emerges from interactions between the Cd $d_{x^2-y^2}$, d_{xy} and S p_y orbitals. However the highest occupied band at K is contributed by anion-anion interactions between the S p_z orbitals. An empirical scaling law given by Harrison provides a relation of how the hopping interaction strengths would scale with distance. According to this law, the pd interactions scale as $\frac{1}{r^4}$ while the pp interactions scale as $\frac{1}{r^3}$. This immediately provides us with a handle of being able to control this separation. Introducing an in-plane tensile strain, we find that, a 3% tensile strain pushes the highest occupied band at Γ , ~ 0.16 eV deeper. This emerges from the fact that these states are from antibonding Cd $d_{x^2-y^2}$, d_{xy} and S p_y interactions which moves deeper into the valence band as the strength of this interaction is decreased. The variations are depicted pictorially in Figure 4.5, where the electrostatic potential on a Cd atom are used as an internal energy reference to compare

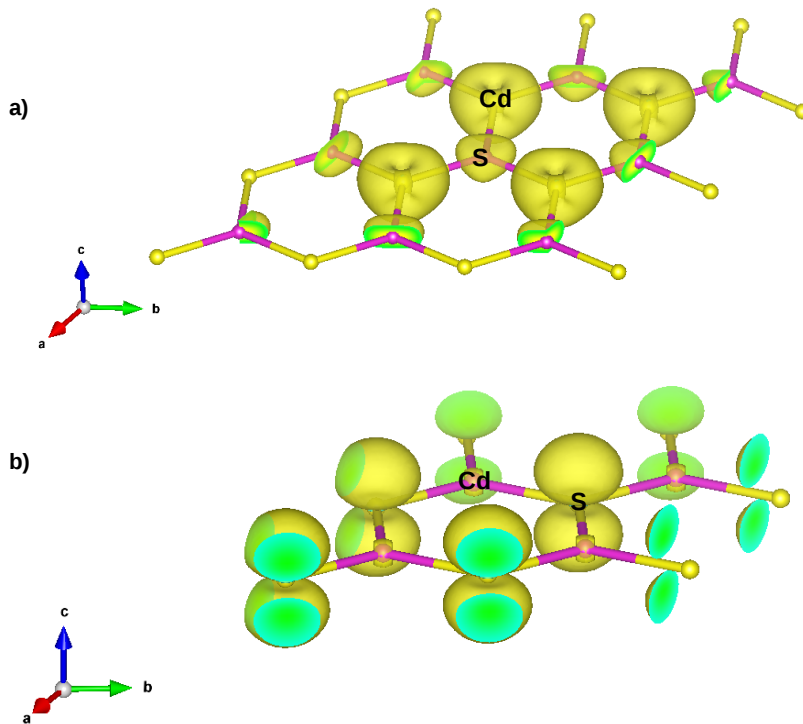


Figure 4.6: Charge density of the highest occupied band at Γ and the charge density of the highest occupied band at K-point in planar CdS.

the movement of the highest occupied band between different calculations. There seems to be an apparent movement of the highest occupied band at K to higher energies. The movements are much smaller than that of the band at Γ , suggesting that other effects such as charge transfer between Cd and S could modify the onsite energies, and lead to the observed movement of the band to higher energies. The important consequence of applying strain is that the band extrema shifts to K point at 3% strain. As discussed in the introduction, spin-orbit effects lead to a spin splitting of the highest occupied band at K point. This is found to be ~ 20 meV in CdS and increases to ~ 50 meV in CdTe. This would then make these systems also important candidates for probing spin valley physics, and additionally introduce drastic change in their transport behavior. This work has been published in [38]. Another method to make use of this phenomenon is to use materials where spin-orbit coupling strength is large like in heavy metals. In the next section we discuss the realization of quasi free standing monolayer of a heavy metal taking bismuth as an example.

4.3 Route to planar Bismuthene

4.3.1 Introduction

Some members among two dimensional materials have been identified as topological insulators [39–44] which can be potential candidates to be used in electronic industry. Topological insulators are materials which have an insulating bulk gap, residing in which are robust metallic edge states which are insensitive to scattering by non-magnetic impurities. The properties of the edge states makes them suitable candidates for applications in devices and hence there has been an avalanche of interest in the study of these materials. More and more emphasis is being given in identifying and exploring such materials [45–47]. Quantum Spin Hall (QSH) insulator is one such class of recently discovered two dimensional materials, in which electrons with up and down spins move in opposite directions along the edge of the material. The successful theoretical model explaining QSH insulator was given by Kane and Mele in 2005 [48, 49]. Subsequently in 2007 it was observed experimentally in (Hg,Cd)Te [50]. After that, a lot of materials like silicene, germanene, stanene, bismuthene etc have been predicted and shown to be quantum spin hall insulators [51–53]. Most of these studied materials have very small band gap which limits their operation to very low temperatures. Efforts are being made to realize such materials with larger bandgap.

As a dominant contribution to the band gap is from spin-orbit interactions, heavier metal atoms such as bismuth, antimony etc. were suggested as alternate candidates which could give rise to a large band gap and consequently a room temperature quantum spin hall effect [54, 55]. A lot of predictions of the properties of graphitic analogues with heavier metals have been on freestanding substrates [56, 57]. In this work we identify a few important criteria which would help us usefully implement the ideas developed for freestanding members to those grown on a substrate.

In the previous section of this chapter we had shown that considering various III-V and II-VI semiconductors which involve elements beyond the first row, freestanding graphitic monolayers were found to be unstable. This was traced to the coulomb interactions between electrons on neighbouring atoms destabilizing the structure. In these two dimensional structures, the nearest neighbour bondlengths are a few percent smaller than the structures in three dimensions. This is primarily driven by the reduced coordination they have in the graphitic phase and this drove the structural instability. As a result the atoms adopted a buckled structure which allowed them to reduce the Coulomb interactions between electrons on neighbouring atoms. Biaxial tensile strain of just a few percent

increased the cation-anion bondlengths and thereby reduce the Coulomb interactions between electrons on neighbouring atoms. This stabilizes the structure. This required strain can be provided by a substrate.

Also, in order to be able to use these monolayers for any device application, we need a substrate. It holds the material as well as assists in its transferability. The substrate, apart from providing the necessary strain for a graphitic growth should also be able to interact weakly with the heavy metal so that it is not dislodged by the slightest amount of vibration. At the same time, the interaction strength should be small so that it does not modify the electronic structure of the heavy metal monolayer drastically.

In this work we have studied the properties of monolayer of bismuth (bismuthene), both free standing and on different substrates. Our results indicate a stabilization of the planar graphitic phase at a strain of 15.4%. We studied bismuthene on Ag(111) substrate, where it does provide the necessary strain for graphitic growth but Ag being metallic interferes with the bismuth states near the Fermi energy and makes it metallic. We then studied its growth on a hydrogenated SiC(0001) surface. We analyzed the energetics involved in bismuth atoms replacing the hydrogen and found that it is energetically more favorable for the bismuth atom to sit on top of the hydrogenated substrate. We then went on to examine the electronic structure of this monolayer of planar bismuth formed on hydrogenated SiC(0001). Hydrogenated SiC has a gap of 3.54 eV and Bi when grown on it, introduces states within the gap. Similar to freestanding bismuthene we have two Dirac cones at K point. One from p_z and the other from p_x and p_y . However neither is at the Fermi level. It thus needed orbital filtering to show properties similar to QSH insulators. We then put one layer of hydrogen on top of bismuth so that it interacts with the p_z orbitals of bismuth and moves it away from the Fermi level. The electronic structure now has a Dirac cone at the K point which opens up a gap of 0.8 eV when spin-orbit interactions were introduced. Finally the nature of interaction of bismuth layer with that of the hydrogenated substrate is discussed. It was seen that there is a small change in the electrostatic potential, when bismuth is added on the hydrogenated substrate indicating a small charge transfer. This keeps the bismuth layer attached to the substrate. We have thus found a mechanism of growing bismuthene over SiC(0001) surface such that a quasi free standing planar graphitic form of bismuth is formed, keeping its electronic structure intact.

4.3.2 Methodology

The bandstructure was calculated within a projector augmented-wave (PAW) [26, 27] method implementation of density function theory (DFT) within the Vienna Ab-initio Simulation Package (VASP) [28]. The lattice parameters were kept fixed at the experimental values while the internal positions were optimized in each case. In addition to the optimization of internal positions, we included the optimization of the separation between different layers. This was done including van der Waals interactions implemented using the DFT-D2 method of Grimme [58]. The electronic structure was solved self consistently using a k-point mesh of $21 \times 21 \times 1$. The plane-wave energy cut-off was taken as 500 eV. Perdew Burke-Ernzerhof potentials were used for the exchange correlation functional [59, 60]. Freestanding monolayer of bismuth was generated by truncating two layers of bismuth atoms from the bulk bismuth unit cell grown in 001 direction. A vacuum of 20 Å was introduced in the c-direction between images in the periodic unit cells used in our calculations. This is needed to break the periodicity along the growth direction and thus to prevent the interactions between images otherwise present as we use periodic unit cells.

4.3.3 Results and Discussion

We begin by looking at the bulk structure of bismuth. In its bulk form bismuth has trigonal crystal structure with $a = b = 4.54$ Å and $c = 11.86$ Å, $\alpha = \beta = 90^\circ$ and $\gamma = 120^\circ$ [61]. For any Bi atom the first nearest neighbor distance is 3.07 Å and is in a plane 1.59 Å above it. It forms layers of buckled hexagon, with each alternate atom in the hexagon moving out of the plane and each layer being separated from the other by 2.36 Å as can be seen in the structure shown in Figure 4.7.

In our previous work on semiconductors involving elements beyond the first row of the periodic table, we explored the possibility of a freestanding stable graphitic monolayer. As we go down the periodic table, the wavefunction of the valance electrons become more extended. This increases the Coulomb repulsion between the electrons on neighbouring atoms, which makes the planar graphitic structure unstable and the system goes to a buckled structure. A method explored to reduce the Coulomb repulsion was by applying strain to the planar graphitic structure. A small biaxial tensile strain of 2% on CdS was found to make it stable. As mentioned earlier and also indicated in Figure 4.7, two layers of bismuth taken together form a buckled hexagon. The question we asked at this point was can planar graphitic structure be stabilized with strain? In order to answer this we

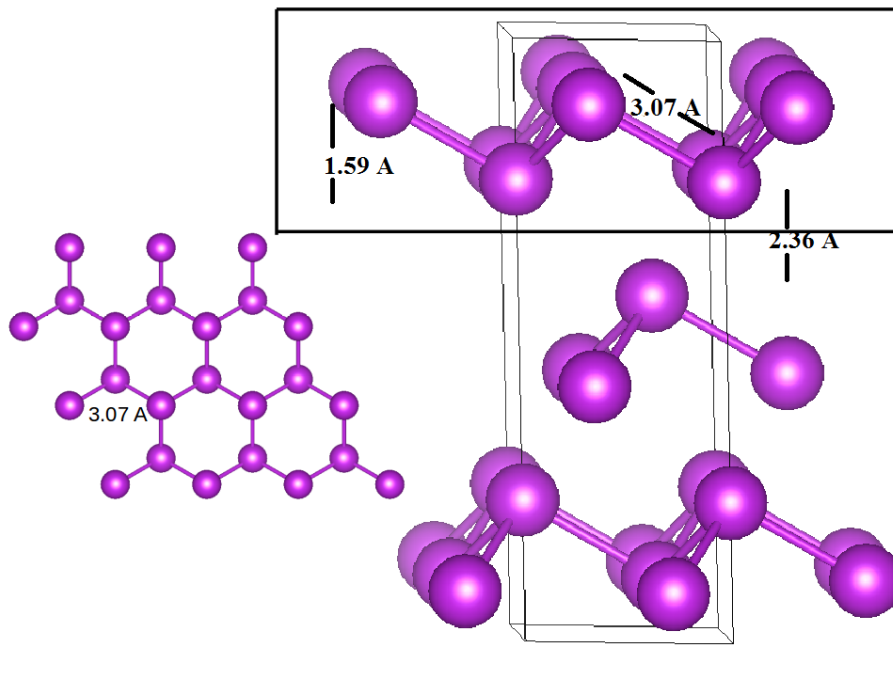


Figure 4.7: Structure of bulk Bismuth

calculated the total energy for both buckled and planar monolayer of bismuth by varying the lattice constant in steps of 0.1 Å. The results are shown in Figure 4.8

We find that near the bulk lattice constant, energy of the buckled monolayer was lower than the planar graphitic one. As we start increasing the strain the energy of the planar graphitic phase starts decreasing and around a lattice constant of 5.24 Å which corresponds to a strain of 15.4%, there is a crossover and the energy of the planar graphitic structure is lower than its buckled counterpart. This strain could be provided by a suitable choice of substrate and depending on the interaction of the substrate with the bismuthene monolayer, the percentage of strain which can stabilize a planar graphitic structure can vary.

Before discussing the substrate and its role in determining the electronic structure of bismuthene, we examine the electronic structure of this freestanding planar graphitic monolayer of bismuth. The bandstructure for planar freestanding bismuthene is shown in Figure 4.9

The bandstructure of freestanding bismuthene show some interesting features. We can see that at the K point in the Brillouin zone p_x , p_y and p_z orbitals form two Dirac points, which are slightly shifted from the Fermi energy. In order to bring the Dirac point to the Fermi energy one needs to push the p_z bands out by orbital filtering. This can be done by using a substrate, which will interact with the p_z band bring the Dirac point formed by

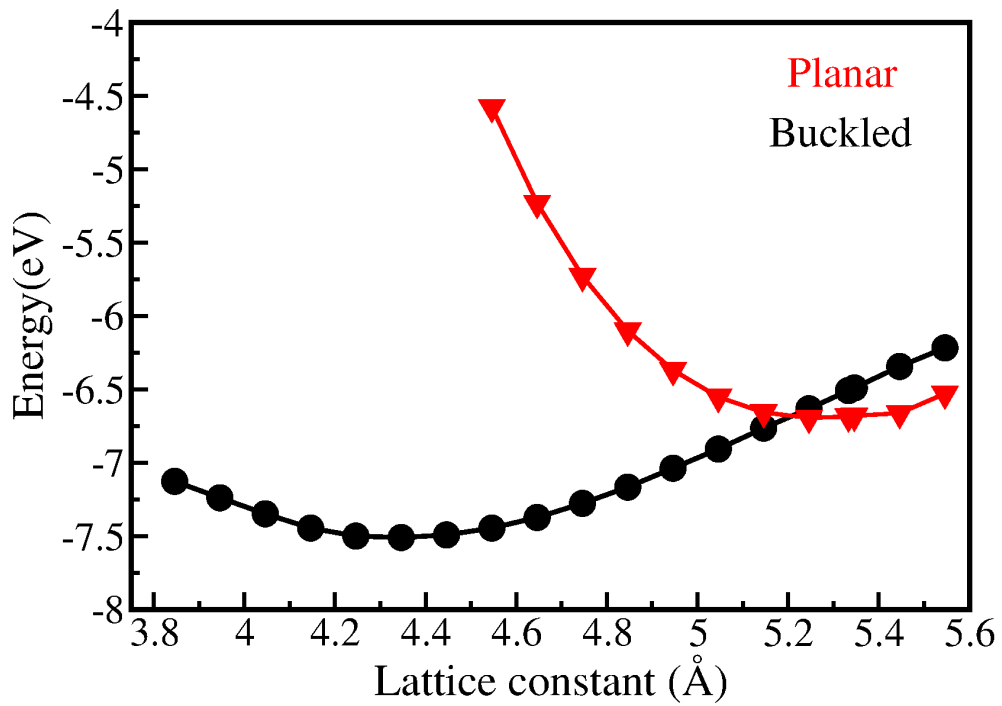


Figure 4.8: Variation of Energy with lattice constant for freestanding planar and buckled Bismuthene

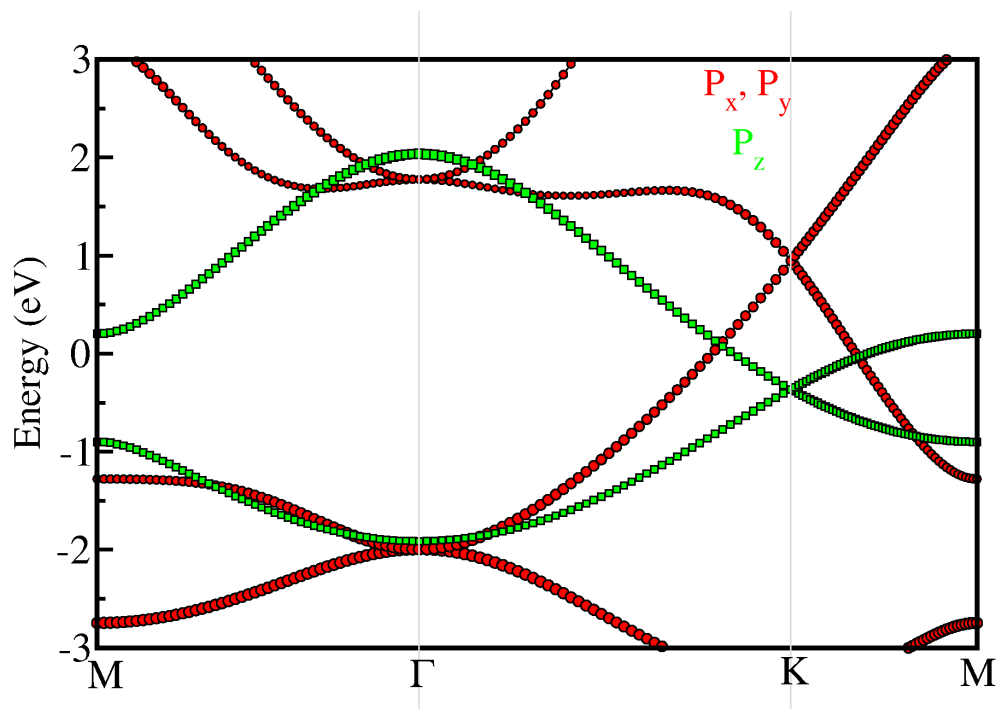


Figure 4.9: Bandstructure of planar freestanding bismuthene calculated along various symmetry directions

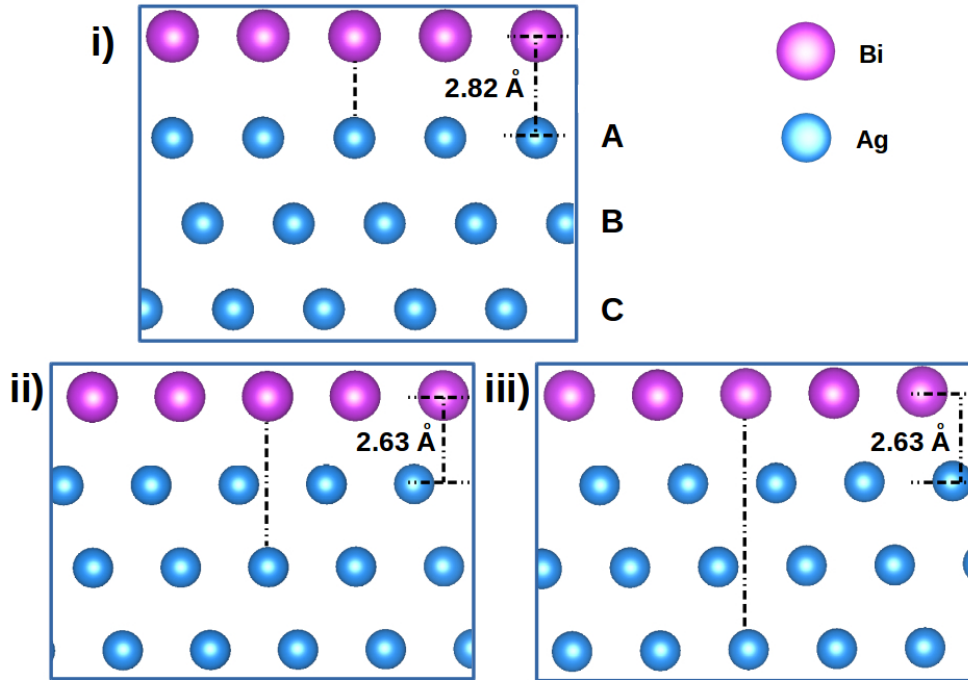


Figure 4.10: Layer of bismuth atoms on Ag(111) slab

p_x and p_y orbitals to the Fermi energy. The substrate apart from providing the strain for the planar graphitic structure to be stabilized also helps in keeping the monolayer intact and helps in its transferability.

We looked for possible substrates which can be used. Ag(111) surface has been used often in literature as a possible substrate to grow monolayers of heavy metals [63,64]. Ag has a lattice constant of 4.085\AA [62]. Ag(111) surface with a reconstruction of $\sqrt{3}\times\sqrt{3}$ R 30° has a lattice constant of 5.004\AA . This corresponds to a strain of 10.22%. We explored this as a candidate for the substrate to grow planar bismuthene. We constructed a slab of Ag(111) with 10 Ag layers. Bismuth atoms were placed on both the surfaces of the slab to make it symmetric. Ag(111) has ABC stacking as shown in Figure 4.10 i). There are three possibilities where the bismuth atom can sit. We explored all three possibilities as shown in Figure 4.10

We found that configuration i) where the bismuth atom sits on top of the top layer of the Ag atoms of the slab to be the lowest in energy. This suggests it prefers atom on atom growth because bonding in such cases is favored compared to the other two cases. We then went on to examine the electronic structure of this structure. This is shown in Figure 4.11. We can see that since Ag is metal, bands associated with it crosses the Fermi energy and makes the system metallic.

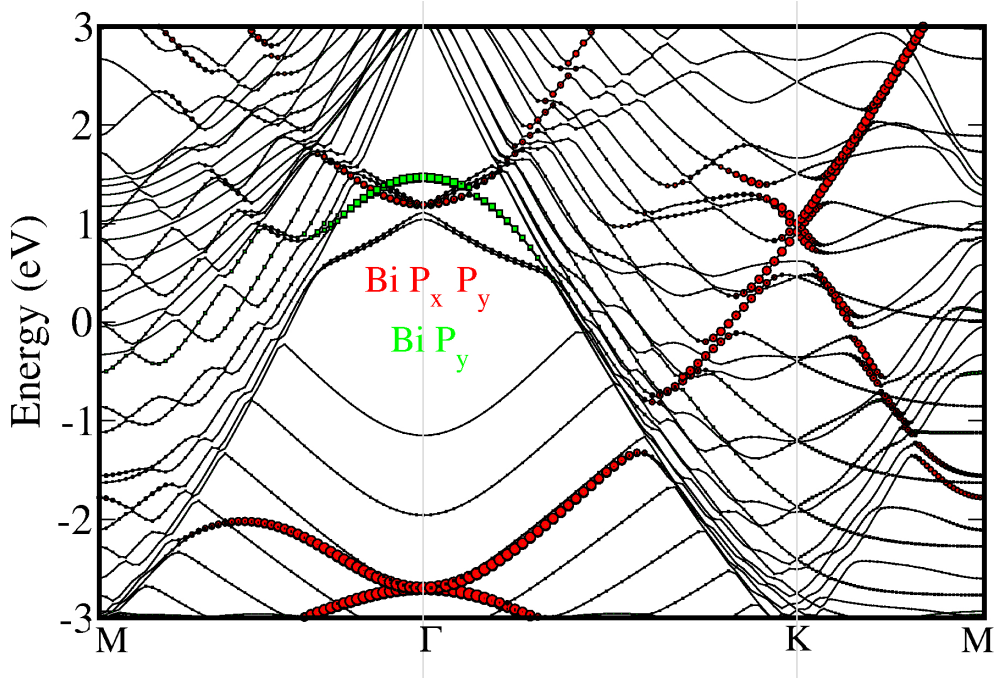


Figure 4.11: Bandstructure of bismuthene on Ag(111) substrate calculated along various symmetry directions

We then went on to examine other possible substrate to grow bismuthene. SiC(0001) has been considered a good choice in literature since it is a semiconductor. Single monolayer of Bismuth grown on SiC(0001) substrate has been shown to be a topological insulator. We first examined the route proposed to achieve this in detail [67]. SiC has a bulk lattice constant 3.079 \AA [65]. $\sqrt{3} \times \sqrt{3} \text{ R } 30^\circ$ supercell of SiC has a therefore a lattice constant of 5.333 \AA . Starting from the bulk wurtzite structure of SiC, we took two layers of SiC terminated with Si on top. We then passivated it on both the sides with hydrogen atoms to remove the dangling bonds. We examined the bandstructure of this hydrogenated SiC and found it to have a bandgap of 3.56 eV . The hydrogenated SiC structure and its bandstructure calculated along various symmetry directions are shown in Figure 4.12.

On this hydrogenated SiC we examined the possible mechanism of placing bismuth. One of the possibilities discussed in literature is that the bismuth atom replaces the hydrogen atom and forms a bond with the silicon atom [67]. We examined this process carefully and calculated the energy involve in this process. We calculated the formation energy when a hydrogen is removed from the hydrogenated SiC and also when a Bi atom replaces one hydrogen. In order to calculate the formation energies we used the following formula [66]

$$\Delta H_f(\alpha) = E(\alpha) - E(0) + \sum_{\alpha} \Delta n_{\alpha} \mu_{\alpha}^a \quad (4.1)$$

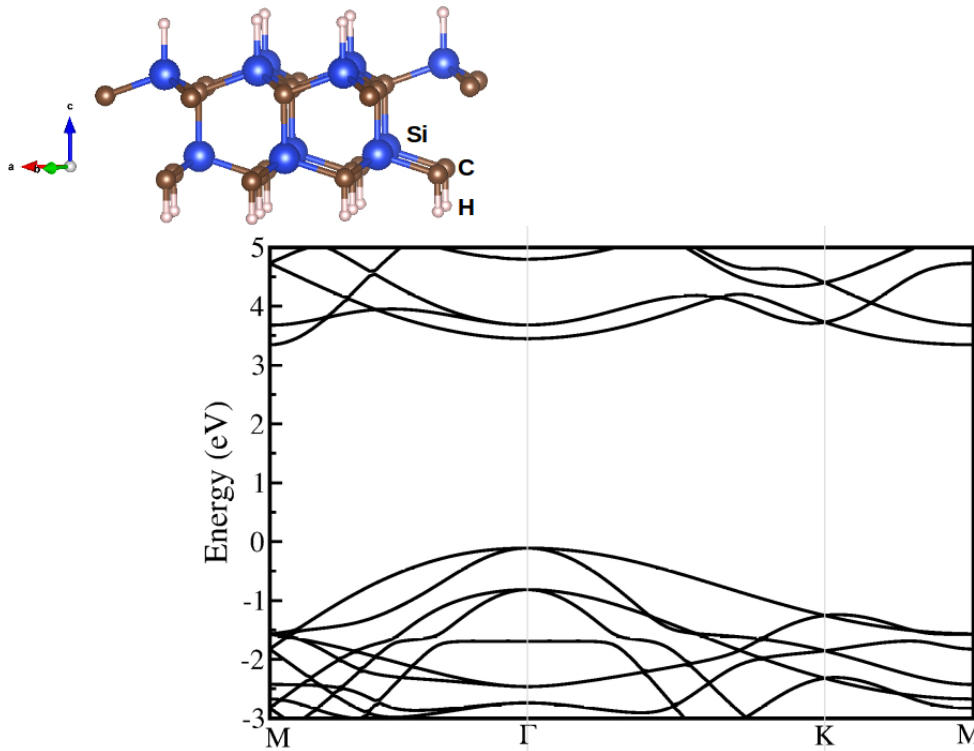


Figure 4.12: Hydrogenated SiC and its bandstructure calculated along various symmetry directions.

Here, $E(\alpha)$ represents the total energy of the supercell with defect α and $E(0)$ is the total energy of the supercell without defect. The number of defect atoms is given as n_α . The value of $n_\alpha = -1$ if an atom is added, while when an atom is subtracted $n_\alpha = 1$. μ_α^a is the absolute value of the chemical potential of a given atom labeled as α . Now as we know, the formation energies are defined with respect to the elemental solid(s), μ_α^a is given as the sum of all the components because of element in its most commonly occurring structure μ_α^s and excess chemical potential μ_α ($\mu_\alpha^a = \mu_\alpha^s + \mu_\alpha$). In our case μ_α^s for H and Bi are energies obtained after full optimization of elemental solids in their observed crystal structures. For our case μ_α of Bi is negligible as we examined the formation energy of BiH_3 and it was very small.

Using this, we found that the formation energy of removal of a hydrogen atom from hydrogenated SiC surface was 4.14 eV and the formation energy of replacing a Bi atom with that of a hydrogen atom from the hydrogenated SiC substrate was 4.76 eV. We have depicted these two processes in the Figure 4.13.

We then went on to explore another route to achieve planar bismuthene on SiC substrate. We placed two bismuth atoms on top of hydrogenated SiC. They sit at a height of 2.96 Å from the hydrogen layer. Using Equation 4.1 we calculated the formation energy of

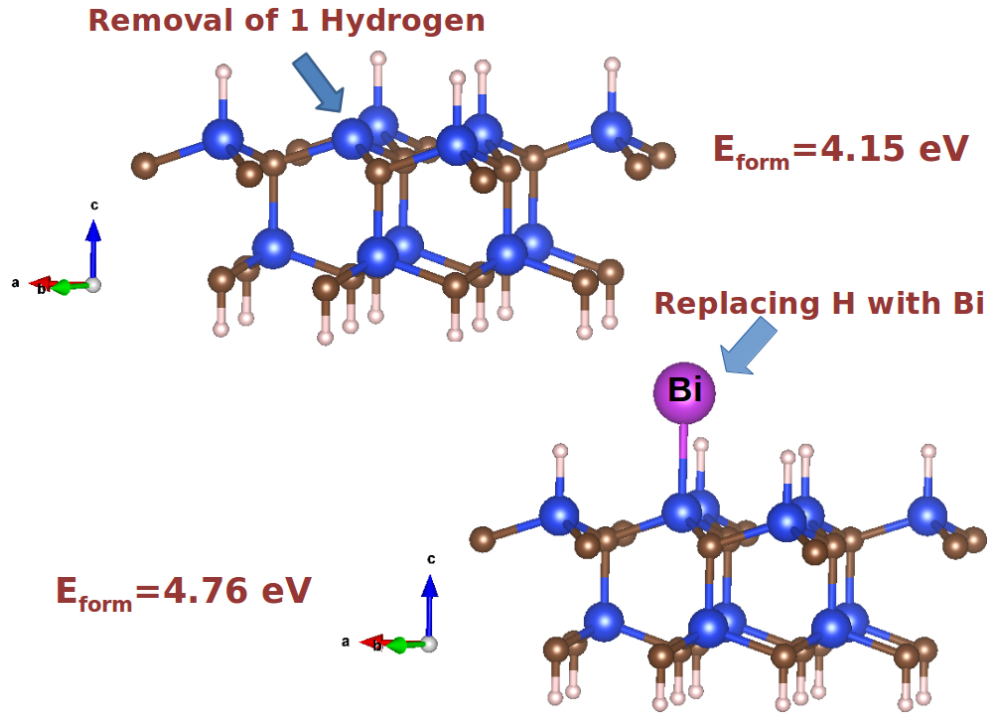


Figure 4.13: Formation energies involved in obtaining Bismuthene

this process and we find it to be 0.53 eV. From this analysis, we can say that, Bi atoms would prefer to sit on top of hydrogenated SiC rather than replacing a hydrogen. We then examined the bandstructure of this structure. This has been shown in Figure 4.14.

On examining this bandstructure we find it remarkably similar to the bandstructure of a freestanding bismuthene which is shown in Figure 4.9. It has all the features of a free standing layer of bismuthene. Thus by growing bismuth on top of a hydrogenated SiC substrate, we obtain a planar graphitic bismuthene with all the features predicted for its freestanding form. Similar to its freestanding counterpart, this structure also needs orbital filtering to get the dirac point at Fermi energy. In order to do so, we place hydrogen again on top of the bismuth layer so that it interact with its p_z orbitals and push it away from the gap region. We then calculated the bandstructure of this quasi freestanding bismuthene. It is shown in Figure 4.15.

The bandstructure of this quasi freestanding bismuthene thus obtained now has the Dirac point at the fermi energy. This quasi freestanding bismuthene obtained by this method has the properties of a topological insulator of having the Dirac point at the Fermi energy. It is also important that this quasi free standing monolayer of bismuth remains attached to the substrate. This can happen if there is some interaction between the substrate and the Bismuth layer. We therefore investigated the nature of interaction between the Bi monolayer and the substrate. For this we looked at the possibility of charge transfer

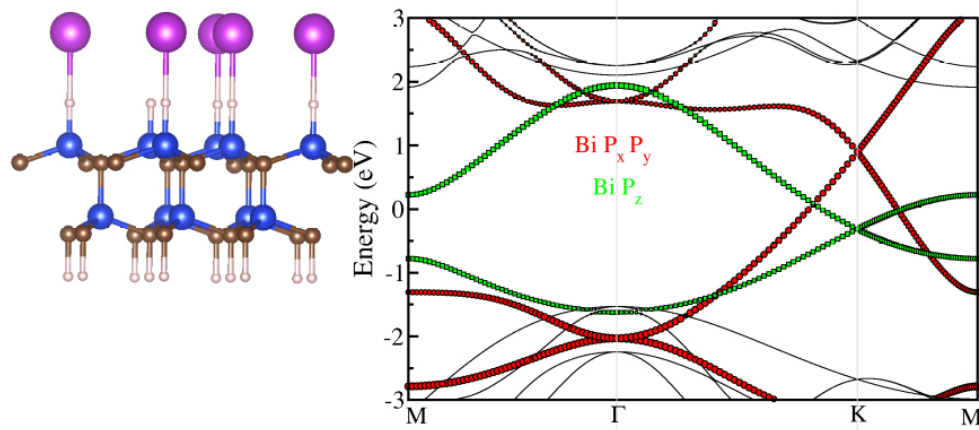


Figure 4.14: Hydrogenated SiC with a layer of Bi on top of H and its bandstructure calculated along various symmetry directions.

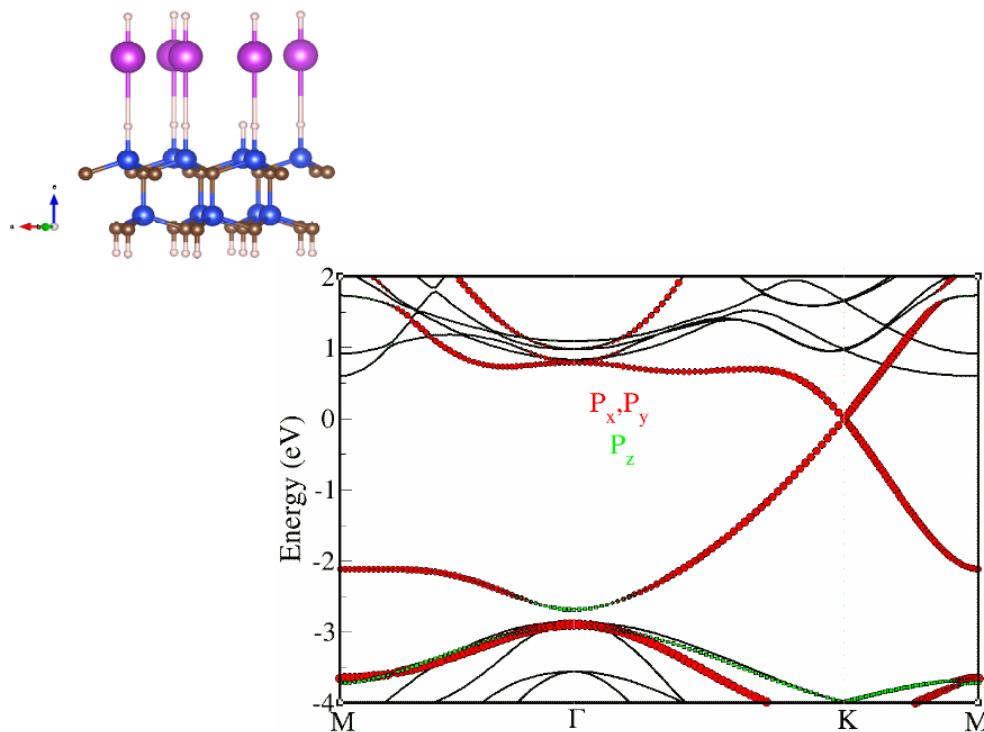


Figure 4.15: Quasi freestanding bismuthene its bandstructure calculated along various symmetry directions.

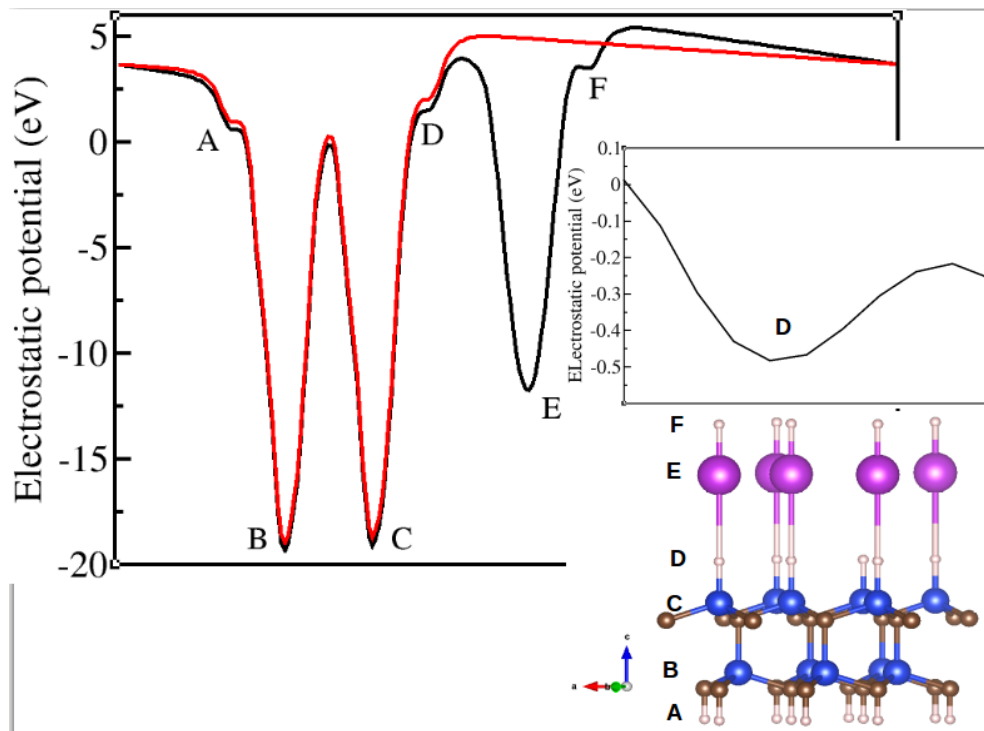


Figure 4.16: Electrostatic potential of the substrate and the quasi freestanding bismuthene

which can lead to bonding between the layers. In order to study that we looked at the electrostatic potential of the substrate and the quasi freestanding bismuthene. This has been shown in Figure 4.16.

In Figure 4.16, the red curve is for the substrate while the black one is for the quasi freestanding bismuthene. A, B, C, D, E and F represent the position of H, C-Si first layer, C-Si second layer, H, Bi and H respectively (shown in inset of Figure 4.16). We wanted to understand the interaction between the bismuth layer and the hydrogenated substrate so we examine the curves around point D. This portion is zoomed in and shown in the inset of Figure 4.16. It shows the difference between the two curves. We can see that due to the presence of bismuth layer in the black curve there is a significant deviation from the red one. This conclusively shows that there is a weak interaction between the hydrogenated substrate and the bismuth layer, leading to a small charge transfer which will keep the bismuth layer intact over the surface.

4.4 Conclusion

In conclusion, the present investigation examines the structure favoured by monolayers of group II-VI and III-V semiconductors. A non-polar buckled structure has been found to

be energetically more favourable than a polar buckled one. Reduced Coulomb repulsion between the electrons on the anion and cations because of increased bondlengths in the non-polar structure compared to the polar one plays a major role in stabilizing it. A biaxial tensile strain of 2% is capable of eliminating the buckling in such structures stabilizing a graphitic analogue. Additionally, with 3% biaxial tensile strain, the position of the VBM shifts from Γ to K point which makes them suitable candidates for exploring spin valley physics.

We further went on to explore the formation of free standing monolayer of heavy metals taking Bismuth as an example. They have been predicted to be large gap topological insulators. The realization of such models have failed as the presence of a substrate for growing the monolayers, usually interacts with the monolayer and makes its properties substantially different from that of a freestanding one. We have explored a route to quasi free-standing bismuthene, and additionally a possible explanation for the growth of quasi free standing bismuthene on a substrate that has been explored experimentally.

Bibliography

- [1] H. Tang and S. Ismail-Beigi Phys. Rev. Lett. **99**, 115501 (2007).
- [2] S. Zhao, Z. Li, and J. Yang J. Am. Chem. Soc **136**, 13313 (2014).
- [3] S. Cahangirov, M. Topsakal, E. Aktürk, H. Sahin, and S. Ciraci Phys. Rev. Lett. **102**, 236804 (2009).
- [4] W. Yu, Chun-Yao Niu, Z. Zhu, X. Wang and Wei-Bing Zhang J. Mater. Chem. C **4**, 6581 (2016).
- [5] S. Demirci, N. Avazli, E. Durgun, and S. Cahangirov Phys. Rev. B. **95**, 115409 (2017).
- [6] C. Sevik, D. Cakir, O. Gülseren, and F. M. Peeters J. Phys. Chem. C **120**, 13948 (2016).
- [7] F. Schwierz, J. Pezoldt and R. Granzne Nanoscale **7**, 8261 (2015).
- [8] B. Radisavljevic, A. Radenovic, J. Brivio, V. Giacometti, and A. Kis, Nat. Nanotechnol. **6**, 147 (2011).
- [9] Y. Zhang, J. Ye, Y. Matsushashi, and Y. Iwasa, Nano Lett. **12**, 1136 (2012).
- [10] Z. Yin, Hai Li, Hong Li, L. Jiang, Y. Shi, Y. Sun, G. Lu, Q. Zhang, X. Chen, and H. Zhang, ACS Nano **6**, 74 (2012).
- [11] H. Fang, S. Chuang, T. C. Chang, K. Takei, T. Takahashi, and A. Javey, Nano Lett. **12**, 3788 (2012).
- [12] Feng-Chuan Chuang, Liang-Zi Yao, Zhi-Quan Huang, Yu-Tzu Liu, Chia-Hsiu Hsu, T. Das, H. Lin, and A. Bansil Nano Lett. **14**, 2505 (2014).

-
- [13] Z. Y. Al Balushi, K. Wang, R. K. Ghosh, R. A. Vila, S. M. Eichfeld, J. D. Caldwell, X. Qin, Yu-Chuan Lin, P. A. DeSario, G. Stone, S. Subramanian, D. F. Paul, R. M. Wallace, S. Datta, J. M. Redwing and J. A. Robinson *Nat. Mat.* **15**, 1166 (2016).
- [14] A. Onen, D. Kecik, E. Durgun, and S. Ciraci *Phys. Rev. B.* **93**, 085431 (2016).
- [15] D. R. Kripalani, A. A. Kistanov, Y. Cai, M. Xue, and K. Zhou *Phys. Rev. B.* **98**, 085410 (2018).
- [16] F. Claeysens, C. L. Freeman, N. Allan, Y. Sun, M. N. R. Ashfolda, and J. H. Harding, *Journal of Mater. Chem.*, **15**, 139 (2005).
- [17] C. Tusche, H. L. Meyerheim, and J. Kirschner, *Phys. Rev. Lett.* **99**, 026102 (2007).
- [18] B. Rakshit, and P. Mahadevan, *Phys. Rev. Lett.* **107**, 085508 (2011).
- [19] A. K. Singh, H. L. Zhuang, and R. G. Hennig *Phys. Rev. B.* **89**, 245431 (2014).
- [20] H. Sahin, S. Cahangirov, M. Topsakal, E. Bekaroglu, E. Akturk, R. T. Senger and S. Ciraci *Phys. Rev. B.* **80**, 155453 (2009).
- [21] H. L. Zhuang, A. K. Singh, and R. G. Hennig *Phys. Rev. B.* **87**, 165415 (2013).
- [22] H. Zheng, Xian-Bin Li, Nian-Ke Chen, Sheng-Yi Xie, W. Q. Tian, Y. Chen, H. Xia, S. B. Zhang, and Hong-Bo Sun, *Phys. Rev. B.* **92**, 115307 (2015).
- [23] D. Di Sante, A. Stroppa, P. Barone, Myung-Hwan Whangbo, and S. Picozzi, *Phys. Rev. B.* **91**, 161401 (2015).
- [24] Z. Y. Zhu and Y. C. Cheng and U. Schwingenschlgl, *Phys. Rev. B.* **84**, 153402 (2011).
- [25] Y. Liu, Y. Xu, J.P. Li, B. Zhang, D. Wu and Y.H. Sun, *Mater. Res. Bull.* **41**, 99 (2006).
- [26] G. Kresse and D. Joubert, *Phys. Rev. B* **59**, 1758 (1999).
- [27] P. E Blöchl, *Phys. Rev.* **50**, 17953 (1994).
- [28] G. Kresse and J. Furthmüller, *Phys. Rev. B* **54**, 11169 (1996).
- [29] J. P. Perdew, and A. Zunger, *Phys. Rev. B* **23**, 5048 (1981).
- [30] Su-Huai Wei and S. B. Zhang *Phys. Rev. B* **62**, 6944 (2000).

- [31] Su-Huai Wei and Alex Zunger Phys. Rev. B **60**, 5404 (1999).
- [32] J. Heyd, G.E. Scuseria, and M. Ernzerhof, J. Chem. Phys. **118** 8207 (2003); J. Chem. Phys. **124** 219906 (2006).
- [33] Atsushi Togo, Fumiyasu Oba, and Isao Tanaka, Phys. Rev. B **78**, 134106 (2008).
- [34] R. W. Nunes and Xavier Gonze, Phys. Rev. B **63**, 155107 (2001).
- [35] S. Debnath, Structural, Magnetic, Optical and Electronic Properties of Transition Metal Compounds and Semiconductors. Thesis submitted to Calcutta University (2015)
- [36] W. A. Harrison, E. A. Kraut, J. R. Waldrop and R. W. Grant, Phys. Rev. B **18**, 8 (1978).
- [37] C. Noguera and J. Goniakowski, Chem. Rev. **113**, 6 (2012).
- [38] P. Kumari, S. Debnath, and P. Mahadevan Phys. Rev. B(R) **97** 041404(R) (2018).
- [39] P. Dziawa, B. J. Kowalski, K. Dybko, R. Buczko, A. Szczerbakow, M. Szot, E. Lusakowska, T. Balasubramanian, B. M. Wojek, M. H. Berntsen, O. Tjernberg and T. Story Nat. Mat. **11**, 1023 (2012).
- [40] L. Kou, Y. Ma, Z. Sun, T. Heine and C. Chen, J. Phys. Chem. Lett. **8**, 1905 (2017).
- [41] H. Zhang, Chao-Xing Liu, Xiao-Liang Qi, X. Dai, Z. Fang and Shou-Cheng Zhang Nat. Phy. **5**, 483 (2009).
- [42] X. Qian, J. Liu, L. Fu, and J. Li, Science **346**, 1344 (2014).
- [43] T. H. Hsieh, H. Lin, J. Liu, W. Duan, A. Bansil and L. Fu Nat. Comm. **3**, 982 (2012).
- [44] T. Olsen, E. Andersen, T. Okugawa, D. Torelli, T. Deilmann, and K. S. Thygesen Phys. Rev. B **3**, 024005 (2019).
- [45] Y. Sun, Qing-Ze Wang, 2 Shu-Chun Wu, C. Felser, Chao-Xing Liu, and B. Yan, Phys. Rev. B **93**, 024005 (2019).
- [46] Q. Zhang, Y. Cheng and U. Schwingenschlögl Sci. Rep. **5**, 8379 (2015).
- [47] M. Wada, S. Murakami, F. Freimuth and G. Bihlmayer Phys. Rev. B **83**, 121310(R) (2011).

- [48] C. L. Kane and E. J. Mele Phys. Rev. Lett. **95**, 226801 (2005)
- [49] C. L. Kane and E. J. Mele Phys. Rev. Lett. **95**, 146802 (2005)
- [50] M. König, S. Wiedmann, C. Brüne, A. Roth, H. Buhmann, L. W. Molenkamp, Xiao-Liang Qi, and Shou-Cheng Zhang Science **318**, 766 (2007).
- [51] L. Kou, Y. Ma, B. Yan, X. Tan, C. Chen, and Sean C. Smith ACS Appl. Mater. Interfaces **7**, 19226 (2015)
- [52] F. Matusalem, D. S. Koda¹, F. Bechstedt, M. Marques and L. K. Teles Sci. Rep. **7**, 15700 (2017)
- [53] Run-wu Zhang, Wei-xiao Ji, Chang-wen Zhang, Ping Li and Pei-ji Wang Phys.Chem.Chem.Phys **18**, 28134 (2016)
- [54] M. Zhoua, W. Minga, Z. Liua, Z. Wanga, P Lia, and F. Liu PNAS **111**, 40 (2014).
- [55] F. Dominguez, B. Scharf, G. Li, J. Schäfer, R. Claessen, W. Hanke, R. Thomale, and E. M. Hankiewicz Phys. Rev. B. **98**, 161407(R) (2018)
- [56] E. Aktürk, O. Ü. Aktürk, and S. Ciraci Phys. Rev. B. **94**, 014115 (2016)
- [57] N. Nouri, M. Bieniek, M. Brzezinska, M. Modarresi, S. Zia Borujeni, Gh. Rashedi, A. Wojs and P. Potasz Phys. Lett. A **382**, 2952 (2018)
- [58] J. Harl, L. Schimka, and G. Kresse, Phys. Rev. B **81**, 118126 (2010).
- [59] J. P. Perdew, K. Burke, and M. Ernzerhof, Phys. Rev. Lett. **77**, 3865 (1996)
- [60] J. P. Perdew, B. Kieron, and E. Matthias, Phys. Rev. Lett. **78**, 1396 (1997).
- [61] P. Cucka and C. S Barrett, Acta Crystallographica **15** 865 (1962).
- [62] J. Spreadborough and J. W. Christian Journal of Scientific Instruments **36** 116 (1959).
- [63] Y. Shao, Zhong-Liu Liu, C. Cheng, X. Wu, H. Liu, C. Liu, Jia-Ou Wang, Shi-Yu Zhu, Yu-Qi Wang, Dong-Xia Shi, K. Ibrahim, Jia-Tao Sun, Ye-Liang Wang and Hong-Jun Gao Nano Lett. **18** 2133 (2018).
- [64] B. Feng, Z. Ding, S. Meng, Y. Yao, X. He, P. Cheng, L. Chen and K. Wu Nano Lett. **12** 3507 (2012).
- [65] H. Schulz, K. H Thiemann, Solid State Communications **32** 783 (1979).

- [66] P. Mahadevan and A. Zunger, *Phys. Rev. Lett.*, **88** 4 (2002).
- [67] F. Reis, G. Li, L. Dudy, M. Bauernfeind, S. Glass, W. Hanke, R. Thomale, J. Schäfer, R. Claessen, *Science* **357** 287 (2014).

Chapter 5

The Role Of Spin-Orbit Coupling On Magnetism In Sr_2IrO_4

5.1 Introduction

Sr_2IrO_4 is a $5d$ oxide and belongs to a series of material called the Ruddlesden-Popper series, which has a general formula $\text{Sr}_{n+1}\text{Ir}_n\text{O}_{3n+1}$ [1,2]. It is a series of layered perovskites which consists of n IrO_2 layers with double layers of SrO in between, stacked along c axis. Here n represents the number of layers that are immediately adjacent. For $n = 1$, there are single layers of IrO_2 that are separated by SrO layers. For $n = 2$, there are two layers of IrO_2 forming a bilayer structure that are separated by SrO layers. When $n = \infty$ the system is purely three dimensional. The electronic configuration of the ions in these systems are $\text{Sr}^{2+}(4p^6)$, $\text{Ir}^{4+}(5d^5)$ and $\text{O}^{2-}(2p^6)$. Figure 5.1 shows the structure of $\text{Sr}_{n+1}\text{Ir}_n\text{O}_{3n+1}$ for $n = 1$, $n = 2$, $n = 3$ and $n = \infty$ [3].

Members of this series exhibit varied properties, like Sr_2IrO_4 is an antiferromagnetic insulator [4–7], whereas SrIrO_3 is a non magnetic metal [8–11]. The properties of these compounds can be understood by looking at their electronic structure. The spatial extent of $5d$ orbitals is large. As a result, they have a large bandwidth (W) and a small on-site Coulomb interaction (U). The relative strength of W and U in these materials determine their electronic structure. The bandwidth W increases as we go from $n = 1$ to $n = 2$ to $n = \infty$ in the series. As a result, the properties changes gradually as from being an insulator for $n = 1$ to barely insulating for $n = 2$ to metallic for $n = \infty$ [12]. This has been shown schematically in Figure 5.2.

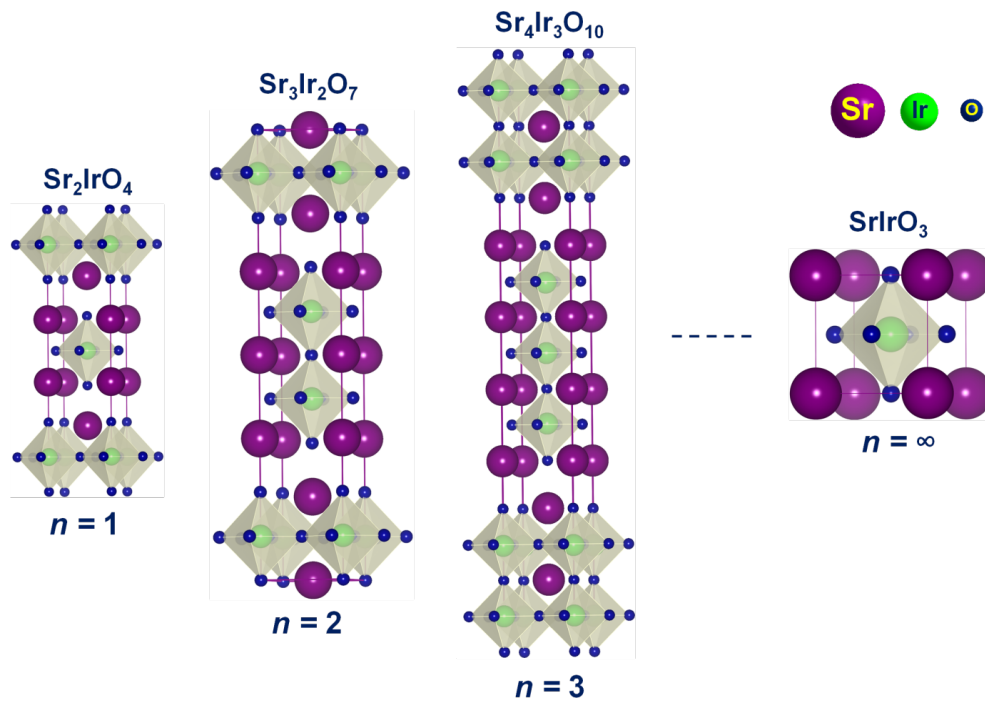


Figure 5.1: Structure of $\text{Sr}_{n+1}\text{Ir}_n\text{O}_{3n+1}$ for $n = 1$, $n = 2$, $n = 2$ and $n = \infty$. Reproduced from [3]

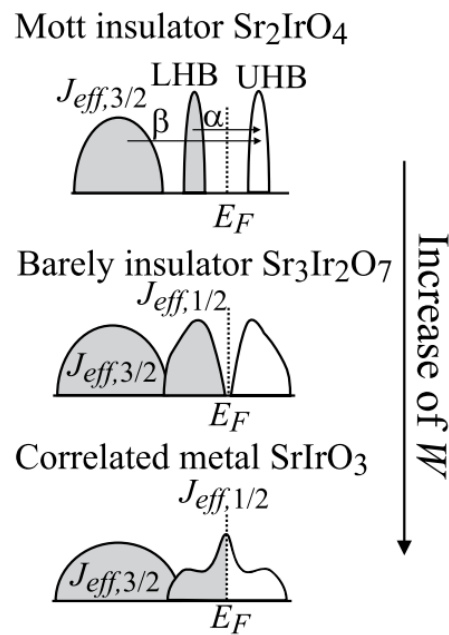


Figure 5.2: Schematic of the electronic structure of $\text{Sr}_{n+1}\text{Ir}_n\text{O}_{3n+1}$ for $n = 1$, $n = 2$ and $n = \infty$. Reproduced from [12]

In this work we studied one of the members of this series, Sr_2IrO_4 which is an antiferromagnetic insulator. Spin-orbit coupling plays an important role in making it insulating as well as magnetic [13–17]. We briefly discuss both these aspects here focusing on the role played by spin-orbit interactions.

Iridium atoms in Sr_2IrO_4 is in an octahedral environment with the oxygen atoms. As a result, crystal field splitting lifts the degeneracy of the d orbitals. The spin-orbit coupling then splits the t_{2g} orbitals of the iridium atom into four fold degenerate, fully filled $J_{eff}=3/2$ and two fold degenerate half filled $J_{eff}=1/2$ states. Since $J_{eff}=1/2$ bands are half filled, U opens up a gap, making it an insulator.

The widely accepted picture of magnetism in solids focuses on the existence of localized electrons and the ordering of their local moments leading to different types of magnetic ordering. As a result, $3d$ transition metal oxides like SrMnO_3 ($T_N = 233\text{K}$) [18] and $\text{Sr}_2\text{FeMoO}_6$ ($T_N = 410\text{-}450\text{K}$) [19] which have highly correlated electrons are associated with high magnetic ordering temperatures. $4d$ and $5d$ oxides which do not have highly correlated electrons are not expected to show magnetic ordering. But some of the $4d$ and $5d$ oxides (SrTcO_3 ; $T_N = 1024\text{ K}$ [20], CaTcO_3 ; $T_N = 800\text{ K}$ [21], Ba_2IrO_4 ; $T_N = 240\text{ K}$ [23], NaOsO_3 ; $T_N = 410\text{ K}$ [22]) show high magnetic ordering temperatures. The problem was investigated for the case of SrTcO_3 and CaTcO_3 . The high ordering temperature in these materials was attributed to the d^3 configuration at the transition metal site, which leads to the half filling of the t_{2g} states and allows electrons to be localized in an anti-ferromagnetic configuration only [24]. In this project we examine the role played by spin-orbit coupling in stabilizing high magnetic ordering temperature in Sr_2IrO_4 using a multiband Hubbard Hamiltonian with spin-orbit coupling term incorporated in it. We find that for a very narrow regime of U value, the antiferromagnetic state is stabilized.

5.2 Methodology

The bandstructure was calculated within a projector augmented-wave method implementation of density function theory (DFT) within the Vienna Ab-initio Simulation Package (VASP) [25,26]. The experimental crystal structure of Sr_2IrO_4 was taken with the lattice constant of 5.498 \AA [27]. The lattice parameters were kept fixed at the experimental values while the internal positions were optimized. The electronic structure was solved self consistently using a k-point mesh of $7\times 7\times 3$. Perdew Burke-Ernzerhof potentials were used for the exchange correlation functional [28,29]. Interaction parameters were obtained by fitting the non-magnetic ab-initio bandstructure on to a tight binding model. For the tight binding model, the basis used were Ir d , O s and O p . Hopping is considered between

Ir d , O s and O p . These hopping interactions (t_{ij} 's) were parametrized in terms of the Slater-Koster parameters $pd\sigma$, $pd\pi$, $sd\sigma$, $pp\sigma$ and $pp\pi$. This formed the one electron part of the Hamiltonian given below.

$$\begin{aligned}
H = & \sum_{i,l,\sigma} \epsilon_p p_{il\sigma}^\dagger p_{il\sigma} + \sum_{i,l,\sigma} \epsilon_d d_{il\sigma}^\dagger d_{il\sigma} - \sum_{i,j,l_1,l_2,\sigma} \left(t_{i,j,pp}^{l_1,l_2} p_{i,l_1,\sigma}^\dagger p_{j,l_2,\sigma} + \text{H.c.} \right) \\
& - \sum_{i,j,l_1,l_2,\sigma} \left(t_{i,j,pd}^{l_1,l_2} d_{i,l_1,\sigma}^\dagger p_{j,l_2,\sigma} + \text{H.c.} \right) \\
& + \sum_{\alpha,\beta,\gamma,\delta,\sigma_1,\sigma_2,\sigma_3,\sigma_4} U_{dd}^{\alpha\beta\gamma\delta} d_{\alpha\sigma_1}^\dagger d_{\beta\sigma_2}^\dagger d_{\gamma\sigma_3} d_{\delta\sigma_4}
\end{aligned} \quad (5.1)$$

Here $p_{il\sigma}^\dagger$ and $p_{il\sigma}$ creates and annihilates an electron with spin σ in the l^{th} p orbital on O in the i^{th} unit cell respectively. $d_{il\sigma}^\dagger$ and $d_{il\sigma}$ creates and annihilates an electron with spin σ in the l^{th} d orbital on Ir in the i^{th} unit cell respectively. $U_{dd}^{\alpha\beta\gamma\delta}$ is the Coulomb interactions between electrons on Ir site. A mean-field decoupling scheme has been used for the four fermion operator terms ($d_{i\uparrow}^\dagger d_{i\uparrow} d_{i\downarrow}^\dagger d_{i\downarrow}$) and is given by

$$\begin{aligned}
d_{i\uparrow}^\dagger d_{i\uparrow} d_{i\downarrow}^\dagger d_{i\downarrow} = & \langle d_{i\uparrow}^\dagger d_{i\uparrow} \rangle d_{i\downarrow}^\dagger d_{i\downarrow} + d_{i\uparrow}^\dagger d_{i\uparrow} \langle d_{i\downarrow}^\dagger d_{i\downarrow} \rangle - \langle d_{i\uparrow}^\dagger d_{i\downarrow} \rangle d_{i\downarrow}^\dagger d_{i\uparrow} - d_{i\uparrow}^\dagger d_{i\downarrow} \langle d_{i\downarrow}^\dagger d_{i\uparrow} \rangle \\
& - \langle d_{i\uparrow}^\dagger d_{i\uparrow} \rangle \langle d_{i\downarrow}^\dagger d_{i\downarrow} \rangle + \langle d_{i\uparrow}^\dagger d_{i\downarrow} \rangle \langle d_{i\downarrow}^\dagger d_{i\uparrow} \rangle
\end{aligned} \quad (5.2)$$

The Hamiltonian is then solved self-consistently for the order parameters [30]. The spin-orbit interaction was incorporated as

$$H_{SO} = \lambda \vec{L} \cdot \vec{S} = \lambda (L_x S_x + L_y S_y + L_z S_z) = \lambda \left(\frac{1}{2} L_+ S_- + \frac{1}{2} L_- S_+ + L_z S_z \right) \quad (5.3)$$

Here λ is the spin-orbit coupling constant, \vec{L} is the orbital angular momentum and \vec{S} is the spin angular momentum. $L_x(S_x)$, $L_y(S_y)$ and $L_z(S_z)$ are the x, y and z components of orbital angular momentum (spin angular momentum) respectively. Also, $L_+(S_+)$ and $L_-(S_-)$ are the raising and lowering operators for orbital angular momentum (spin angular momentum) respectively.

5.3 Result and Discussion

We begin by looking at the structure of Sr_2IrO_4 in detail. Sr_2IrO_4 has a tetragonal unit cell with the lattice vectors given as $a = b = 5.498\text{\AA}$ while $c = 25.798\text{\AA}$ (shown in Figure 5.6). It has layers of distorted Ir-O octahedra separated by layers of Sr atoms. Each Ir-O octahedra has tetragonal distortion leading to longer Ir-O bonds in the z-direction, than in the x-y plane. Sr_2IrO_4 is reported to be an antiferromagnetic insulator with a bandgap of $\sim 0.1\text{ eV}$ [14].

We calculated the non-magnetic bandstructure for Sr_2IrO_4 using first principle ab-initio calculation, then the tight binding parameters were determined by least square error minimization of the ab-initio bandstructure within the tight binding model. Bandstructure obtained by both these methods are shown in Figure 5.3 and the parameters obtained are listed in Table 5.1.

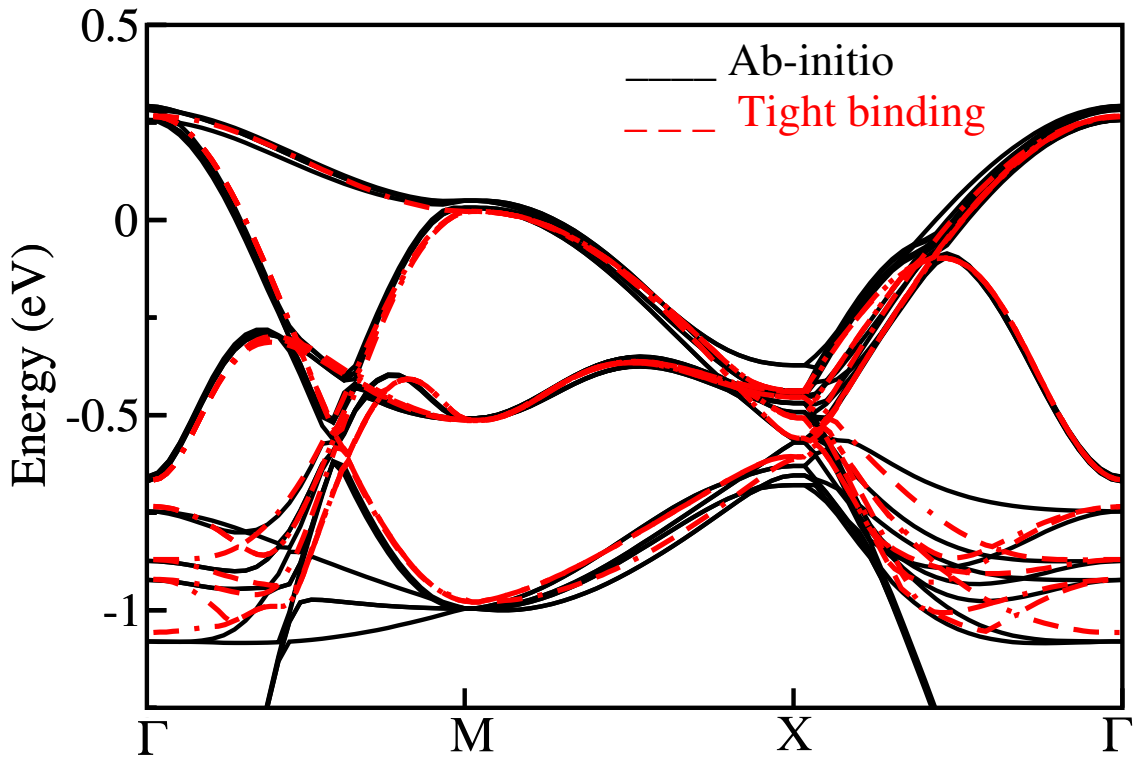


Figure 5.3: Non-magnetic bandstructure of Sr_2IrO_4 using ab-initio (solid black line) method and tight binding (dashed red line) along various symmetry directions. Γ , M and X are taken to be $(0.0, 0.0, 0.0)$, $(0.5, 0.5, 0.0)$ and $(0.5, 0.0, 0.0)$ respectively.

	E_s	E_{p_x, p_y}	E_{p_z}	$E_{d_{xy}}$	$E_{d_{yz}}$	$E_{d_{zx}}$	$E_{x^2-y^2}$	E_{z^2}
Ir	-	-	-	1.82	1.82	1.82	2.51	2.51
O_1	-16.36	0.38	1.22	-	-	-	-	-
O_2	-13.05	1.45	1.09	-	-	-	-	-
	$E(Ir, Ir)$	$E(Ir, O_1)$	$E(Ir, O_2)$	$E(O_1, O_1)$	$E(O_2, O_2)$	$E(O_1, O_2)$		
$dd\sigma$	-0.25	-	-	-	-	-	-	-
$dd\pi$	0.21	-	-	-	-	-	-	-
$dd\delta$	-0.23	-	-	-	-	-	-	-
$ds\sigma$	-	-3.00	-3.55	-	-	-	-	-
$dp\sigma$	-	2.44	2.53	-	-	-	-	-
$dp\pi$	-	-1.45	-1.45	-	-	-	-	-
$pp\sigma$	-	-	-	0.59	0.39	0.05	-	-
$dd\pi$	-	-	-	-0.40	-0.28	-0.25	-	-

Table 5.1: Parameters obtained from least-squared-error fitting of the ab-initio band structure onto a tight binding model for Sr_2IrO_4 .

We then plotted the density of states of Ir d states using our tight binding model and it is shown in Figure 5.4. At this level of we do not have U and spin-orbit interactions included. Here we can see that all the three t_{2g} orbitals (d_{xy} , d_{yz} and d_{xz}) are occupied whereas the two e_g orbitals ($d_{x^2-y^2}$ and d_{z^2}) are unoccupied. This demonstrates the octahedral splitting of the Ir d states an the octahedral environment.

After this we incorporated spin-orbit coupling term in the hamiltonian. This splits the occupied, t_{2g} orbitals into $J_{eff}=3/2$ which is fully filled and $J_{eff}=1/2$ which is half filled. Now, introduction of U splits the half filled $J_{eff}=1/2$ bands into fully occupied upper hubbard band (UHB) and completely unoccupied lower hubbard band (LHB) opening up a gap and making Sr_2IrO_4 an insulator as shown in Figure 5.5

The splitting of the partly occupied t_{2g} orbitals by spin-orbit coupling into $J_{eff}=3/2$ and $J_{eff}=1/2$ and subsequently formation of UHB and LHB due to U also plays a very important role in understanding the magnetism in this material. In order to understand this we studied the electronic structure at different values of U considering various magnetic configurations which are shown in Figure 5.6b and 5.6c. In the case shown in Figure 5.6b, the magnetic moments on Ir atoms are antiferromagnetically aligned in one plane whereas the the case shown in Figure 5.6c the magnetic moments are ferromagnetically aligned in one plane.

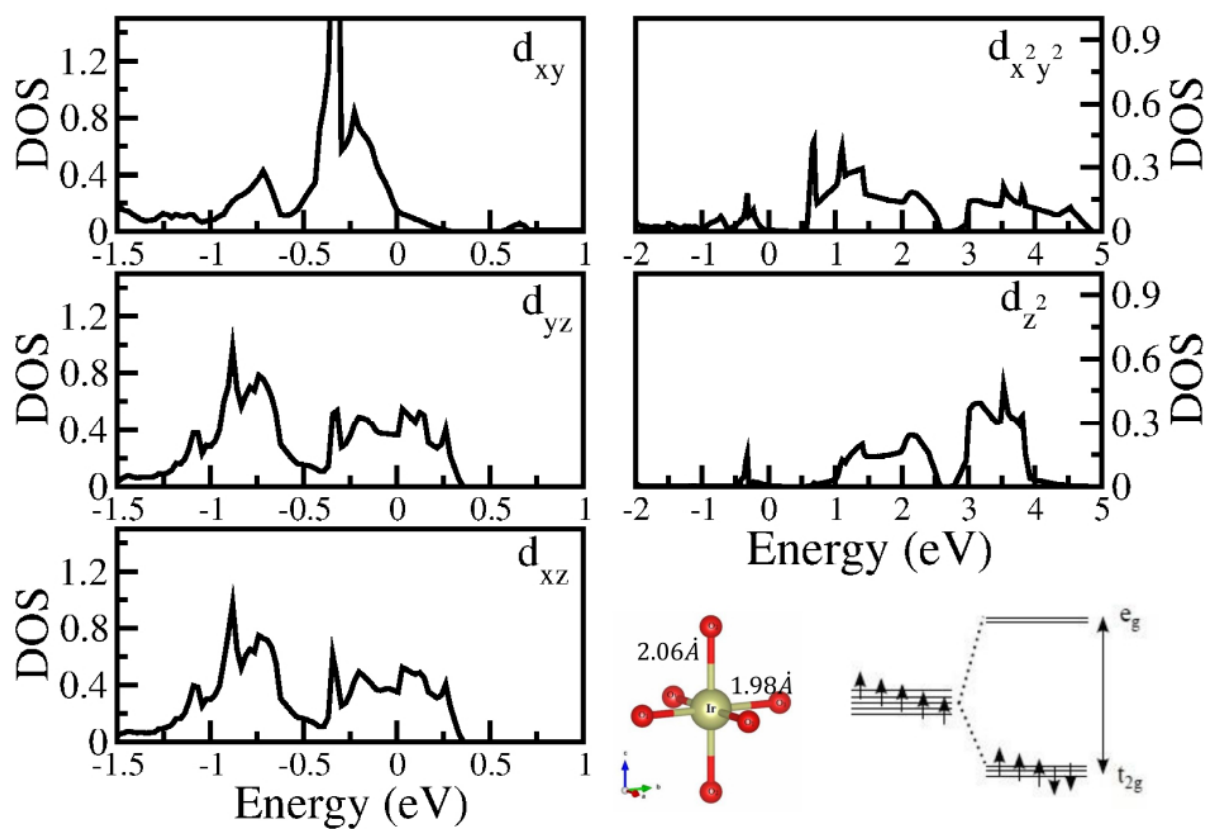
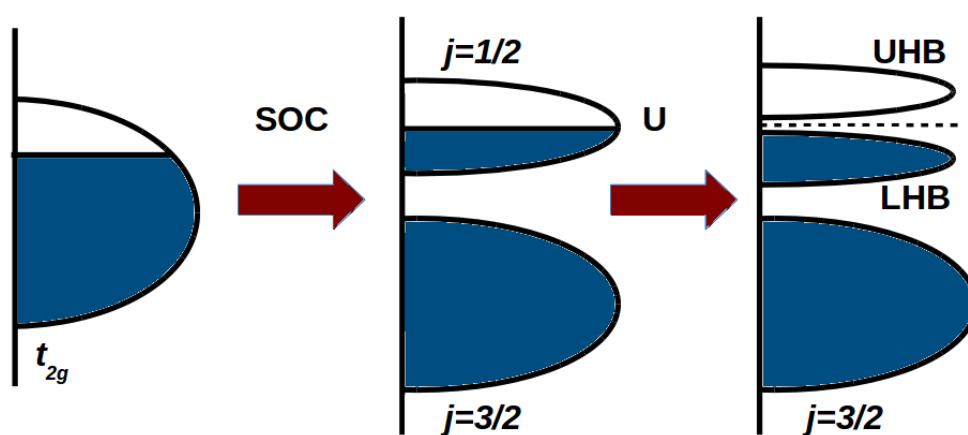


Figure 5.4: Orbital projected density of states for Ir atom

Figure 5.5: Schematic of the electronic structure of Sr_2IrO_4

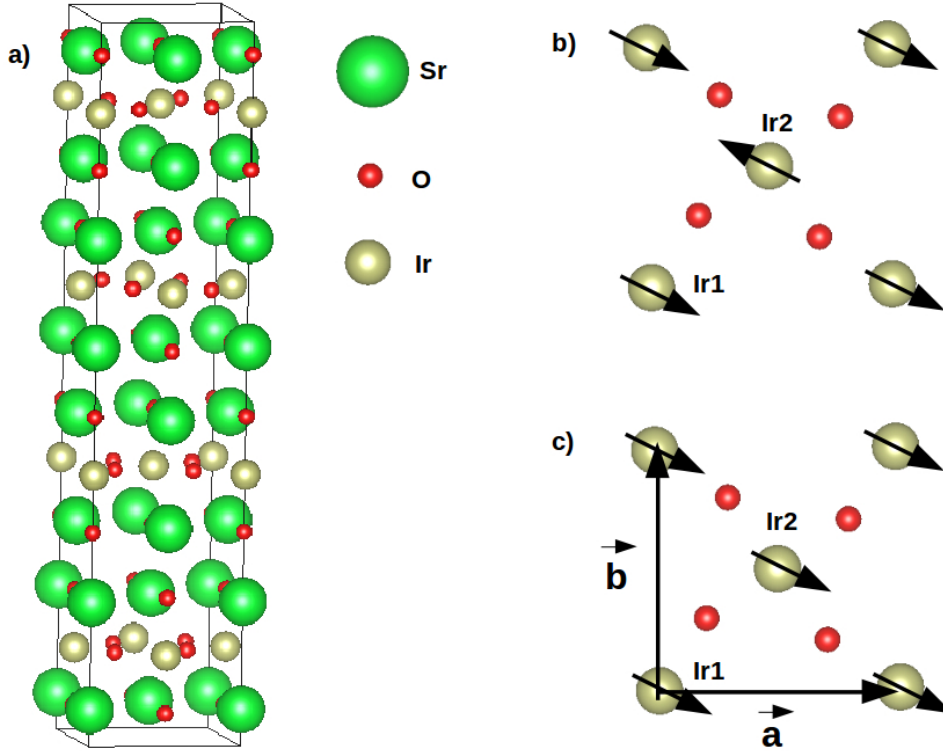


Figure 5.6: Various magnetic configurations considered for Sr_2IrO_4

We present the results at two different U values here, $U=1.0$ eV and $U=1.5$ eV. At both these U values, we have taken the spin-orbit coupling to be 0.4 eV [14]. At $U=1.0$ eV we find that the antiferromagnetic configuration is stable by 114 meV as compared to the other configuration. The magnetic moment in this case is $0.08 \mu_B$ per iridium atom in the xy plane. The bandstructure for this case, calculated along different symmetry directions are shown in Figure 5.7 with Fermi energy at 0. We can see that the valence band maximum is at the Γ point whereas the conduction band minimum is near the X point, making it an indirect bandgap material. The bandgap at this value of U and spin-orbit coupling is found to be 0.12 eV. As we start increasing U and go to $U=1.5$ eV, we find that the two magnetic configuration considered by us are energetically degenerate. Antiferromagnetic state is no longer energetically favored state. In this case, the moment on the iridium atom is $0.12 \mu_B$ in the xy plane. Figure 5.8 shows the bandstructure of Sr_2IrO_4 calculated along various symmetry directions at $U=1.5$ eV with Fermi energy at 0. The position of the valence band maximum and the conduction band minimum in this case remains the same as $U=1.0$ eV. The bandgap however increases to 0.5 eV.

In order to understand this magnetic behaviour of Sr_2IrO_4 at different U regime, we take a closer look at the bandstructure in the two cases. We can see that at $U=1.0$ eV, the

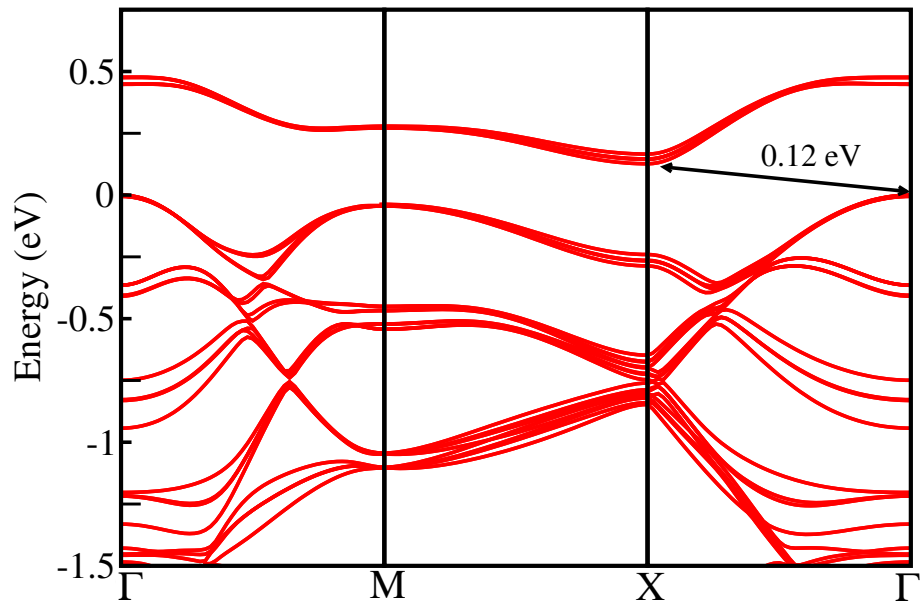


Figure 5.7: Bandstructure of Sr₂IrO₄ using multiband hubbard hamiltonian with spin orbit coupling included for $U=1.0$ eV, $SO=0.4$ eV along various symmtery directions.

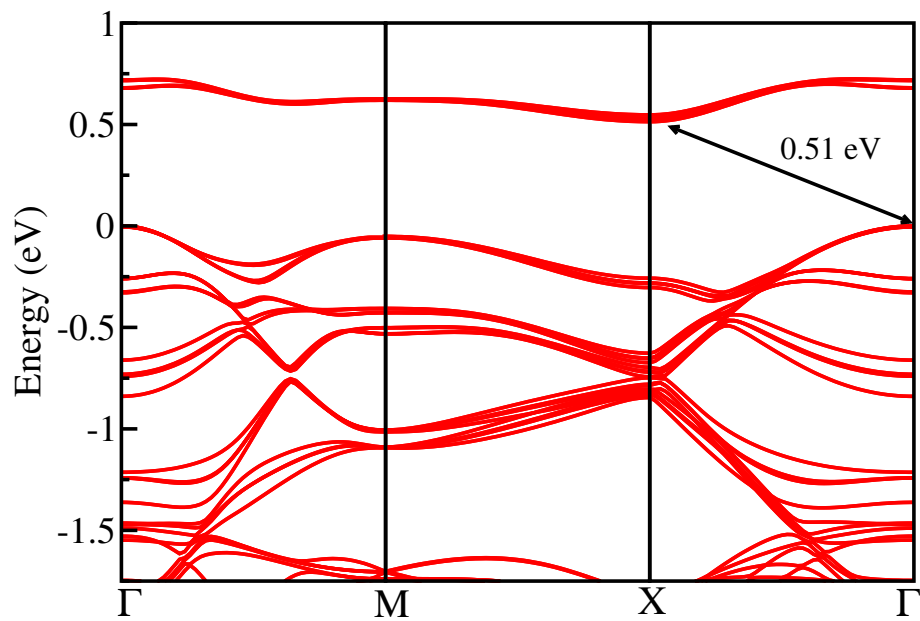


Figure 5.8: Bandstructure of Sr₂IrO₄ using multiband hubbard hamiltonian with spin orbit coupling included for $U=1.5$ eV, $SO=0.4$ eV along various symmtery directions.

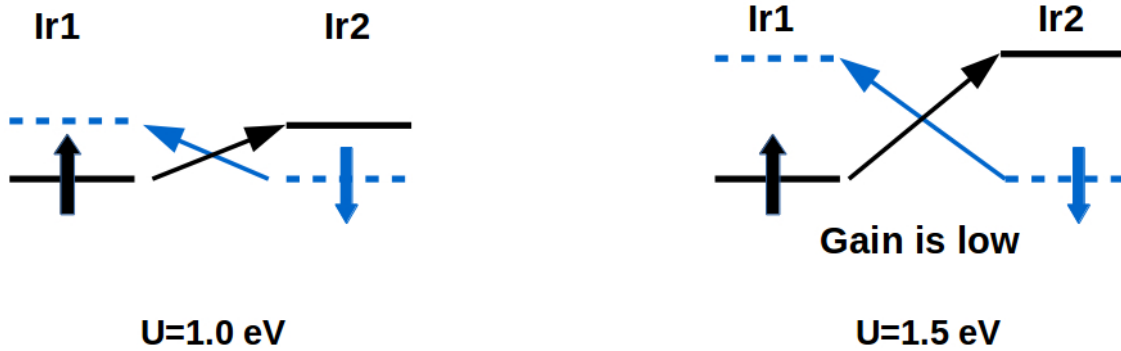


Figure 5.9: Schematic explaining magnetic stability for $U=1.0$ eV compared to $U=2.0$ eV

dispersional width of the conduction band is ~ 0.4 eV whereas when we go to $U=1.5$ eV it decreases to ~ 0.25 eV. This can be understood as follows. As explained earlier, $J_{eff}=1/2$ band is half filled and with the introduction of U it splits into UHB and LHB. This can be represented as shown in the Figure 5.9. We have up spin at Ir1 site and down spin at Ir2 site. The downspin at Ir1 is unoccupied whereas the upspin at the Ir2 site is unoccupied. Now when $U=1.0$ eV the separation between the occupied and the unoccupied band is small and hence each of the spin can hop to the next site as is shown in the Figure 5.9. As a result antiferromagnetic configuration in this case becomes stable as it gains energy by hopping. This is reflected from the dispersional width of the conduction band in this case (Figure 5.7). Now as we start increasing U and goto the case of $U=1.5$ eV we see that the separation between the occupied and the unoccupied states increases so much that hopping between neighboring site is reduced considerably and the gain in energy by this process is less, hence all the magnetic configurations are degenerate in energy. This is also reflected in the decreased dispersional width of the conduction band in this case, as can be seen in Figure 5.8

5.4 Conclusion

5d transition metal oxide, Sr_2IrO_4 has interesting electronic structure. In spite of electron-electron correlation being low in this material it is an antiferromagnetic insulator. In this work within a multiband hubbard hamiltonian framework we try to understand the electronic structure as well as the role played by various interactions specially spin-orbit coupling in stabilizing long range magnetic ordering. We find that only for a very narrow region of U around 1.0 eV we have the antiferromagnetic state stable due to gaining in

energy resulting from hopping between the occupied and the unoccupied states in that regime of U .

Bibliography

- [1] H. Zhang, K. Haule and D. Vanderbilt, *Phys. Rev. Lett.* **111**, 246402 (2013).
- [2] X. Liu, Y. Cao, B. Pal, S. Middey, M. Kareev, Y. Choi, P. Shafer, D. Haskel, E. Arenholz and J. Chakhalian, *Phys. Rev. Mat.* **1** 075004 (2017).
- [3] A. Biswas, K.-S. Kim and Y. H. Jeong, *Metal-Insulator Transitions and Non-Fermi Liquid Behaviors in 5d Perovskite Iridates*, Ch.7 p 230, (2016).
- [4] H. Watanabe, T. Shirakawa and S. Yunoki, *Phys. Rev. Lett.* **105**, 216410 (2010).
- [5] B. J. Kim, H. Ohsumi, T. Komesu, S. Sakai, T. Morita, H. Takagi and T. Arima, *Science*. **323**, 1329-1332 (2009).
- [6] S. Boseggia, R. Springell, H. C. Walker, H. M. Ronnow, Ch. Rüegg, H. Okabe, M. Isobe, R. S. Perry, S. P. Collins and D. F. McMorrow, *Phys. Rev. Lett.* **110**, 117207 (2013).
- [7] P. Liu, S. Khmelevskiy, B. Kim, M. Marsman, D. Li, X.-Q. Chen, D. D. Sarma, G. Kresse and C. Franchini, *Phys. Rev. B* **92**, 054428 (2015).
- [8] G. Cao, V. Durairaj, S. Chikara, L. E. DeLong, S. Parkin and P. Schlottmann, *Phys. Rev. B.* **76**, 100402(R) (2007).
- [9] I. Qasim, B. J. Kennedy and M. Avdeev, *J. Mater. Chem. A* **1**, 3127 (2013).
- [10] M. A. Zeb and H.-Y. Kee, *Phys. Rev. B.* **86**, 085149 (2012).
- [11] A. Biswas and Y. H. Jeong, *J. Phys. D: Appl. Phys.* **48**, 135303 (2015).
- [12] S. J. Moon, H. Jin, K. W. Kim, W. S. Choi, Y. S. Lee, J. Yu, G. Cao, A. Sumi, H. Funakubo, C. Bernhard, and T. W. Noh, *Phys. Rev. Lett.* **101**, 226402 (2008).
- [13] G. Jackeli and G. Khaliullin, *Phys. Rev. Lett.* **102**, 017205 (2009).

- [14] B. J. Kim, Hosub Jin, S. J. Moon, J.-Y. Kim, B.-G. Park, C. S. Leem, Jaejun Yu, T. W. Noh, C. Kim, S.-J. Oh, J.-H. Park, V. Durairaj, G. Cao and E. Rotenberg, *Phys. Rev. Lett.* **101**, 076402 (2008).
- [15] J. P. Clancy, N. Chen, C. Y. Kim, W. F. Chen, K. W. Plumb, B. C. Jeon, T. W. Noh, and Y.-J. Kim, *Phys. Rev. Lett.* **86**, 195131 (2012).
- [16] J. S. Lee, Y. Krockenberger, K. S. Takahashi, M. Kawasaki and Y. Tokura, *Phys. Rev. B.* **85**, 035101 (2012).
- [17] D. Haskel, G. Fabbris, M. Zhernenkov, P. P. Kong, C. Q. Jin, G. Cao and M. van Veenendaal, *Phys. Rev. Lett.* **109**, 027204 (2012).
- [18] O. Chmaissem, B. Dabrowski, S. Kolesnik, J. Mais, D. E. Brown, R. Kruk, P. Prior, B. Pyles and J. D. Jorgensen, *Phys. Rev. B* **64**, 134412 (2001).
- [19] K.-I. Kobayashi, T. Kimura, H. Sawada, K. Terakura and Y. Tokura, *Nature.* **395**, 677-680 (1998).
- [20] E. E. Rodriguez, F. Poineau, A. Llobet, B. J. Kennedy, M. Avdeev, G. J. Thorogood, M. L. Carter, R. Seshadri, D. J. Singh and A. K. Cheetham, *Phys. Rev. Lett.* **106**, 067201 (2011).
- [21] M. Avdeev, G. J. Thorogood, M. L. Carter, B. J. Kennedy, J. Ting, D. J. Singh and K. S. Wallwork, *J. Am. Chem. Soc.* **133**, 1654(2011).
- [22] Y. G. Shi, Y. F. Guo, S. Yu, M. Arai, A. A. Belik, A. Sato, K. Yamaura, E. Takayama-Muromachi, H. F. Tian, H. X. Yang, J. Q. Li, T. Varga, J. F. Mitchell and S. Okamoto, *Phys. Rev. B* **80**, 161104 (2009).
- [23] S. Moser, L. Moreschini, A. Ebrahimi, B. D. Piazza, M. Isobe, H. Okabe, J. Akimitsu, V. V. Mazurenko, K. S. Kim, A. Bostwick, E. Rotenberg, J. Chang, H. M. Ronnow and M. Grioni, *New J. of Phys.* **16** 013008 (2014).
- [24] S. Middey, A. K. Nandy, S. K. Pandey, Priya Mahadevan and D. D. Sarma, *Phys. Rev. B* **86**, 104406 (2012).
- [25] G. Kresse and J. Hafner, *Phys. Rev. B* **47**, 558 (1993).
- [26] G. Kresse and J. Hafner, *Phys. Rev. B* **49**, 14251 (1994).
- [27] M. K. Crawford, M. A. Subramanian and R. L. Harlow, *Phys. Rev.* **49**, 13, (1994).
- [28] J. P. Perdew, K. Burke, and M. Ernzerhof, *Phys. Rev. Lett.* **77**, 3865 (1996).

- [29] J. P. Perdew, B. Kieron, and E. Matthias, *Phys. Rev. Lett.* **78**, 1396 (1997).
- [30] S. Nimkar, D. D. Sarma, H. R. Krishnamurthy and S. Ramasesha, *Phys. Rev. B*, **48**, 7355 (1993).

Appendix A

A.1 Monte Carlo Simulation For Heisenberg Model

Monte Carlo simulations are computational methods to model the probability of different outcomes for processes where the time dependence of the growth or the change does not follow a very rigid or rigorous rules and can not be predicted. It is often used in Physics, mathematics, economics, engineering, finance etc. to solve problems like flow through porous rocks, behavior of dilute magnets, diffusion limited aggregation. It is used to solve problems which have a probabilistic interpretation. In physics Monte Carlo has been in use for a long time. In 1949 Metropolis and Ulam presented a review of the use of Monte Carlo simulations [1]. They enumerated the advantages of the use of this method to solve problems. his method is based on repeated random sampling of phase space and computing the results using statistical analysis.

During the course of this thesis, we used Monte Carlo simulation to calculate magnetization in dilute magnetic semiconductors, which was inturn used to get the transition temperature within a classical Heisenberg Model. In the next section we first discuss the Heisenberg Model then the Metropolis algorithm, which has been used for producing samples.

A.2 Heisenberg Model

Heisenberg Model is a vector model which is used in statistical physics to model a magnetic system. This model is given as

$$H = - \sum_{i,j} J_{i,j} \vec{S}_i \cdot \vec{S}_j \tag{A.1}$$

here, $J_{i,j}$ is the exchange interaction between nearest neighbor sites. It can have a positive or a negative value representing ferromagnetic and antiferromagnetic configuration respectively. \vec{S}_i and \vec{S}_j are the spin on the i -th and the j -th sites respectively. In a Heisenberg model, spins can take all possible directions. One way to do this is to work in spherical coordinates, by varying θ and ϕ from 0 to π and 0 to 2π respectively using random numbers one can assign any direction to the spin.

A.3 Metropolis Hastings Algorithm

The Metropolis Hastings algorithm is an algorithm for producing samples from a distribution. It is very commonly used in Monte Carlo simulations. It was proposed by Nicholas Metropolis, A. W. Rosenbluth, M. N. Rosenbluth, A. H. Teller and E. Teller [3]. In this method one can generate configurations from a previous state using a transition probability. This transition probability depends on the energy difference between the initial and final states.

The scheme of Metropolis Hastings algorithm is as follows:

1. An initial state is chosen by randomly assigning spins to the sites randomly.
2. Total energy of the system is calculated using for that state.
3. A site i is chosen.
4. The spin at the site i is changed randomly.
5. Total energy is again calculated. If the change in energy (ΔE) is negative, the new configuration at i is accepted.
6. If ΔE is positive, a random number r is generated such that $0 < r < 1$. If $r < \exp(-\Delta E/k_B T)$, the new configuration is accepted.
7. Go to the next site and go to step 4.

The important point to note here is that the successive random number generated should be uncorrelated and it should be chosen uniformly between 0 and 1. This is done for all the sites till equilibrium is reached. Once equilibrium is reached, various properties of the system is calculated.

A.4 Results

In our work a Heisenberg model of the form given in Equation A.1 is considered. Exchange interaction strengths entering this model were extracted until fourth neighbor from our calculations and solved for a lattice with 6912 sites with 3.125 % magnetic doping. The distribution of the magnetic atoms were kept random in six cases. Starting from a random configuration of spins the system was brought to a thermal equilibrium within 2×10^7 Monte Carlo steps for every temperature cycle. Once the system goes into thermal equilibrium, magnetization of the lattice was calculated using

$$M = \sqrt{M_X^2 + M_Y^2 + M_Z^2} \quad \text{where} \quad M_{X/Y/Z} = \sum_{i=1}^N S_i^{X/Y/Z} \quad (\text{A.2})$$

Magnetization per site (m_i) is then calculated by normalizing this over the system size. The arithmetic average of m_i over many configuration is calculated and averaged over to get the ensemble average of magnetization given as

$$\langle m \rangle = \frac{1}{mcs} \sum_i^{mcs} m_i \quad (\text{A.3})$$

Important point here to note that magnetization is calculated only after the system has reached equilibrium. Some of the results obtained by the Monte Carlo code written by me can be found in references [4]

Bibliography

- [1] D.P. Landau and K. Binder, A Guide to Monte Carlo Simulations in Statistical Physics, Cambridge Univ. Press (2000)
- [2] N. Metropolis and S. Ulam, J. Amer. Stat. Assoc. **44**, 335 (1949).
- [3] N.C. Metropolis et al., J. Chem. Phys. **21**, 1087 (1953).
- [4] B. Mandal, H. K. Chandra, P. Kumari and P Mahadevan, **96**, 014430 (2017).